Refractive Hard X-Ray Nanofocusing at Storage Ring and X-Ray Free-Electron Laser Sources

Dissertation

zur Erlangung des Doktorgrades

an der Fakultät für Mathematik, Informatik
und Naturwissenschaften

Fachbereich Physik

der Universität Hamburg

vorgelegt von

Frank Seiboth

aus Dresden

Hamburg
2016

Gutachter: Prof. Dr. Christian G. Schroer
Prof. em. Dr. Bruno Lengeler

Datum der Disputation: 22.03.2016

Abstract

Nanofocused hard x-ray beams are an essential tool at modern synchrotron radiation facilities. Tightly focused probe beams are mandatory to reach highest resolution in various x-ray microscopy schemes mapping the local elemental composition, chemical state, or atomic structure. Achievable spatial resolution is typically limited by the probe size itself and the applied dose. Both parameters are strongly dependent on the focusing quality and efficiency of x-ray optics used. This thesis focuses on the improvement of refractive hard x-ray optics. A new lens design is introduced that facilitates the use of coating techniques to fabricate lenses. This enables one to exploit x-ray optically favorable materials like aluminum oxide that were inaccessible beforehand. Experimental results proof the working principle of this new lens design and demonstrate the feasibility of aluminum oxide as a suitable material for refractive x-ray optics.

In addition an aberration correction scheme based on a corrective phase plate, applicable to various x-ray optics, is presented. On the example of beryllium lenses spherical aberrations are characterized by means of ptychography. Based on this knowledge a corrective phase plate was designed and matched exactly to the specific optical element. It consists of fused silica and is machined by laser ablation. Experiments on different synchrotron radiation facilities are performed, demonstrating a reduction in the strength of spherical aberrations by an order of magnitude. The corrected optical element performs nearly at the diffraction limit, eliminating disadvantageous side lobes and increasing the peak intensity in the focal plane simultaneously. Benefits and possible new application fields for this aberration free, radiation hard, and efficient refractive hard x-ray optics are outlined.

Kurzfassung

Fokussierte harte Röntgenstrahlen im Nanometerbereich sind ein unentbehrliches Instrument an modernen Großforschungsanlagen mit Synchrotronstrahlung. Diese extrem stark fokussierten Nanosonden sind notwendig, um höchste räumliche Auflösung bei verschiedensten Techniken in der Röntgenmikroskopie zu erzielen. Dabei werden zum Beispiel die Elementzusammensetzung, chemische Zustände und atomare Strukturen lokal abgebildet. Die zu erreichende Auflösung ist durch die Fokusgröße an sich, als auch durch die verfügbare Dosis begrenzt. Beide Größen werden maßgeblich durch die verwendete Röntgenoptik beeinflusst. Die vorliegende Arbeit beschäftigt sich deshalb mit der Verbesserung der Fokussiereigenschaften refraktiver Röntgenoptiken. In diesem Rahmen wurde ein neuartiges Linsenkonzept entwickelt. Es erlaubt die Verwendung von Beschichtungstechnologien zur Linsenherstellung und ermöglicht damit den Einsatz von Materialen wie Aluminiumoxid, die zuvor unzugänglich waren, mit sehr guten optischen Eigenschaften. Die Funktionalität des neuen Linsendesigns und die Eignung von Aluminiumoxid als Linsenmaterial werden experimentell untersucht.

Ein weiterer Gesichtspunkt dieser Arbeit ist die Beseitigung von Aberrationen in bereits vorhandenen Optiken mit Hilfe einer Phasenplatte. Am Beispiel von Berylliumlinsen werden zunächst sphärische Aberrationen hoch präzise mit der Methode der Ptychographie vermessen. Diese Daten werden anschließend verwendet, um eine exakt angepasste Phasenplatte zu konstruieren. Die Herstellung erfolgt aus Quarzglas mit Hilfe eines Kurzpulslasers durch Materialabtrag. Bei Experimenten an verschiedenen Synchrotronstrahlungsquellen konnte der Einfluss von sphärischen Aberrationen auf das Wellenfeld um eine Größenordnung reduziert werden. Die korrigierte Optik erzielt damit fast die nominelle Beugungsbegrenzung, was sich vor allem durch deutlich reduzierte Nebenmaxima und damit in einer erhöhten Maximalintensität im zentralen Fleck des Beugungsscheibchen äußert. Sich daraus ergebende Vorteile und neue Anwendungsmöglichkeiten dieser aberrationsfreien, strahlenharten und zugleich transparenten Röntgenoptik werden diskutiert.

Contents

1 Introduction

Since the discovery of x rays in 1895 [Rön95] and the finding that both x rays and visible light are part of the electromagnetic spectrum, enabling one to use optics theory for visible light also in the x ray regime, the desire was born to develop suitable x-ray optics for x-ray microscopy. This kind of microscope is of very high interest due to the extraordinary properties of x rays. One of them is the large penetration depth in matter. Unlike visible light or electron beams x rays can penetrate matter and reveal interior properties of the specimen without special sample preparation that might destroy features of interest. The high energy of x rays and their wavelength comparable to atomic length scales allows for, amongst others, the determination of elemental composition, chemical state or atomic structure. The foundation to reveal these information was laid in the beginning of the 20th century when x-ray analytical techniques like crystallography, fluorescence and absorption spectroscopy as well as small angle x-ray scattering were developed. In this time most of the experiments were carried out using unfocused x-ray beams that were eventually collimated by slits. While some degree of spatial filtering using slits is possible, the method is limited by feasible slit sizes and reduces the usable x-ray flux dramatically. To limit the spatial extent of the x-ray probe beam even more while maintaining a high photon flux for appropriate signal levels x-ray optics are required.

However, today's available x-ray optics are hardly comparable to visible light optics. Imagine visible light optics without transparent and aberration-free lenses! Images in tele- or microscopes would appear only faint and distorted. Though, many tools in everyday life such as magnification glasses, binoculars, and spectacles rely on appropriate optical components. Their performance was greatly enhanced since the art of lens grinding developed in the 14th century and the first microscope was built in the late 16th century. From this point on, a rapid evolution in optics started. Theory evolved from geometric optics in the Greco-Roman world over diffractive optics in early modern Europe of the 17th century to wave and quantum optics in the 20th century. Together with this growth in understanding the nature of light both materials and manufacturing techniques improved continuously.

Despite the tremendous theoretical background and practical experience from visible light optics the manufacturing of x-ray optics only began not before the middle of the 20th century with reflective optical elements [KB48] and still today is trying ro reach the quality of visible light optics. Surprisingly refractive lenses, which are the most widely used optics in the visible light regime, were not developed before the end of the 20th century. Main reason were the small refraction effects of x rays with matter as observed early on by W. C. Röntgen [Rön95], which prevented further efforts in refractive x-ray focusing at first. While main limitations are of fundamental nature, current optics are still limited by manufacturing constraints. These high demands in x-ray optics fabrication are a consequence of x-ray matter interaction. Furthermore, the available x-ray sources were weak and of lower coherence than comparable visible light ones. It was thus not until the advent of third generation synchrotron sources in the 1990th that x-ray microscopy has become a viable tool for sample investigation on mesoscopic length scales.

Today's x-ray optics allow to generate sub-$100\,\mathrm{nm}$ beams and recent developments demonstrated focusing below $10\,\mathrm{nm}$ in one dimension [Mor+15] at storage ring sources. For the extremely bright x-ray free-electron laser sources optics are needed that withstand the intense x-ray pulses without getting damaged. Diamond Fresnel zone plates [Dav+11], beryllium refractive lenses [Sch+13] and reflective mirrors [Yam+15] were successfully used for nanofocusing. Besides reducing the focal spot size the improvement of efficiency or transparency of x-ray optics are further important aspects. Another crucial step is the minimization of aberrations. While all these optics can create a relatively small focal spot due to their high numerical aperture, the spot is often surrounded by strong side lobes. Aberrations reduce the intensity in the focal spot as well as the spatial resolution and can distort the image.

The thesis builds on the pioneering work by Snigirev and Lengeler et al. [Sni+96], who fabricated the first refractive lenses for hard x rays, and on subsequent work of Schroer et al. [Sch+03], who used fabrication techniques from the semiconductor industry to build one-dimensional nanofocusing lenses. The latest improvements in x-ray optics were not possible without an appropriate characterization method. While in the visible light regime several techniques for optics characterization existed [Mal07], the characterization of x-ray foci was difficult and could only be carried out using classical knife-edge techniques. It was not until 2008 that a complete characterization of the focused wave field of x-ray optics was possible [Thi+08]. As the quality and coherence properties of x-ray sources improved, microscopy techniques based on coherent imaging further developed [Mia+99; Mar+03; Rod+07]. From these, a new method, named ptychography, allowed to determine both the x-ray transmission function of an object as well as the incident wave field penetrating the investigated sample. Together with the adoption of well-known tests from visible light optics like the Ronchi test [Nil+12] essential tools were at hand to characterize x-ray optics with beforehand unknown accuracy. The detailed knowledge of the focused x-ray wave field, as well as eventual errors, then created new possibilities to further improve x-ray optics. These new tools together with recent developments in fabrication techniques are exploited in this work. Main objectives were the development of more efficient refractive optics for nanofocusing at storage ring sources and the improvement of focusing quality by aberration correction for beryllium lenses used at both storage ring and XFEL sources.

The remainder of this work is structured as follows. Chapter 2 gives a short introduction to wave optics and discusses the interaction of x rays with matter. Modern x-ray sources and their most important properties for the scope of this thesis are presented in Chapter 3. Based on these foundations, refractive x-ray optics are discussed in Chapter 4. A new lens shape is introduced, the so-called refractive lamellar lens (RLL), opening up new beneficial material opportunities such as aluminum oxide for nanofocusing x-ray lenses. This is made possible by the new lens design that enables one to employ coating techniques. Different lens materials with fabrication constraints in mind are discussed at the end of this chapter to highlight the prospects of refractive x-ray lenses. Emphasis is put on advantages of aluminum oxide over currently utilized silicon and on the great opportunities of available beryllium lenses for nanofocusing. Beam characterization techniques will be introduced in Chapter 5, yielding detailed and quantitative information on present aberrations. Following up on findings provided by these techniques shape errors of beryllium CRLs are identified with unprecedented accuracy. Since manufacturing constraints prohibit rapid rectification of these errors, an alternative approach of aberration correction by a phase plate is outlined. In Chapter 6 and Chapter 7 experimental results for both the first manufactured phase plates for

beryllium lenses and first RLL prototypes are presented. Their focusing quality and optics performance are assessed in both cases. Residual aberrations of the corrected beryllium lenses at various experimental sites are discussed in detail. The thesis concludes with Chapter 8, in which findings are summarized and a general approach of aberration correction for various x-ray optics is discussed. An outlook on upcoming refractive x-ray optics development and applications is given.

In this PhD thesis the improvement of current hard x-ray optics for nanofocusing based on the refraction of light, which are employed at state-of-the-art synchrotron radiation facilities, is addressed. In particular, experiments were conducted at different third generation storage ring sources, such as the Diamond Light Source (DLS), the European Synchrotron Radiation Facility (ESRF), and the PETRA III storage ring at DESY, as well as the Linac Coherent Light Source (LCLS), a new x-ray free-electron laser (XFEL). Developments, experiments and evaluation were done by our group at TU Dresden in the Institute of Structural Physics. Optics manufacturing was carried out by the Institute of Semiconductors and Microsystems at TU Dresden and the Institute of Applied Physics at the University of Jena. The project was supported by the Impuls- und Vernetzungsfond (IVF) of the Helmholtz Association of German Research Centers and the German Department of Education and Research (BMBF).

2 Theoretical Background

In order to develop, characterize, and simulate refractive optics in the hard x-ray regime a profound understanding of basic x-ray properties, their interaction with matter and the propagation of x rays in free space is of utmost importance.

As the term "refractive x-ray nanofocusing" in the title of this thesis might suggest, x rays are very similar to visible light. They can be focused by an optical element using, amongst others, the effect of refraction. Indeed, both are a part of the electromagnetic spectrum. As such, they can be described within a classical theory by electromagnetic fields with a wavelength λ, or equivalently the wavenumber $k = 2\pi/\lambda$, and a frequency ν. They are connected to each other by the dispersion relation $\lambda\nu = c$ with c being the speed of light in any given medium. Compared to visible light the wavelength of x rays is very short. Although no hard boundaries to the neighboring radiation types of ultra-violet light and gamma rays exist, typical wavelengths range from $10\,\mathrm{nm}$ down to a few pm. From a quantum mechanical standpoint the electromagnetic field can be quantized into elementary excitations, namely photons. With this the wavelength can be connected to the photon energy $E_{\mathrm{ph}} = hc_0/\lambda = \hbar\omega$, where h is Planck's constant with $\hbar = h/(2\pi)$ and the angular frequency $\omega = 2\pi\nu$. The wavelength boundaries stated before can now be expressed in photon energies ranging from $100\,\mathrm{eV}$ up to several hundreds of keV. Within this energy spectrum another differentiation is made between so-called soft x rays with photon energies not exceeding a few keV and hard x rays starting at roughly $6\,\mathrm{keV}$. In this thesis the focus lies on the latter, though a lot of the properties presented in here are also valid for soft x rays. Due to the lower photon energy of soft x rays they are absorbed very strongly in matter and even in air after short travel distances. Hard x rays on the other hand can penetrate a lot of materials very deeply and are only absorbed marginally in air. These are the properties most often associated with x rays owing to the wide utilization of hard x rays in medical applications.

In the following sections the propagation of x rays will be described based on Maxwell's equations and the phenomenon known as *diffraction*. Later on, *scattering* of x rays in matter, mainly caused by the interaction of x rays with bound electrons in atoms, is discussed.

2.1 Wave propagation in Free Space

An important question that is raised when dealing with optics and their characterization is the following: How exactly does the electromagnetic field look like within a plane at some distance apart in the propagation direction, when the current field amplitudes are known? It is not only necessary in order to understand the origin and formation of certain beam characteristics caused by the propagation of x rays through optical components, but also to be able to measure and characterize wave fields by techniques such as the Ronchi test and ptychography which will be discussed later on in this work in Chapter 5.

In the following sections a scalar wave theory will be deduced from the fundamental vectorial nature of the electromagnetic field. This approach will neglect the fact that components of the electric and

magnetic field are coupled through Maxwell's equations and cannot be treated on their own. Accurate results are obtained if the diffracting aperture is large compared to the wavelength and if the fields are not observed too close to the aperture [Goo05]. We will start by introducing the Helmholtz equation and further on deduce the integral theorem of Helmholtz and Kirchoff. From this the Fresnel-Kirchoff diffraction formula is derived and additional assumptions will be made in order to provide fast numerical solutions for describing wave fields in experimental scenarios.

2.1.1 The Helmholtz Equation

We start with the fundamental Maxwell equations [Jac98]

$$\nabla \cdot \boldsymbol{E}(\boldsymbol{r},t) = \frac{1}{\epsilon_0}\,\rho(\boldsymbol{r},t) \tag{2.1}$$

$$\nabla \times \boldsymbol{E}(\boldsymbol{r},t) = -\frac{\partial}{\partial t}\boldsymbol{B}(\boldsymbol{r},t) \tag{2.2}$$

$$\nabla \cdot \boldsymbol{B}(\boldsymbol{r},t) = 0 \tag{2.3}$$

$$\nabla \times \boldsymbol{B}(\boldsymbol{r},t) = \mu_0\,\boldsymbol{j}(\boldsymbol{r},t) + \epsilon_0\mu_0\,\frac{\partial}{\partial t}\boldsymbol{E}(\boldsymbol{r},t)\,. \tag{2.4}$$

This set of partial differential equations describe the coupled electric field $\boldsymbol{E}(\boldsymbol{r},t)$ and the magnetic induction $\boldsymbol{B}(\boldsymbol{r},t)$ in the presence of charge and current densities, $\rho(\boldsymbol{r},t)$ and $\boldsymbol{j}(\boldsymbol{r},t)$, respectively. The symbols $\times$ and $\cdot$ represent a vector cross product and a vector dot product, respectively. $\nabla = \frac{\partial}{\partial x}\boldsymbol{e}_x + \frac{\partial}{\partial y}\boldsymbol{e}_y + \frac{\partial}{\partial z}\boldsymbol{e}_z$ is the Nabla operator. For these equations we implicitly made the assumption that the wave will be propagating in a dielectric medium. Further on the medium shall be *isotropic* (properties are independent of wave polarization), *homogeneous* (constant permittivity), *nondispersive* (wavelength independent permittivity), and *nonmagnetic* (magnetic permeability equals vacuum permeability μ_0) [Goo05].

When applying $\nabla\times$ from the left to Equation (2.2) and using the known vector identity $\nabla \times (\nabla \times \boldsymbol{A}) = \nabla(\nabla\boldsymbol{A}) - \nabla^2\boldsymbol{A}$ we can insert Equation (2.1) and Equation (2.4) to retrieve the inhomogeneous wave equation

$$\left(\nabla^2 - \frac{1}{c^2}\frac{\partial^2}{\partial t^2}\right)\boldsymbol{E}(\boldsymbol{r},t) = \frac{1}{\epsilon_0}\left[\nabla\rho(\boldsymbol{r},t) + \frac{1}{c^2}\frac{\partial}{\partial t}\boldsymbol{j}(\boldsymbol{r},t)\right] \tag{2.5}$$

with $1/c^2 = \mu_0\epsilon_0$. In the same way the wave equation for the magnetic induction

$$\left(\nabla^2 - \frac{1}{c^2}\frac{\partial^2}{\partial t^2}\right)\boldsymbol{B}(\boldsymbol{r},t) = -\mu_0\nabla \times \boldsymbol{j}(\boldsymbol{r},t) \tag{2.6}$$

can be retrieved. As one can see both Equation (2.5) and Equation (2.6) are coupled to one another by the field creating charge and current densities. For the goal to find a description for wave propagation in free space it is justified to discard these source therms and view both fields far away from any charged particles. This yields the homogeneous wave equations

$$\left(\nabla^2 - \frac{1}{c^2}\frac{\partial^2}{\partial t^2}\right)\boldsymbol{E}(\boldsymbol{r},t) = 0\,,$$

$$\left(\nabla^2 - \frac{1}{c^2}\frac{\partial^2}{\partial t^2}\right)\boldsymbol{B}(\boldsymbol{r},t) = 0\,.$$

Since this vector wave equation is obeyed by both $\boldsymbol{E}$ and $\boldsymbol{B}$, an identical scalar wave equation, e. g.

$$\left(\nabla^2 - \frac{1}{c^2}\frac{\partial^2}{\partial t^2}\right) E_x(\boldsymbol{r}, t) = 0 \,, \tag{2.7}$$

is fulfilled by all components of those vectors [Goo05]. Therefore, the electromagnetic field and the behavior of all components of $\boldsymbol{E}$ and $\boldsymbol{B}$ can be described by a single *complex* scalar wave field $\Psi(\boldsymbol{r}, t)$ [GW53]. This time-dependent wave field can be separated with a spectral decomposition by the use of a Fourier transform. We hereby obtain a superposition of monochromatic fields $\psi_\omega(\boldsymbol{r})$:

$$\Psi(\boldsymbol{r}, t) = \frac{1}{\sqrt{2\pi}} \int_0^\infty \psi_\omega(\boldsymbol{r}) e^{-\mathrm{i}\omega t} d\omega \,. \tag{2.8}$$

The subscript ω denotes again the angular frequency of the monochromatic wave field $\psi_\omega(\boldsymbol{r})$. By inserting Equation (2.8) into Equation (2.7) one can see that the amplitude $\psi_\omega(\boldsymbol{r})$ is indeed a solution of the time-independent wave equation

$$\left(\nabla^2 + k^2\right) \psi_\omega(\boldsymbol{r}) = 0$$

with $k = \omega/c = 2\pi/\lambda$, better known as the *Helmholtz equation*. This approximation is especially suited in the context of x rays. The representation of the complex amplitude by monochromatic fields $\psi_\omega(\boldsymbol{r})$ demands that the function only varies slowly with $\boldsymbol{r}$ compared to the radiation wavelength λ $\left(\left|\nabla^2\psi_\omega\right| \ll |k \cdot \nabla\psi_\omega|\right)$. This inherently implies that $\psi_\omega(\boldsymbol{r})$ is representing waves that are propagating in forward direction (small angle approximation) and that no inhomogeneities at wavelength scale are present. Both conditions are met in x-ray optics due to the small wavelength of x rays and their weak interaction with matter as we will see in Section 2.2.

2.1.2 Integral Theorem of Helmholtz and Kirchoff

The basic principle on which the later derived diffraction formula of *Fresnel-Kirchhoff* relies on is the integral theorem presented here. Foundation to this is *Green's theorem*, well known from text books of advanced calculus. Let $U(P)$ and $G(P)$ be any two complex-valued functions of position, and let S be a surface surrounding a volume V. When U, G and their partial derivatives exist and are continuous within and on S, then

$$\iiint_V \left(U\nabla^2 G - G\nabla^2 U\right) dv = \iint_S \left(U\frac{\partial G}{\partial n} - G\frac{\partial U}{\partial n}\right) ds \tag{2.9}$$

holds, where $\partial/\partial n$ denotes a partial derivative in the outward normal direction on S.
We will now use the Helmholtz equation to find the field amplitudes $\psi(P_0)$ in a point $P_0 = \boldsymbol{r}_0$ if the field amplitudes and its derivatives on an arbitrary surface S, surrounding P_0, are known. Following Kirchhoff we choose an auxiliary function G that is given at any point P_1 by

$$G(P_1) = \frac{e^{\mathrm{i}kr_{01}}}{r_{01}} \,. \tag{2.10}$$

This is the so-called *free space* Green's function, an unit-amplitude spherical wave expanding from point P_0, where $r_{01} = ||\boldsymbol{r}_{01}|| = ||\overrightarrow{P_0P_1}||$. To circumvent the problem of the discontinuity of G at P_0 we introduce a small spherical surface S_ϵ of radius ϵ, surrounding P_0 (cf. Figure 2.1). Green's theorem will then be applied to the volume V', surrounded from the outside by S and from the inside by S_ϵ. Within

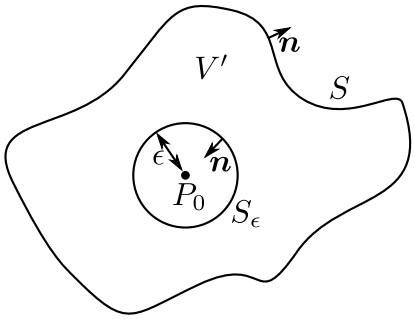

Figure 2.1: Schematic of the surfaces of integration (following [BW80; Goo05]). The central spherical surface surrounds the discontinuity of G with $\epsilon \to 0$.

the volume V' both ψ and G shall fulfill the Helmholtz equation $\nabla^2\psi = -k^2\psi$ and $\nabla^2 G = -k^2 G$ with identical wave number k. When we substitute these two Helmholtz equations into the left hand side of Green's theorem (2.9) the integrand of the volume integral vanishes and the theorem simplifies to

$$\iint_{S'} \left(\psi \frac{\partial G}{\partial n} - G\frac{\partial \psi}{\partial n}\right) ds = 0$$

with $S' \coloneqq S \cup S_\epsilon$ or

$$-\iint_{S_\epsilon} \left(\psi \frac{\partial G}{\partial n} - G\frac{\partial \psi}{\partial n}\right) ds = \iint_{S} \left(\psi \frac{\partial G}{\partial n} - G\frac{\partial \psi}{\partial n}\right) ds \,.$$

In order to evaluate these integrals we calculate the gradient of Equation (2.10) on the outer surface S to

$$\frac{\partial G(P_1)}{\partial n} = \cos\left(\boldsymbol{n}, \boldsymbol{r}_{01}\right) \left(\mathrm{i}k - \frac{1}{r_{01}}\right) \frac{e^{\mathrm{i}kr_{01}}}{r_{01}} \,. \tag{2.11}$$

For the inner surface, where P_1 is on S_ϵ, $\cos\left(\boldsymbol{n}, \boldsymbol{r}_{01}\right) = -1$, and Equation (2.11) becomes

$$\frac{\partial G(P_1)}{\partial n} = \left(\frac{1}{\epsilon} - \mathrm{i}k\right) \frac{e^{\mathrm{i}k\epsilon}}{\epsilon} \quad \text{with} \quad G(P_1) = \frac{e^{\mathrm{i}k\epsilon}}{\epsilon} \,.$$

With these results and the continuity of ψ at P_0 we can evaluate the integration over the inner surface S_ϵ in the limit

$$\begin{aligned} \lim_{\epsilon\to 0} \iint_{S_\epsilon} \left(\psi \frac{\partial G}{\partial n} - G\frac{\partial \psi}{\partial n}\right) ds &= \lim_{\epsilon\to 0} 4\pi\epsilon^2 \left[\psi(P_0) \left(\frac{1}{\epsilon} - \mathrm{i}k\right) \frac{e^{\mathrm{i}k\epsilon}}{\epsilon} - \frac{\partial \psi(P_0)}{\partial n} \frac{e^{\mathrm{i}k\epsilon}}{\epsilon}\right] \\ &= 4\pi\psi(P_0) \,. \end{aligned}$$

We are now ready to finally substitute this result in Figure 2.1.2 to obtain

$$\psi(P_0) = \frac{1}{4\pi} \iint_S \left[\frac{\partial \psi}{\partial n} \left(\frac{e^{\mathrm{i}kr_{01}}}{r_{01}}\right) - \psi \frac{\partial}{\partial n} \left(\frac{e^{\mathrm{i}kr_{01}}}{r_{01}}\right)\right] ds \,, \tag{2.12}$$

which relates the known wave field on the surface S with the observable amplitudes ψ at point P_0, also known as the integral theorem of Helmholtz and Kirchhoff. This important result will now be used to derive the diffraction formula of Fresnel-Kirchhoff.

2.1.3 The Fresnel-Kirchoff Diffraction Formula

To further develop our understanding of the propagation of an electromagnetic field in free space we now consider the illumination of an opaque screen with an aperture Σ, that is illuminated by a spherical wave, originating from P_2 (cf. Figure 2.2). We are interested in the field amplitude behind the screen in

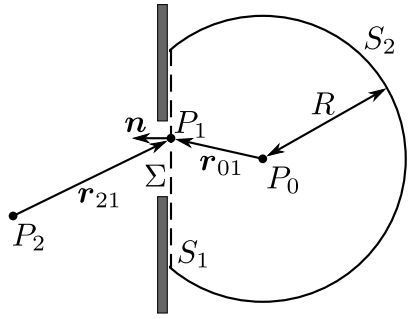

Figure 2.2: Schematic of the illumination of an opaque plane screen with opening Σ by a point source in P_2. We search for the field amplitudes in P_0 by integrating over the closed surface $S_1 \cup S_2$ (following [BW80; Goo05]).

P_0. We will now use the beforehand derived integral Theorem in Equation (2.12) to calculate $\psi(P_0)$ by a prudent choice of the surrounding surface, consisting of the disjoint parts S_1 and S_2, and by making approximations that are fulfilled in almost any cases, especially for hard x rays with wavelength below a few nm. To start we apply Equation (2.12) to this problem with

$$\psi(P_0) = \frac{1}{4\pi} \iint_{S_1 \cup S_2} \left(\frac{\partial \psi}{\partial n} G - \psi \frac{\partial G}{\partial n} \right) ds \,. \tag{2.13}$$

To perform this integration knowledge of the field amplitudes on the whole surface $S_1 \cup S_2$ is necessary. However, we can make assumptions that will allow us to only regard the screen opening Σ. First, we make an assumption about the wave field directly behind the opaque screen, also known as the *Kirchhoff boundary conditions*. First of all across Σ the field distribution ψ and its derivative $\partial\psi/\partial n$ are exactly the same as without the screen. Secondly the field ψ and its derivative $\partial\psi/\partial n$ are identically zero in the shadow of the opaque screen, that is the surface $S_1 \setminus \Sigma$. What remains is the spherical surface S_2, surrounding P_0. The suggestion made in [BW80] assumes that the radiation field does not exist at all times, but that a source begins to radiate at some time t_0. If the field is evaluated in P_0 at t_1, no radiation from S_2 can have reached P_0 if $R > c(t_1 - t_0)$. However, this requires a depart from strict monochromatic waves. Another interesting approach made in [Goo05] relies on the *Sommerfeld radiation condition* [Som49]. It states that ultimately only *outgoing* waves have to be dealt with at S_2 when R becomes arbitrarily large. In any case we now might also disregard the integration over S_2. Another simplification of Equation (2.13) can be obtained by assuming that the distances r_{21} and r_{01} from the source and the observation point to the screen, respectively, are large compared to the wavelength of the radiation, implying $k \gg 1/r_{21}$ and $k \gg 1/r_{01}$. This simplifies the gradient of the disturbances (cf. Equation (2.11)), when we again assume Green's free space function G (cf. Equation (2.10)) and a spherical wave as the emitting source from P_2 with an amplitude A. With this we can deduce

$$\begin{aligned} \psi(P_0) &= \frac{A\mathrm{i}k}{4\pi} \iint_{\Sigma} \frac{e^{\mathrm{i}k(r_{21}+r_{01})}}{r_{21} r_{01}} \left[\cos(\boldsymbol{n}, \boldsymbol{r}_{21}) - \cos(\boldsymbol{n}, \boldsymbol{r}_{021})\right] ds \\ &= \frac{\mathrm{i}k}{4\pi} \iint_{\Sigma} \psi(P_1) G(P_1) \left[\cos(\boldsymbol{n}, \boldsymbol{r}_{21}) - \cos(\boldsymbol{n}, \boldsymbol{r}_{021})\right] ds \,, \end{aligned} \tag{2.14}$$

which is known as the *Fresnel-Kirchhoff diffraction formula*. It relates the known intensity of point P_1 in a plane Σ to the observable field in P_0 very accurately. Despite some inconsistencies arising from the imposed boundary conditions on both the field strength and its derivate in the aperture plane, a comparison with the more consistent *Rayleigh-Sommerfeld solution* shows, that both are identical under the assumption of small angles. This implies that the distances from P_0 and P_2 to Σ must be large compared to the aperture's diameter [WM64], meaning both P_0 and P_2 are in the *far field* of the plane. These and other approximations will be discussed in the following section in order to simplify analytic treatment in the simulations and phase retrieval algorithms used in this thesis.

2.1.4 From Fresnel to Fraunhofer Diffraction

It can be shown that the *Huygens-Fresnel principle* follows from the Fresnel-Kirchhoff diffraction formula. It states that Equation (2.14) can also be interpreted as that the field at P_0 arises from an infinite number of artificial secondary point sources located in the diffraction aperture. In the following considerations we want to describe the field $\psi_{z_1}(x, y)$ in a plane located at $z = z_1$ by the known distribution $\psi_{z_0}(\zeta, \eta)$ in the plane $z = z_0$. Therefore, we will now move to rectangular coordinates. The given geometry is outlined in Figure 2.3.

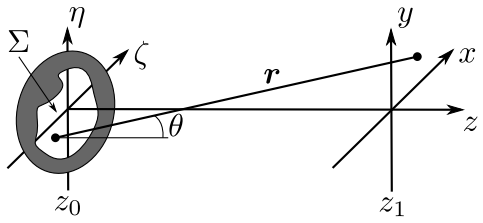

Figure 2.3: Schematic of the diffraction geometry. The observation plane (x, y) is located at $z = z_1$ and the diffraction plane (ζ, η) at $z = z_0$ with the aperture Σ (following [Goo05]).

Within these coordinates the Huygens-Fresnel principle can be expressed as

$$\psi_{z_1}(x, y) = -\frac{\mathrm{i}k}{4\pi} \iint_{\Sigma} \psi_{z_0}(\zeta, \eta) \frac{e^{\mathrm{i}kr}}{r} \cos\theta \, d\zeta d\eta \, . \tag{2.15}$$

Let's assume that the propagation distance $\Delta z = z_1 - z_0$ is large compared to the aperture opening, so that we can approximate $\cos\theta \approx 1$ with θ being the angle between the outward normal $\boldsymbol{n}$ and the vector $\boldsymbol{r}$. Investigating the latter a bit closer we can calculate $r = \sqrt{\Delta z^2 + (x-\zeta)^2 + (y-\eta)^2}$ exactly. In order to reduce Equation (2.15) to a more simple and usable term we may rewrite $r = \Delta z\sqrt{1+b}$ with $b = [(x-\zeta)/\Delta z]^2 + [(y-\eta)/\Delta z]^2 < 1$. With the binomial expansion of the square root we can approximate $\sqrt{1+b} = 1 + (1/2)b - (1/8)b^2 + \cdots$, where the number of terms that is required for a certain accuracy greatly depends on the magnitude of b. But we also have to distinguish between the two occurrences of r in Equation (2.15). For the appearance of r in the exponent small errors are critical. On the one hand r is multiplied by a very large number $k > 10^8\,\mathrm{m}^{-1}$ (typically $\lambda < 10\,\mathrm{nm}$), on the other hand the value of the exponential varies significantly even for phase changes of a fraction of 2π. With this in mind we will consider the first two terms of the expansion in the exponent, whereas for the appearance in the denominator we will abort the expansion after the first term $r \approx \Delta z$. With these approximations we have obtained

$$\psi_{z_1}(x, y) = -\frac{\mathrm{i}k}{4\pi} \frac{e^{\mathrm{i}k\Delta z}}{\Delta z} \iint_{-\infty}^{+\infty} \psi_{z_0}(\zeta, \eta) e^{\frac{\mathrm{i}k}{2\Delta z}\left[(x-\zeta)^2 + (y-\eta)^2\right]} d\zeta d\eta \, , \tag{2.16}$$

where the finite aperture limits are incorporated into the definition of $\psi_{z_0}(\zeta,\eta)$. We may also regard Equation (2.16) as a convolution to be expressed as

$$\psi_{z_1}(x,y) = \iint_{-\infty}^{+\infty} \psi_{z_0}(\zeta,\eta) K_{\Delta z}(x-\zeta, y-\eta) d\zeta d\eta \tag{2.17}$$

with the convolution or propagator kernel

$$K_{\Delta z}(x,y) = -\frac{\mathrm{i}k}{4\pi}\frac{e^{\mathrm{i}k\Delta z}}{\Delta z} e^{\frac{\mathrm{i}k}{2\Delta z}(x^2+y^2)} .$$

For later applications it will be useful to define the short form $\psi_{z_1} = \mathcal{K}_{\Delta z}\psi_{z_0}$ with the propagation operator

$$(\mathcal{K}_{\Delta z}\bullet)(x,y) = \iint_{-\infty}^{+\infty} \bullet(\zeta,\eta) K_{\Delta z}(x-\zeta, y-\eta) d\zeta d\eta . \tag{2.18}$$

With the well known *convolution theorem* we can express Equation (2.17) also as a multiplication in Fourier space, with the Fourier transform denoted by the operator $\mathcal{F}$, as

$$\psi_{z_1} = \mathcal{F}^{-1}\left\{\mathcal{F}\left\{\psi_{z_0}\right\} \cdot \mathcal{F}\left\{K_{\Delta z}\right\}\right\} .$$

Computationally this is very useful, since the propagation may by calculated in only three steps using the very efficient *fast Fourier transform*. While the formalisms discussed until now are useful to propagate wave fields by small distances $\Delta z \lesssim kD^2$ with D being the largest lateral expanse of the diffraction aperture Σ, an even faster approach with a scalable pixel size in a discrete two-dimensional field is necessary to speed-up large distance propagation. Since we mostly deal with divergent waves the lateral extend of the wave field varies greatly between larger propagation distances. On the one hand we need a sufficiently small pixel size to map all features of the small wave field. On the other hand the extended wave field after propagation would require a large pixel array to cover the whole wave field extend. With the now discussed approach this problem is solved by introducing a scalable discrete pixel size due to properties of the discrete fast Fourier transform, which will allow us to reduce the necessary array size significantly. The result from Equation (2.16) can be rewritten if one factors out the term $\exp[\mathrm{i}k/(2\Delta z)(x^2+y^2)]$, leading to

$$\psi_{z_1}(x,y) = -\frac{\mathrm{i}k}{4\pi}\frac{e^{\mathrm{i}k\Delta z}}{\Delta z} e^{\frac{\mathrm{i}k}{2\Delta z}(x^2+y^2)} \iint_{-\infty}^{+\infty} \left[\psi_{z_0}(\zeta,\eta) e^{\frac{\mathrm{i}k}{2\Delta z}(\zeta^2+\eta^2)}\right] e^{\frac{\mathrm{i}k}{\Delta z}(x\zeta+y\eta)} d\zeta d\eta .$$

It can be seen that, in the scope of Fresnel diffraction, the observed field $\psi_{z_1}(x,y)$ can be found by the Fourier transform of the product of $\psi_{z_0}(\zeta,\eta)$ with a quadratic phase function. If we now enforce the even stronger approximation $\Delta z \gg k(\zeta^2+\eta^2)_{\max}$, than the phase term is unity over the entire aperture and the observable wave field in the *far field* region is described by *Fraunhofer diffraction*

$$\psi_{z_1}(x,y) = -\frac{\mathrm{i}k}{4\pi}\frac{e^{\mathrm{i}k\Delta z}}{\Delta z} e^{\frac{\mathrm{i}k}{2\Delta z}(x^2+y^2)} \iint_{-\infty}^{+\infty} \psi_{z_0}(\zeta,\eta) e^{\frac{\mathrm{i}k}{\Delta z}(x\zeta+y\eta)} d\zeta d\eta ,$$

which turns out to be a simple Fourier transform of $\psi_{z_0}(\zeta,\eta)$ with an additional phase factor. The relation between discrete pixel sizes for the fast Fourier transform is given with $\Delta x \Delta\zeta = 2\pi/N$, where N denotes the array size in this dimension. This formalism will be employed extensively in the phase

retrieval algorithm used in this work to reconstruct the wave field in the sample plane by measuring the intensity distribution of the wave field in the far field with a two-dimensional pixel detector.

2.2 Interaction with matter

The theoretical foundation for the interaction of x rays with matter was already given by Maxwell's equations (2.1) - (2.4). While we deduced the propagation in free space by neglecting explicitly any free charges, these field creating charge and current densities are now considered. The electromagnetic field can interact with these charges and accelerate them. The electromagnetic field that is now emitted from these accelerated charges can be deduced from the inhomogeneous wave equations (2.5) and (2.6) by using *Green's function* and the *Fourier-Laplace transform*, described in [Jac98; Att00]. This interaction process on an atomic level is referred to as *scattering*, where the incident electromagnetic wave can change direction and even energy. When the latter occurs one speaks of *inelastic scattering*, touched briefly in Section 2.2.4. If no energy loss occurs, the term *elastic scattering* is used. When deriving the *complex index of refraction* in the following section we will notice that the macroscopic phenomenon of refraction is related to elastic scattering on charged particles in solids.

2.2.1 From Free to Bound Electrons

In general the process of scattering is described by the scattering cross section σ, which is an effective area that delineates the likelihood of a scattering event. It relates the total scattered flux to the incident one on the target, whereas the differential cross section $d\sigma/d\Omega$ gives an intrinsic rate of a scattering event into a certain solid angle Ω. Scattering occurs due to the driven electron oscillation caused by the electric field of the incident wave impinging on an atom. The electric field accelerates the free electron, causing it to oscillate and radiate by itself. The emitted radiation is referred to as dipole radiation. The scattering process is described by

$$\sigma_e = \frac{8\pi}{3} r_e^2 \qquad \text{and} \qquad \left(\frac{d\sigma}{d\Omega}\right)_{\text{Thomson}} = r_e \sin^2\Theta \qquad \text{with} \qquad r_e = \frac{e^2}{4\pi\epsilon_0 m_e c^2} \,,$$

where r_e is the classical electron radius, e the particle charge, m_e the rest mass, and Θ describes the angle between the acceleration vector of the electron $\boldsymbol{a}$ and the scattered wave vector $\boldsymbol{k'}$ (cf. Figure 2.4). Since these results were first derived by J. J. Thomson, this kind of scattering is also called *Thomson scattering*. One can see that the cross section is independent of the wavelength but $r_e \propto 1/m_e$. Since the proton is 1839 times heavier than the electron, scattering from protons can be neglected here.

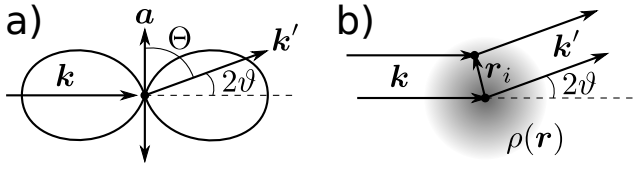

Figure 2.4: Scattering on free and bound electrons. a) Scattering on a single electron. b) Scattering on an atom with multiple electrons, displaced by $\boldsymbol{r}_i$.

When moving forward from free to bound electrons in atoms the full description of scattering processes based on quantum mechanics is rather complicated [Jam54]. Here, we want to follow the semi-classical model and treat each electron as a damped harmonic oscillator with eigenfrequencies w_j and the damping

parameter γ. The location of each electron within the atom shall be given by the displacement vector $\boldsymbol{r}_j$. It is also convenient to use the scattering angle 2ϑ between the incident and scattered wave vectors (cf. Figure 2.4), so that the *scattering vector* $\boldsymbol{q} = \boldsymbol{k} - \boldsymbol{k}'$ and $|\boldsymbol{q}| = 2|\boldsymbol{k}| \sin\vartheta$. The total scattering on an atom can now be described as a summation over all bound electrons within that atom, when taking into account the individual phase shift $\Delta\phi_j = \boldsymbol{q}\boldsymbol{r}_j$ of each electron due to its displacement. The differential scattering cross section for such an atom can now be written as [FM10]

$$\left(\frac{d\sigma}{d\Omega}\right) = \left(\frac{d\sigma}{d\Omega}\right)_{\text{Thomson}} |f(\boldsymbol{q},\omega)|^2 \qquad \text{with} \qquad f(\boldsymbol{q},\omega) = \sum_{j=1}^{Z} g_j \frac{\omega^2 e^{-\mathrm{i}\boldsymbol{q}\boldsymbol{r}_j}}{\omega^2 - \omega_j^2 + \mathrm{i}\gamma\omega} \,.$$

Here, we added the oscillator strength g_j with $\sum_j g_j = Z$. In the semi-classical approach each electron within the atom has only a single resonance frequency w_j. In reality, however, when using a quantum mechanical model, each electron has a multitude of possible transitions with differing transition probabilities. Historically, to account for this discrepancy in the semi-classical model, the term of the oscillator strength was added to the *atomic form factor* $f(\boldsymbol{q},\omega)$. Furthermore it is common to split up $f(\boldsymbol{q},\omega) = f_0(\boldsymbol{q}) + f'(\omega) + \mathrm{i}f''(\omega)$ by separation into real and imaginary parts. The first expression $f_0(\boldsymbol{q})$ can be interpreted as the Fourier transform of the electron density $\rho(\boldsymbol{r})$ of the atom, if we move from localized electrons to a distributed charge density with $f_0(\boldsymbol{q}) = \int d\boldsymbol{r}\rho(\boldsymbol{r}) \exp[-\mathrm{i}\boldsymbol{q}\boldsymbol{r}]$. It depends on the scattering vector $\boldsymbol{q}$. But in the limit of long wavelength being greater than the atom size and also for forward scattering $|\boldsymbol{q}\boldsymbol{r}| \to 0$ it follows in both cases that $f_0(\boldsymbol{q}) \to f_0 = Z$. However, in the hard x-ray regime, the wavelength is well within atomic dimensions. Instead we consider the weak interaction of x rays with matter, where we can assume single scattering, also known as the kinematic model or *Born's approximation*, and account only for forward scattering. The dispersion corrections $f'(\omega)$ and $f''(\omega)$ are strictly speaking also dependent on $\boldsymbol{q}$, but since relevant eigenfrequencies of electrons only exist in the highly localized core levels of the atom, the dependency is very weak and can be neglected.

2.2.2 The Refractive Index

With the given model of the damped harmonic oscillator for electrons driven by an electromagnetic field one can derive a current density $\boldsymbol{j}(\boldsymbol{r},t)$ for the incident wave [FM10]. Substituting this into Equation (2.5) and comparing the result with the standard form of the wave equation

$$\left(\nabla^2 - \frac{n^2(\omega)}{c^2}\frac{\partial^2}{\partial t^2}\right)\boldsymbol{E}(\boldsymbol{r},t) = 0 \,,$$

where $n(\omega)$ is the energy-dependent refractive index, shows that

$$n(\omega) = 1 - \frac{n_a}{2\pi} r_e \lambda^2 \left(f_0 + f'(\omega) - \mathrm{i}f''(\omega)\right) \,.$$

Here, n_a is the atomic number density given by $n_a = \rho N_A/M$ with N_A being Avogadro's number, ρ the mass density, and M the molar mass of the material. Since the dispersive elements f' and f'' are typically very small in the x-ray regime, the refractive index is often written as

$$n(\omega) = 1 - \delta + \mathrm{i}\beta \,. \tag{2.19}$$

The decrement δ is typically in the range 10^{-7} to 10^{-5}, indicating the extremely weak refraction of x rays. The imaginary part β is describing attenuation effects. By comparison one finds

$$\delta = \frac{n_a}{2\pi} r_e \lambda^2 \left(Z + f'(\omega)\right) \tag{2.20}$$

and

$$\beta = \frac{n_a}{2\pi} r_e \lambda^2 f''(\omega) \tag{2.21}$$

The real part of the refractive index is thus slightly smaller than unity, consequences will be discussed in Section 2.2.5. In general both δ and β are not independent of one another. While the real part describes a change in the velocity of the electromagnetic wave, the imaginary part refers to absorption. Both parts are connected through the model of harmonic oscillators in the semi-classical approach or transition probabilities in the quantum mechanical view. In practice, they are related by the *Kramers-Kronig relations* [Kro26].

2.2.3 The Transmission Operator

For an elegant description of the interaction of x rays with matter within the modeling of x-ray optics or methods of phase retrieval, the introduction of a transmission operator $\mathcal{T}_{\Delta z}$ is very useful. However, the sample is required to be thin. While the wave field propagates through the sample it is implicated that no significant change in the wave-field extent nor an alternation of the propagation direction is observed. With this the exiting wave field ψ after the sample can be described by the simple multiplication

$$\psi = \mathcal{T}_{\Delta z} \psi_0 \, .$$

The transmission operator is further defined by integrating along the propagation direction z through the sample thickness Δz by

$$(\mathcal{T}_{\Delta z} \bullet)(x,y) = \bullet(x,y) \cdot e^{\mathrm{i}k \int\limits_{z=0}^{\Delta z} dz\, n(x,y,z)} = \bullet(x,y) \cdot e^{\mathrm{i}k\Delta z} e^{\mathrm{i}k \int dz\, \delta(x,y,z)} e^{-k \int dz\, \beta(x,y,z)} \, . \tag{2.22}$$

The material causes an additional phase shift induced by δ and the magnitude of the field amplitude is reduced by β.

2.2.4 Attenuation

The reduction in field amplitude is experimentally observed by a decrease of intensity I, since current detectors measure x-ray radiation through secondary processes that arise from primary absorption of radiation or energy losses. As a side note it should also be mentioned that the phase of the field is lost in this detection process, giving rise to phase retrieval methods discussed later. Since $I \propto |\psi|^2$, with Equation (2.22) we can write $|\psi|^2 = |\mathcal{T}_{\Delta z}\psi_0|^2 = |\psi_0|^2 \exp[-2k \int dz\, \beta]$. By defining the linear attenuation coefficient

$$\mu(x,y,z) = \frac{4\pi}{\lambda} \beta(x,y,z)$$

we find

$$I_{\Delta z}(x,y,z) = I_0 \cdot e^{-\int_{z=0}^{\Delta z} dz\, \mu(x,y,z)} ,$$

which is a generalized form of *Lambert-Beer's law* for a z-dependent attenuation coefficient. The intensity of the field is decreased exponentially when propagating through any given medium.

Several physical processes contribute to attenuation as there are absorption (photoelectric absorption and pair production) and scattering (elastic Rayleigh and inelastic Compton scattering). Elastic Rayleigh scattering takes on a special role and is the cause for multiple phenomena. Parts of this signal are responsible for the refraction of x-rays inside the material, which is exploited in refractive x-ray lenses (cf. Chapter 4). Diffraction in samples due to elastic scattering will also be the relevant signal for coherent imaging techniques discussed in Chapter 5. A special case of diffraction occurs for periodically structured materials, e. g. single crystals, polycrystalline objects or even microscopically structured samples, where a significant fraction of the incident beam can be diffracted into certain angles. If scattering occurs at crystal lattices one speaks of *Bragg-Laue* diffraction. For the considerations here the material is not periodic and the intensity is measured before and after the sample in an infinitesimal small detector, so that contributions from scattered x rays in forward direction become negligible. Each of these processes contributes additively and independently of one another to the total attenuation coefficient μ_{total} with

$$\mu_{\text{total}} = \sum_i \mu_i = \mu_{\text{photo}} + \mu_{\text{compton}} + \mu_{\text{bragg}} + \mu_{\text{pair}} .$$

The attenuation coefficients can be derived from the scattering cross section of the individual process with $\mu_i = dN/dV\sigma_i$. In addition to linear absorption coefficients, the mass attenuation coefficient μ/ρ is often used in literature and databases to provide a density independent measure.

The strongest contributions to attenuation within typical x-ray energies are made by photo absorption for lower energies and Compton scattering towards higher photon energies, typically well above $10\,\text{keV}$. A plot highlighting the interplay of all these contributions to the total mass attenuation coefficient μ/ρ is shown in Figure 2.5. Also μ/ρ for a few other x-ray optically relevant materials is shown. The high-Z element tungsten is not used in refractive optics discussed later, but is used often in test structures, guard slits or diffractive optics like Fresnel zone plates (cf. Chapter 4).

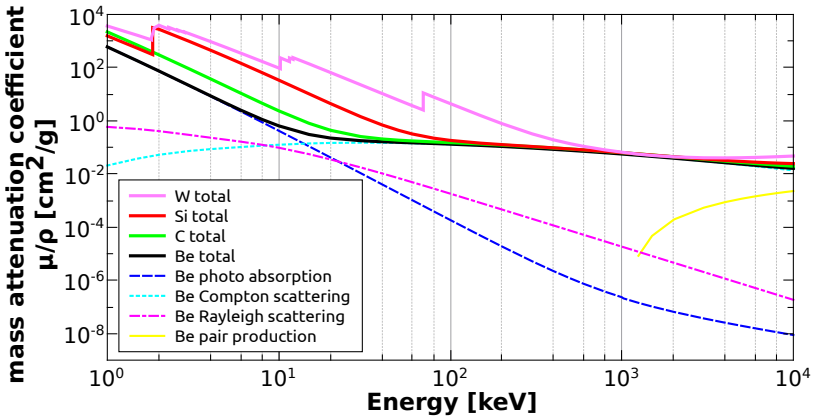

Figure 2.5: Total μ/ρ for a few relevant materials in this work. Contributions to the total mass attenuation coefficient of Be are shown to highlight the strength of each process.

Photoelectric absorption describes the extinction of an incident photon while interacting with a bound electron within the atom. The whole energy E_{ph} of the photon is transferred to the atom and excites it. In this process an electron is raised from its bound state into a free state with a certain kinetic energy $E_{\mathrm{kin}} = E_{\mathrm{ph}} - E_{\mathrm{b}}$, where E_{b} is the binding energy of the initial electron state. The cross section σ_{photo} scales roughly by Z^4/E_{ph}^3 [AM11]. After the emission of the free photoelectron the atom is in an excited state. The vacant state can be populated again by secondary processes, emitting fluorescence radiation or Auger electrons that can be used to further study the irradiated material [Jen99; BG03].
The scattering processes can be divided in coherent Rayleigh and incoherent Compton scattering. Both describe the interaction of x rays with bound electrons. An important variable is the energy of the x-ray photon E_{ph}, that determines if Rayleigh or Compton scattering is more dominant. The former is dominant if $E_{\mathrm{ph}} \ll E_{m_e}$, with E_{m_e} being the energy equivalent of the rest mass of the electron m_e. However, the effect is strongly overlain by photoelectric absorption, since at the same time $E_{\mathrm{ph}} \approx E_{\mathrm{b}}$. With rising photon energies the probability increases to transfer energy to the electron, since $E_{\mathrm{ph}} \lessapprox E_{m_e}$. The loss in energy is readily calculated when considering the conservation of energy and momentum during the collision. Compton scattering takes over in the total mass attenuation coefficient, since photo absorption falls off as $1/E_{\mathrm{ph}}^3$.
The last effect to discuss is pair production. If $E_{\mathrm{ph}} > 2m_e$ the possibility exists to create an electron-positron pair in the strong electric field of the atoms nucleus. However, experiments at these energies are far beyond the scope of this work and the effect can be neglected.

2.2.5 Refraction and Reflection

So far, the interaction of x rays with matter was discussed on an atomic level. With these results and an understanding for the underlying principles we are now looking at the macroscopic effects of *refraction* and *reflection*. These phenomena are entirely described by the already known index of refraction n (cf. Equation (2.19)). As we have noticed beforehand, for x rays $n = 1 - \delta \lessapprox 1$, since δ is positive and in the range 10^{-7} to 10^{-5}, whereas in contrast for visible light with $n > 1$ and typical values of n in the range 1.3 to 1.6. Here, we want to highlight consequences of the refractive index being slightly smaller than unity for x rays. The situation is depicted in Figure 2.6.

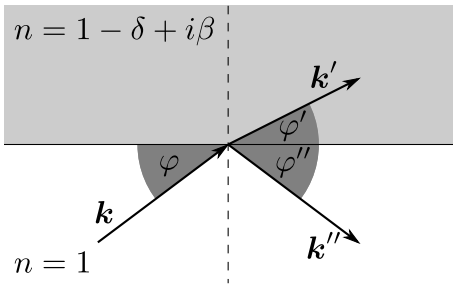

Figure 2.6: Refraction and reflection of x rays at a sharp interface between vacuum ($n = 1$) and matter ($n < 1$).

A plane wave with wave vector $\boldsymbol{k}$ in vacuum enters a medium at an angle φ with respect to its surface. Interactions give rise to two secondary waves. One is the refracted wave under an angle φ' and corresponding wave vector $\boldsymbol{k}'$ inside the medium. The other is reflected back into the vacuum under an angle $\varphi'' = \varphi$ with a wave vector $\boldsymbol{k}''$. The refraction angles φ and φ' are related to one another by Snell's law

$$n \cos \varphi' = \cos \varphi \, .$$

As for x rays vacuum is the optically densest material with $n = 1$, rays are refracted away from the surface normal and towards the surface, hence $\varphi' < \varphi$. Besides these angles, one is often interested in the intensity of the refracted and reflected fields, called *refractivity* and *reflectivity*. These calculations can be carried out using the *Fresnel equations* [AM11]. Note that these calculations treat *specular* reflectivity, which means that the reflected intensity is confined to the plane spanned by the incident wave and the surface normal and further $\varphi'' = \varphi$. Other reflectivity is produced by rough surfaces, which plays an important role for x-ray mirrors. For refractive optics surface roughness is only a minor concern (cf. Section 4.3.2).
In the limit $\varphi' \to 0$ the incident wave field can no longer propagate into the medium. Instead, one observes *external* total reflection. From Snell's law it is evident that for all incident angles φ smaller than the critical angle

$$\varphi_c = \arccos n \approx \sqrt{2\delta}$$

the incident wave is completely reflected. Only an evanescent wave enters the medium, allowing, for example, the study of surface effects through external total reflection.

3 X-Ray Sources

Over the past century x-ray sources have made a tremendous development. At the beginning of the 20th century x-ray tubes were the only available sources for x rays. In these devices free electrons are created in a glowing filament and accelerated towards a water-cooled metal anode. The impinging electrons create two distinct components of x-ray radiation. A continuous spectrum is emitted due to the deceleration of electrons within the anode material and is known as *bremsstrahlung*. Due to conservation of energy the maximum photon energy corresponds to the kinetic energy of the electrons hitting the anode. The other component, the fluorescent radiation, is created when impinging electrons collide with bound electrons of the anode material and create a vacant state in the atom. The vacancy is populated again by a transition of an electron from a lower bound state into this vacancy. An x-ray photon may be emitted in this process with a characteristic energy corresponding to the energy difference between the two states. The design of the tube allows one to control the kinetic energy of the electrons as well as the electron current. The main limitation is given by the ability to cool the anode efficiently. Over the decades several new types became available, e. g. the rotating anode x-ray tube, microfocus x-ray tubes, or liquid-metal-jet x-ray tubes [HOH03].

However, the problem of an x-ray tube is not only the very inefficient creation of x rays and the resulting high heat load on the anode, but also the fact that the created radiation is emitted into a full solid angle of 4π, whereas experimentally a beam with small angular divergence is desired. In order to characterize x-ray sources a figure of merit was established, the so-called brilliance $\mathcal{B}$. It gives a measure of the emitted photons per second that originate from a certain source size with a given divergence and spectral distribution. The brilliance is defined as

$$\mathcal{B} = \frac{F}{\Sigma_\mathrm{h}\Sigma_\mathrm{v}\Sigma'_\mathrm{h}\Sigma'_\mathrm{v} \cdot \frac{\Delta E_\mathrm{ph}}{E_\mathrm{ph}}} \,, \tag{3.1}$$

with the photon flux F defined as photons per time interval, the horizontal and vertical source size Σ_h and Σ_v, and the source divergence Σ'_h and Σ'_v. The bandwidth $\Delta E_\mathrm{ph}/E_\mathrm{ph}$ is defined to be 10^{-3}. The unit of brilliance is defined as $[\mathcal{B}] = \mathrm{photons/s/mm^2/mrad^2/0.1\%}$.

After the invention of the x-ray tube no significant increase in brilliance could be achieved with the given principle, even by further developed models at the end of the 20th century. By accident an unwanted radiation was discovered by high-energy physicists in 1947, the so-called *synchrotron radiation* [Eld+47], emitted by particles accelerated to relativistic energies describing a circular path. The name is taken from a specific type of particle accelerator used at that time. Nowadays, synchrotron radiation has become a generic term. It describes emitted radiation from charged particles at relativistic speeds that are forced to travel along curved paths by external magnetic fields. In the scope of this work only modern 3rd generation synchrotron radiation sources and x-ray free-electron lasers (XFELs) have to be considered. A 3rd generation synchrotron source describes a storage ring, dedicated to produce synchrotron radiation, with special insertion devices and long straight sections, optimized for high brilliance. First of its kind

is the European Synchrotron Radiation Facility (ESRF) [BDR95]. XFELs differ vastly from previous sources. Here, linear accelerators and extremely long undulator segments are used to create a lasing medium [Mad71]. In all of these applications the quality of the electron beam within the storage ring or the linear accelerator plays a crucial role for the feasibility of certain techniques and ultimately for the quality of the x-ray source. Hence, a short introduction to emittance is given first. Later, a short review of both 3rd and 4th generation sources will be given. Important beam parameters and resulting demands on x-ray optics are discussed thereafter.

3.1 Emittance

In general emittance can be defined for both the electron and the x-ray beam. The lower limit of the latter is simply given by the convolution of the electron beam emittance and the emittance of the x-ray beam produced by a single electron passing through the source. The electron beam emittance ϵ_e is determined by the product of electron bunch size σ and divergence σ' in a given transverse direction. The x-ray beam emittance ϵ_ph is calculated in the same way from the x-ray source size Σ and divergence Σ'. For circulating electrons in a storage ring the emittance is a constant due to *Liouville's theorem*. This can be visualized by an ellipse with constant area A in the phase-space representation shown in Figure 3.1. The general equation of an ellipse in the x-x'-plane is given by [Wil96]

$$\eta x^2 + 2\alpha x x' + \beta x'^2 = \epsilon = \frac{A}{\pi} \,. \tag{3.2}$$

With the definition $\eta \coloneqq (1+\alpha^2)/\beta$ the ellipse is uniquely defined by the parameters α, β, and ϵ. As an electron circulates in the storage ring the shape and position of the ellipse may change according to the amplitude function β, but the area $A = \pi\epsilon$ stays constant. However, there are many electrons in the bunch, moving with various amplitudes that correspond to different ellipses in phase-space. The average emittance can be defined by using the equilibrium distribution of particles described by a Gaussian distribution. We can now assign a certain emittance at one standard deviation σ with $\sigma = \sqrt{\epsilon_\sigma \beta}$. The emittance of the entire beam is then given with $\epsilon_\mathrm{e} \coloneqq \epsilon_\sigma = \sigma^2/\beta = \sigma\sigma'$ using $\sigma' \coloneqq \sigma/\beta = \sqrt{\epsilon_\sigma/\beta}$. Thus, the achievable x-ray source brilliance greatly depends on the electron bunch quality (cf. Equation (3.1)). The term diffraction limited source is used if the emittance from the electron beam is smaller than the x-ray beam emittance of a single electron passing through the source, e. g. an undulator. As this x-ray beam emittance scales with λ a diffraction limited storage ring is more challenging to realize for higher photon energies.

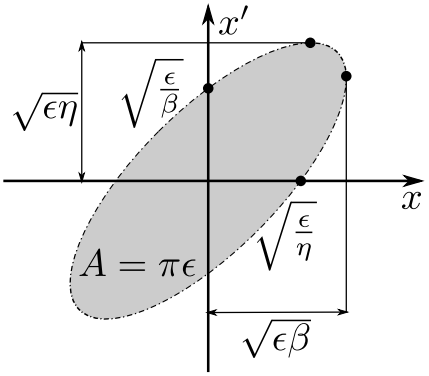

Figure 3.1: Phase-space representation of emittance for a single particle. The abscissa denotes the transverse position of the particle and the ordinate its divergence. For any position along the orbit of a synchrotron storage ring $\epsilon = \mathrm{constant}$ (adapted from [Wil96]).

3.2 Storage Rings For High Brilliance

In order to understand the emitted radiation from high-brilliance sources we first have to consider the principles of synchrotron radiation. The charged particle, here an electron, is traveling on a curved path due to the *Lorentz force* applied by external magnetic fields. As already discussed in Section 2.2.1 an accelerated electron emits dipole radiation. Here, the electron is not at rest, but moving at relativistic speeds. The energy E_e of an electron is given by

$$E_e = \frac{m_e c^2}{\sqrt{1-(v/c)^2}} \,.$$

For further discussions it is convenient to describe E_e in units of its rest mass energy with $\gamma = E_e/(m_e c^2)$. Nowadays storage rings have electron energies of several GeV, thus $\gamma \approx 10\,000$. The characteristic dipole radiation in the reference frame of the electron is therefore considerably changed after the Lorentz-transformation into the laboratory frame (cf. Figure 3.2). The opening angle of the tightly

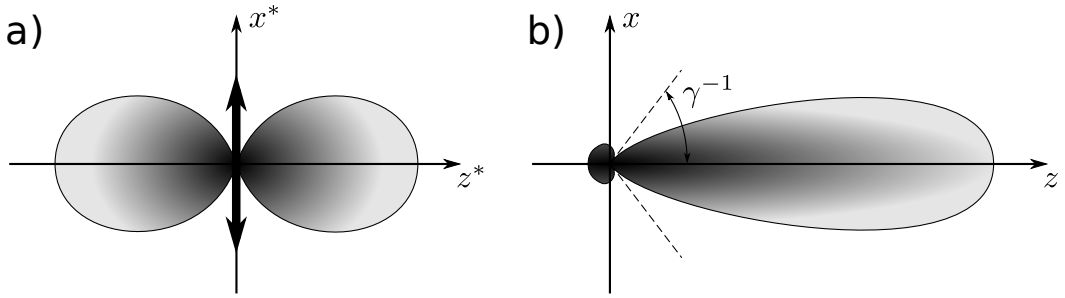

Figure 3.2: Schematic of dipole radiation in the reference frame of the electron (a) and in the laboratory frame (b). (adapted from [AM11])

collimated cone of radiation is given by γ^{-1}, which is roughly $85\,\mu\mathrm{rad}$ for a $6\,\mathrm{GeV}$ storage ring like PETRA III [Bal+04]. While even this collimated radiation cone is setting synchrotron sources apart of x-ray tubes, *insertion devices* have been developed to overlap these radiation cones and enhance brilliance even further. These insertion devices evolved from wigglers to undulators, where radiation cones not only simply overlap, but may also constructively interfere with each other. The basic principle behind these devices is a periodic lattice of alternating magnetic dipolar fields created by an array of magnets that forces the electron on a sinusoidal path while passing through the insertion device (cf. Figure 3.3 left side). Hence, the electrons are continuously accelerated. Characteristic properties of these devices are the spatial period of the undulating magnetic field λ_u, the number of periods N, and the deflection parameter

$$K = \frac{e}{2\pi m_e c} \lambda_u B_0 \tag{3.3}$$

with the magnetic field amplitude B_0, describing the maximum angle of electron deflection in units of γ^{-1}. The classification wiggler is made if the deflection angle of the electrons is larger than the opening angle of the collimated radiation cone given with γ^{-1}, thus $K \gg 1$. For undulators this is decreased, so that the deflection is within the radiation cone, meaning $K \lessapprox 1$, giving the emitted radiation a chance to

constructively interfere. It is this interference that leads to the undulator equation [FM10; AM11]

$$\lambda_n(\theta) = \frac{\lambda_u}{2n\gamma^2}\left(1 + \frac{K^2}{2} + \gamma^2\theta^2\right) = \lambda_n(0)\left[1 + \frac{\gamma^2\theta^2}{1 + K^2/2}\right] \equiv \lambda_n(0)\left[1 + \epsilon_\theta\right] \tag{3.4}$$

which describes the radiation harmonic $\lambda_n(\theta)$ of order n, that is emitted under the angle θ with respect to the optical axis. The fundamental wavelength emitted on axis is $\lambda_1(\theta = 0)$. Radiation is emitted in sharp wavelengths λ_n due to the interference condition. Only field amplitudes that constructively interfere with each other after the electron has moved one undulator period will contribute significantly to the spectrum, as depicted in the right side of Figure 3.3.

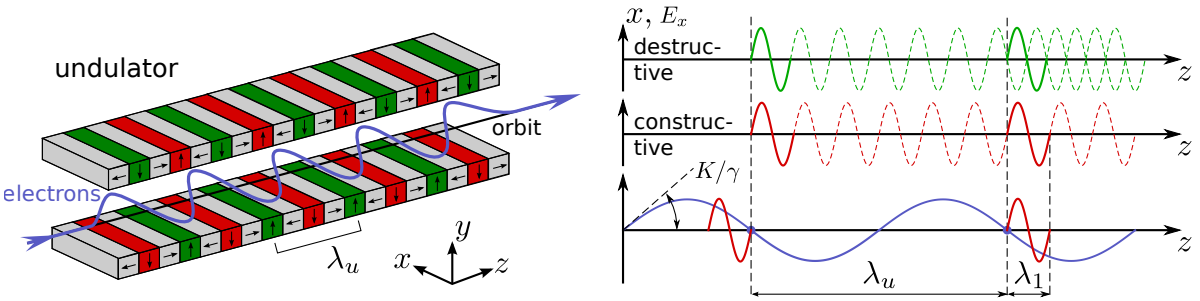

Figure 3.3: Relativistic electrons passing an undulator are forced on a sinusoidal path due to the alternating magnetic fields (left). Only sharp wavelengths that fulfill the interference condition will contribute significantly to the emitted spectrum (top right). While the electron has passed one undulator period λ_u the emitted radiation has overtaken the electron by one fundamental wavelength λ_1 (bottom right). (adapted from [HK07; MT10])

The angular term is simply given due to changing interference conditions off-axis, leading to a relative wavelength offset ϵ_θ. The bandwidth of any given harmonic scales inversely with the number of undulator periods N. Again, simple geometric considerations and the condition that radiation emitted at the beginning of the undulator should interfere constructively with radiation emitted at the end gives [FM10]

$$\frac{\Delta\lambda}{\lambda_n} = \frac{1}{nN} \,. \tag{3.5}$$

This bandwidth approximation directly leads to an additional collimation of the emitted radiation cone compared to the natural opening angle γ^{-1}. Comparing Equation (3.4) to Equation (3.5) suggests that the non-zero bandwidth can be related to a detuning of the wavelength by ϵ under a certain observation angle θ. Therefore, we can find the FWHM of the opening angle θ with [AM11]

$$\epsilon_\theta = \frac{\gamma^2\theta^2_{\mathrm{FWHM}}}{1 + K^2/2} \approx \frac{1}{nN} \qquad \longrightarrow \qquad \theta_{\mathrm{FWHM}} \approx \frac{1}{\gamma}\sqrt{\frac{1 + K^2/2}{nN}} \,. \tag{3.6}$$

This is a substantial reduction in angular divergence of undulator radiation, independent of the azimuthal angle relative to the undulator axis, and one of the reasons for the extremely high brilliance of these sources. Due to the fulfilled interference condition between the N undulator periods, the peak flux on-axis scales with N^2, which reduces to N when averaging over the cone angles, skaling with $N^{-1/2}$.

Let us now consider each individual electron j within the bunch of N_e electrons. The total emitted power

P of these electrons in an undulator is given by [MT10]

$$P \propto \left| \sum_{j=1}^{N_e} \psi_j e^{\mathrm{i}\phi_j} \right|^2 = \sum_{j=1}^{N_e} \psi_j^2 + \left| \sum_{\substack{j=1 \\ j \neq k}}^{N_e} \sum_{k=1}^{N_e} \psi_j \psi_k e^{\mathrm{i}(\phi_j - \phi_k)} \right|^2 \tag{3.7}$$

with ϕ_j as the phases of the emitted fields ψ_j of the $N_e \gg 1$ electrons within the bunch. If the system is uncorrelated, which is the case for chaotic electron bunches, the second sum of $\sim N^2$ terms tends to destructively interfere. In this case the emitted power is the sum of the N_e individual scattering electrons. To harness the potentially much larger coherent term, the phases of the electrons in the bunch have to be correlated, that is $\phi_j \approx \phi_k$ for all electrons. This correlation is realized by the collective interaction of all electrons in the bunch with the undulator radiation fields, known as a free-electron laser (FEL) and described briefly in the next section.

3.3 X-Ray Free-Electron Lasers

A theoretical description of an FEL with small gain effects and the potential to create coherent x-ray radiation was made as early as 1971 by Madey [Mad71]. Shortly thereafter the first FEL could successfully demonstrate amplification and lasing in the infrared regime [Dea+77]. While this FEL was operating in a low-gain regime using mirrors to create an oscillator, current x-ray emitting FELs (XFELs) operate in a high-gain mode [SS80]. The radiation power increases exponentially while the electron bunch and the radiation field co-propagate in the undulator. It allows the operation as a single-pass amplifier and eliminates the need for mirrors to form an oscillator cavity. This development was a crucial step towards XFELs, since the reflection of x-rays is extremely weak due to $n \approx 1$. While electrons are propagating through the undulator they emit synchrotron radiation. Since electrons are slower than light the emitted radiation field passes the electrons. An electron interacting with a resonant radiation field can have a slow exchange of energy with the field over many undulator periods [MT10]. Depending on their position with respect to the resonant field half of the electrons may gain energy while the other half loses energy. This perturbation causes the electrons to bunch at the radiation wavelength, known as microbunching, allowing a coherent interaction between radiated field and electrons (cf. Figure 3.4 right side). Thus, the emitted radiation scales with $\sim N_e^2$ (cf. Equation (3.7)).

The fundamental scaling parameter of an FEL is the *Pierce parameter* ρ [BPN84] and gives a measure of the coupling strength between electrons and radiation field. In the x-ray regime $10^{-4} \leq \rho \leq 10^{-3}$. With the help of this parameter a lot of quantities of the XFEL can be described. One of them is the spectral bandwidth of the emitted x-ray beam $\Delta E_{\mathrm{ph}}/E_{\mathrm{ph}} \approx \rho$. The quality of the electron beam greatly influences the Pierce parameter. For successful FEL operation the energy spread of the electron bunch should be $< \rho$. Another important requirement, as noted earlier, is the electron beam emittance ϵ_e. As $\rho \propto \epsilon_e^{-1/3}$ [BDM92] a sufficiently small beam emittance is necessary in order to achieve adequate coupling. The condition on the emittance is given with $\epsilon_e \leq \lambda_1/(4\pi)$ [MT10], which is the same as for diffraction limited emission of spontaneous undulator radiation [Kim86a]. The Pierce parameter is also a measure of the undulator periods N_g required in order to increase the radiated power by a factor $2e$ given with $N_g = (4\pi\rho)^{-1}$. This leads to hundreds of periods in the x-ray regime. Thus, the undulator sections

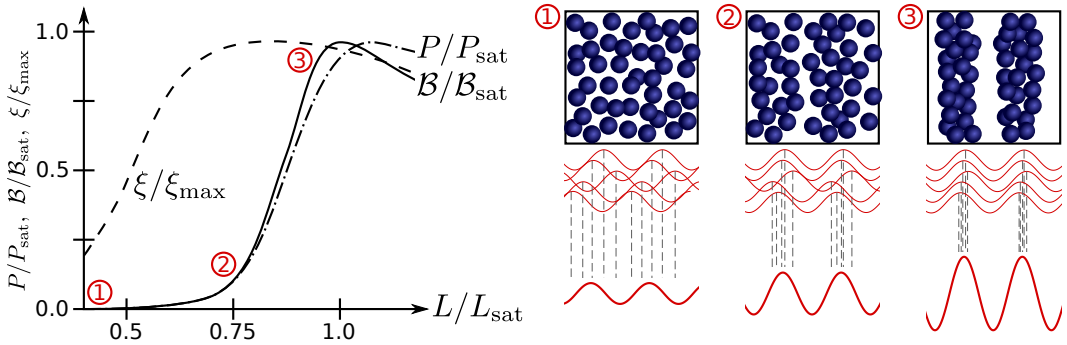

Figure 3.4: Evolution of main SASE FEL parameters along the undulator. Brilliance (solid line) and radiation power (dash-dotted line) are normalized to saturation values. The transverse coherence ξ (dashed line) is normalized to its maximum value. At the beginning of the undulator (label 1) electrons are uncorrelated to the radiation field and amplitudes do not overlap. During propagation electron phases begin to align (label 2) due to a collective interaction with the radiation field. At the saturation point (label 3) electrons are strongly bunched and emit coherently, increasing radiation power drastically. (adapted from [SSY10; MT10])

at XFELs are typically very long ($\sim 100\,\mathrm{m}$) compared to insertion devices at synchrotron sources ($2\,\mathrm{m}$ to $5\,\mathrm{m}$). For lasing to occur the electron beam must travel straight through the long undulator. Transverse drifts of $10\,\%$ to $20\,\%$ can significantly disrupt the FEL interaction [MT10]. This requires an alignment $< 5\,\mu\mathrm{m}$ over the whole undulator length. In addition fluctuations in the deflection parameter K of the undulator have to be small enough, so that no dephasing of electrons with respect to the radiation field occurs. The gain process in the undulator saturates if the density modulation in the electron bunch correlates with the fundamental radiation wavelength and maximum bunching is achieved (cf. Figure 3.4 label 3). The total emitted radiation power at saturation P_{sat} scales with $P_{\mathrm{sat}} \propto P_b\rho$, where P_b is the kinetic energy of the electron bunch [Kim86b].

All these challenges make the realization of an hard x-ray FEL extremely difficult. The first XFEL (FLASH at DESY in Hamburg) started 2005 and was operating at a soft x-ray wavelength of $32\,\mathrm{nm}$ [Fel10]. It originated from the TESLA Test Facility were the first proof-of-principle of lasing at saturation was demonstrated in 2001 [Sch10]. The next landmark for FELs was the Linac Coherent Light Source (LCLS) in Stanford, demonstrating a successful operation at a hard x-ray wavelength of $1.5\,\text{Å}$ in 2009 [Emm+10]. Previous discussions were based on the assumption of an electron beam of infinite duration and uniform density. In real-world applications like the LCLS small electron pulses with $\sim 1\,\mathrm{nC}$ of charge and durations of several tens of fs are injected into the undulator. Here, the emitted radiation propagates or slips through the electron bunch at one fundamental wavelength λ_1 per undulator period. Since the system starts from noise, several regions within the electron bunch may evolve with no phase correlation, known as self-amplified spontaneous emission (SASE) [BPN84]. These regions are characterized by the cooperation length l_c which is a measure for the radiation field slippage over one gain length and is given by $l_c = \lambda_1/(4\pi\rho) = \lambda_1 N_g$ [BMP89]. For an electron bunch with length l_b there will be approximately $l_b/(2\pi l_c)$ phase uncorrelated regions, typically over 100 for an XFEL. Each of these regions emits highly lateral coherent FEL radiation. But the longitudinal coherence is greatly reduced and several spikes develop in the spectral distribution. While each spike has a narrow bandwidth $\Delta E_{\mathrm{ph}}/E_{\mathrm{ph}} \approx \rho$, the total SASE bandwidth may be in the order of $0.2\,\%$ to $0.5\,\%$ [Emm+10]. This imposes some difficulties when working with refractive lenses, described in more detail in Section 4.3.4.

More advanced radiation schemes at XFELs have evolved over the time and also a more compact XFEL is in operation at Spring-8 in Japan [Ish+12]. One of this new possible operation modes is the seeded XFEL. The idea is to seed the initial FEL interaction with a high temporal coherence source, so that the seed power is dominating the initial SASE power and the temporal coherence is maintained during amplification. While seeding from an external source was demonstrated in the ultraviolet regime [Lam+08], insufficient seed powers at shorter wavelengths may limit this approach to the $\sim 1\,\mathrm{nm}$ region [MT10]. Recently a self-seeding scheme was demonstrated for the first time at LCLS that spectrally filters the SASE radiation at an early stage by using a diamond crystal in forward Bragg diffraction [Ama+12]. The self-generated monochromatized beam is then used to seed subsequent SASE radiation. Another interesting opportunity is the two-color operation were two separate pulses with different photon energy and time delay are produced. Various realizations exist today focusing on different aspects such as large energy spread [Har+13], narrow bandwidth [Lut+14], and high intensity [Mar+15].

3.4 Important X-Ray Beam Properties

The initially discussed brilliance $\mathcal{B}$ gives a single value to describe the performance of any given x-ray source. It combines important properties like source size Σ, source divergence Σ', pulse duration τ, and energy bandwidth $\Delta E/E$. While being a good figure of merit to compare different x-ray sources, other parameters are often of higher interest at the experimental station. These include the time structure and pulse duration of the incoming x rays and their degree of longitudinal and transverse coherence. In the following sections a short overview of these properties and typical values for undulator sources at storage rings and XFELs is given.

3.4.1 Time Structure and Pulse Duration

Depending on the experiment the time structure and individual pulse length of the x-ray beam is of great interest. While at storage ring sources the time structure depends on the filling mode of the electron bunches within the ring and is equal for all beamlines at a given time, XFELs provide the ability to select pulse duration and time structure for each experiment and even single measurements individually. Storage rings are filled with a certain number of bunches, usually spaced equidistantly within the ring. Sometimes also special filling modes, where for example only one quarter of the storage ring is occupied with electron bunches, are used. A typical time resolved operation mode at PETRA III of DESY is 40 bunch filling with $100\,\mathrm{mA}$ current at $E_e = 6\,\mathrm{GeV}$. With a storage ring circumference of $2304\,\mathrm{m}$ each bunch has $\sim 20\,\mathrm{nC}$ charge, which is significantly higher than $1\,\mathrm{nC}$ at XFELs. These high charges elongate the electron bunch and cause relatively long pulse durations in the order of $\sim 100\,\mathrm{ps}$ with a separation of $\sim 200\,\mathrm{ns}$. Thus the achievable time resolution is limited and individual pulses are very weak compared to XFELs due to the incoherent electron radiation. Nevertheless time-resolved structural studies using Laue diffraction or Wide Angle X-ray Scattering (WAXS) on proteins are performed routinely at these sources [NM12].

To study even faster processes of transient phenomena in physical, chemical and biological systems shorter pulse durations with sufficient intensity are necessary and can be delivered by XFELs. The

fundamental limitation to the pulse duration is given by the spectral width $\Delta\omega$ with

$$\Delta\omega\,\tau \leq 2\pi\ .$$

For a coherent Gaussian pulse that is *unmodulated*, *bandwidth-limited*, or *transform-limited* (all used interchangeably in literature) $\Delta\omega\,\tau = 2\pi$. To obtain a pulse length of $\tau = 1\,\mathrm{fs}$ a spectral bandwidth of at least $\hbar\Delta\omega \geq 4.14\,\mathrm{eV}$ is required. Since $\hbar\Delta\omega$ is much smaller than the photon energy in the x-ray regime, the pulse will be undistorted and similar to a long pulse [Hau11]. While these pulse durations are possible in theory, even low-charged electron bunches at XFELs have duration of several femtoseconds. Since SASE starts from random noise many coherent modes develop in the time domain over the electron bunch length [Li+05] as already discussed in Section 3.3. Thus, generated pulses at SASE XFELs are far from being unmodulated. Various schemes are proposed to reduce the pulse duration in the attosecond regime by reducing bunch charges to as low as $1\,\mathrm{pC}$ and manipulating electrons in phase-space by external laser fields, so that only a small part of the bunch will emit radiation [Hem+14]. While the proposed technologies are currently emerging, typical pulse durations available to date at XFEL sources can be as low as $10\,\mathrm{fs}$.

3.4.2 Longitudinal Coherence

As seen in the previous section the pulse duration is directly connected to the spectral bandwidth of the pulse. Here, we want to focus on the latter and concisely discus longitudinal coherence. While coherence can be discussed in the form of probability amplitudes in quantum mechanics, we want to focus on a phenomenological approach in terms of classical wave mechanics. The term coherence in general describes the stability of the electromagnetic field and is a measure of the correlation of the field in space and time. For example, the field amplitudes of a perfectly monochromatic wave that exists throughout space are known everywhere and for all times from a single measurement alone. The wave is fully coherent.

Longitudinal coherence refers to the time component. However, it is convenient to measure coherence in terms of a length in order to provide a meaningful quantity for typical experimental scenarios. In general, we are interested in a coherence volume that, ideally, should be larger than the illuminated sample volume in order to guarantee interference of scattered light from within that sample.

Consider two plane waves A and B that differ in energy by ΔE and thus $\lambda_B = \lambda_A - \Delta\lambda$, propagating in the same direction. If the waves are in phase at a position P, how far do they have to propagate before they are out of phase. This distance defines the longitudinal coherence length ξ_l. If we propagate further the waves will be in phase again after the distance $2\xi_\mathrm{l}$. Let us assume $2\xi_\mathrm{l} = N\lambda_A$, or equivalently for wave B with the shorter wavelength λ_B we can write $2\xi_\mathrm{l} = (N+1)(\lambda_A - \Delta\lambda)$. Thus, we can write

$$2\xi_\mathrm{l} = N\lambda = (N+1)(\lambda - \Delta\lambda) \qquad \longrightarrow \qquad \xi_\mathrm{l} = \frac{\lambda^2}{2\Delta\lambda} = \frac{\lambda}{2\Delta\lambda/\lambda}\ . \tag{3.8}$$

The coherence length is only dependent on the monochromaticity or bandwidth of the x-ray pulse. For a SASE beam at $E_\mathrm{ph} = 8\,\mathrm{keV}$ and $\Delta E/E \approx 2\times10^{-3}$ we have $\xi_\mathrm{l} \approx 40\,\mathrm{nm}$. If a Si-111 crystal monochromator ($\Delta E/E = 1.4\times10^{-4}$) is used, equivalently to a typical storage ring situation, we get $\xi_\mathrm{l} \approx 550\,\mathrm{nm}$.

3.4.3 Transverse Coherence

Transverse coherence in this context relates to the correlation of electromagnetic fields originating from different points of a chaotic source with finite extent in a distant plane of observation. Two waves with identical wavelength that originate from different source points will be tilted against each other by an angle $\Delta\theta$ when observed at a distance L (cf. Figure 3.5). Let their wavefronts coincide in point P.

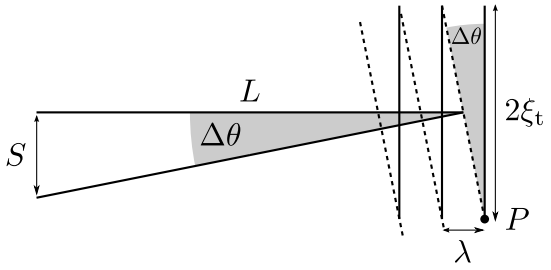

Figure 3.5: Correlation between two monochromatic plane waves tilted to on another by $\Delta\theta$. (adapted from [AM11])

The transverse distance ξ_t from P at which both waves are out of phase is called the lateral coherence length. After a distance $2\xi_\mathrm{t}$ they will be in phase again. From Figure 3.5 is obvious that $\lambda = 2\xi_\mathrm{t}\Delta\theta$ and $\Delta\theta = S/L$. With these relations we can derive the transverse coherence length at distance L from the source size S via

$$\xi_\mathrm{t} = \frac{\lambda L}{2S} \,. \tag{3.9}$$

We see that lateral coherence can be increased by a smaller source size or by simply going further away from the source. Since the former is not trivial due to the electron bunch emittance most experiments at storage ring facilities are placed over $50\,\mathrm{m}$ away from the source. Note that this coherence can be greatly influenced by other optical elements along the beam path that may create a secondary source like monochromators or prefocusing lenses. At XFELs the coherence length is much larger than the lateral extent of the radiation cone. However, the coherence is not perfect due to the overlap of different radiation modes [SSY10; Var+11].

A more sophisticated treatment of coherence by means of the mutual coherence function and the theorem of van Cittert-Zernike can be found elsewhere [BW80; Goo00]. When using these formalisms to calculate the transverse coherence length of a chaotic Gaussian source at a distance L one obtains [Pat10]

$$\xi_{\mathrm{t},\{\mathrm{h,v}\}} = \frac{4\ln 2}{\pi}\frac{\lambda L}{S_{\{\mathrm{h,v}\}}} \,. \tag{3.10}$$

Depending on the FWHM extent of the Gaussian source $S_{\{\mathrm{h,v}\}}$ in horizontal or vertical direction we obtain a FWHM coherence length $\xi_{\mathrm{t},\{\mathrm{h,v}\}}$, respectively. When comparing this result to Equation (3.9) one realizes that they only differ by a coefficient. In literature the degree of spatial coherence is often used, referring to the fringe visibility of an interference pattern. In Young's double-slit experiment, for example, the degree of coherence can also be related to the transverse distance between the two slits and a certain fringe visibility that decreases with larger transverse slit distances.

4 Refractive X-Ray Optics

Ever since the discovery of x rays in 1895 one was searching for ways to build an x-ray microscope similar to the ones available for visible light. The benefits of such an x-ray microscope, considering the unique properties of x-ray radiation, would be enormous. The challenge to overcome is the extremely small decrement δ of the refractive index n. For most materials in the x-ray regime δ is in the order of 10^{-5} to 10^{-7} and positive, leading to $n \lesssim 1$ (cf. Section 2.2.2). In contrast to this, for visible light n is much larger than unity. Fused silica, for example, has a refractive index of ≈ 1.5 in the visible light regime. Additionally, the absorption of x rays in appropriate lens materials is considerably stronger than in comparable materials used for visible light. This implies several difficulties when adapting refractive lenses or mirrors into the x-ray regime. Due to $n \lesssim 1$ refractive lenses can only deflect the x-ray beam by a very small amount and must have a concave shape in order to focus x rays, contrary to convex lenses in the visible light regime, where $n > 1$. This leads to the need of several lenses with small curvatures, which, on the other hand, enforces a small aperture and increased absorption for the lens stack. With that in mind scientists in the early twentieth century kept their focus on x-ray optics based on reflection and diffraction. While reflection is also very weak for x rays, the effect of total external reflection allows one to use mirrors in order to focus light. Despite the low critical angle of $\theta_c = \sqrt{2\delta} < 1°$ (cf. Section 2.2.5), several optics like Kirkpatrick-Beaz mirrors [KB48] or Wolter mirrors [Wol52] have been developed. Also capillaries [HTB94] and waveguides [Pfe+02] emerged. Another method based on Bragg reflection on crystal lattices or multilayer stacks has led to the invention of bent crystals [Sch+98] and multilayer mirrors [UTF86]. Another method to focus light over a large range of the electromagnetic spectrum are Fresnel zone plates based on Fresnel diffraction theory [Lai+92; Sch06; Pfe+06]. Over the past years other flavors like Multilayer Laue Lenses have evolved [Mas+04; Yan+11; Bra+13; Mor+15] that make use of thin film techniques to create one-dimensional diffraction gratings.

At the end of the 20th century scientist discussed again the possibility of refractive x-ray optics. While Michette et al. [Mic91] still believed a refractive lens is not possible, the first lens prototype was successfully tested at ESRF in 1996 [Sni+96]. Later on the design and fabrication where further refined and compound refractive x-ray lenses (CRLs) [Len+99; Len+02] and nanofocusing refractive x-ray lenses (NFLs) [Sch+03] have been fabricated and are nowadays widely used at hard x-ray radiation sources [Hop+13; Dzh+14; Sch+15]. An introduction to these concave shaped lenses is given in the next section. Challenges in the microfabrication of x-ray optically favorable materials led to an advancement of the concave lens shape into a lamella lens, the refractive lamellar lens (RLL) [Sei+14a], discussed later on in section 4.2.

Moreover, common properties of CRLs, NFLs and RLLs are given at the end of this chapter in section 4.3. With this knowledge several favorable lens materials are compared in Section 4.4. Limitations, current possibilities, and future developments will be briefly highlighted.

4.1 Parabolic X-Ray Lenses

Today's parabolic compound refractive x-ray lenses (CRLs) have first been introduced by Lengeler et al. in 1998 [Len+98]. They consist of several lenses stacked behind one another, each with a rotationally symmetric parabolic profile and a bi-concave shape. Due to $n < 1$ in the x-ray regime, a focusing lens is concave rather than convex for visible light. The stacking of many lenses is compulsory since the refraction inside the lens material is extremely weak. To illustrate this, let us consider a thin spherical lens with a common radius $R = 0.2\,\mathrm{m}$. According to the lensmaker's equation [Hec02] the focal length f for a thin lens is given by $f = R/(2\delta)$. A conventional fused silica lens ($|\delta| \approx 0.5$ for visible light) would focus the light in a distance of $f = 0.2\,\mathrm{m}$ if the shape is convex (since $n > 1$ for visible light). Assuming a reasonable but arbitrary $\delta = 0.5 \times 10^{-6}$ for the same lens, but with a concave shape in the x-ray regime, the focal distance f would be $200\,\mathrm{km}$. One can imagine that such a lens is not useful and that the deflection of x rays is very hard to detect. Indeed that was the observation of Röntgen in 1895 [Rön95]. He correctly noted that his measurement accuracy may not have been good enough to detect the deflection. Scientists interpreted this the wrong way and believed x rays can not be refracted. Two obvious solutions come to mind when coping with this problem: use more lenses and decrease the radius of curvature. That is what Snigirev et al. did in 1996 when they demonstrated viable x ray focusing with refractive lenses made of small holes drilled in aluminum [Sni+96].

Unfortunately, spherical lenses are not well suited for x ray focusing as they introduce aberrations. This is also known for visible light, but the effects are considerably smaller. When looking at a visible light lens, the radius of curvature can usually be significantly larger than the lens aperture. This means only a small part of the sphere is actually illuminated. But with the weak refraction of x rays the lens curvature has to be extremely small. Actually, the radius of curvature is smaller than the lens aperture, which means the whole sphere of an x-ray lens is being illuminated. To calculate the correct lens shape we evaluate the refraction of x rays on a single lens surface $s(r)$ (cf. Figure 4.1(a)). The refraction of an x-ray beam

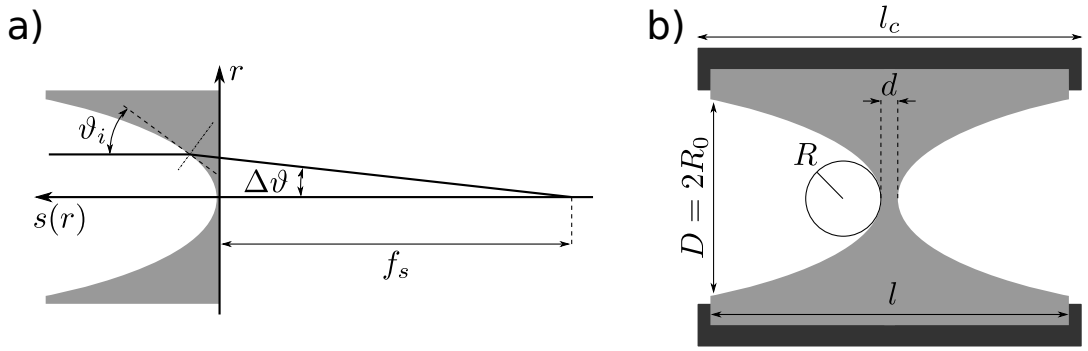

Figure 4.1: Shape of refractive x-ray lenses. (a) Refraction at a concave lens. The angle between the incident beam and the lens surface is given by ϑ_i. (b) Geometry of a biconcave parabolic lens held in a casing of width l_c.

at distance r from the optical axis can be described with Snell's law by $\cos\vartheta_i = (1-\delta)\cos(\vartheta_i - \Delta\vartheta)$. In paraxial approximation, which is a good assumption considering the weak refraction and small apertures of an x-ray lens, one derives $\Delta\vartheta = \delta\cot\vartheta_i = \delta(ds/dr)$. For a thin lens, where the focal length f_s is significantly larger than the lens thickness, $\Delta\vartheta$ can be calculated by r/f_s. After integration the shape is

given by

$$\frac{r}{f_s} = \delta \frac{ds}{dr} \qquad \longrightarrow \qquad s(r) = \frac{r^2}{2 f_s \delta} + c \,, \tag{4.1}$$

which translates to a parabolic lens shape. It is convenient to express the curvature at the lens apex with $d^2 s(r)/dr^2 = 1/(f_s \delta) \equiv 1/R$, where R is the radius of curvature as depicted in Figure 4.1(b). The geometrical aperture $D = 2R_0$ is then given by the thickness l of the lens and the gap d between the two surfaces via $D = 2\sqrt{(l-d)R}$. The focal length f of such a biconcave lens with two parabolic surfaces is half the focal length of a single surface f_s, hence

$$f = \frac{R}{2\delta} \,. \tag{4.2}$$

Further properties of refractive x-ray lenses will be discussed in Section 4.3. The mentioned CRLs feature this parabolic profile in a rotational symmetry like conventional visible light lenses. They are manufactured by embossing metal foils. This mechanical process, however, is the limiting factor for practicable lens curvatures. Today's smallest available curvature is $R = 50\,\mu\mathrm{m}$. The fact that each lens is produced individually can be seen as an advantage, since one can configure the lens stack to the specific requirements. Though the downside is the casing required for alignment and stabilization of the metal foil. This enforces gaps between lenses since the casing width l_c is larger than the lens length l, effectively reducing refractive power per unit length of the lens stack. As will be shown in Section 4.3.1 the minimal attainable focal distance of a lens is given by $f_{\min} = \sqrt{R l_c/(2\delta)}$, which directly translates to the achievable lateral focal spot size.

To overcome this mechanical machining limitation a new type of lens was developed using microfabrication techniques for silicon wafers, the nanofocusing refractive lens (NFL) [Sch+03; Sch+05]. An NFL consists of several tiny micro lenses etched into a silicon substrate with lithographic techniques (cf. Figure 4.2). Due to this process the lenses are not rotationally but cylindrically symmetric and can only focus x rays in one dimension. The advantage, however, is the ability to structure lenses with curvatures as small as a few micro meters and the direct stacking behind each other so that $l_c = l$.

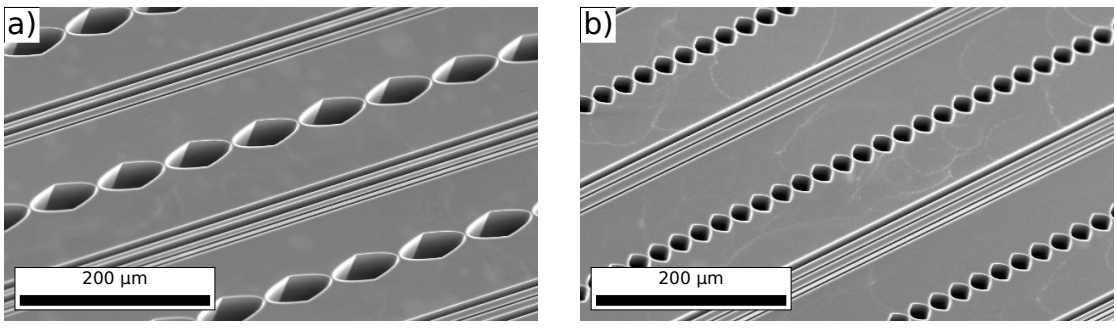

Figure 4.2: SEM image of NFLs produced in 2009. (a) $R = 4.2\,\mu\mathrm{m}$ with high aspect ratio. (b) $R = 7.8\,\mu\mathrm{m}$ with small aspect ratio.

4.2 Lamellar X-Ray Lenses

While NFLs are a great success for focusing hard x rays at synchrotron radiation sources [Sch+05; Sch+10a], the lens material is limited to silicon. This restriction is mainly imposed by available mi-

crostructuring processes that allow high aspect ratios of the order of 1:10.

As we will show later on in Section 4.4 silicon is a well suited lens material, but its high absorption reduces lens apertures considerably for reasonable curvatures. This is caused by the relatively high atomic number of $Z = 14$ compared to more favorable materials and limits the possible numerical aperture and thus also focal spot size and gain. Ideally, a material with low Z and highest density ρ is best. Beryllium is a well suited material, especially for lower photon energies below $15\,\mathrm{keV}$ (cf. Figure 4.7). For harder x rays diamond is the most desired material for refractive x-ray optics when minimal focal spot sizes are required.

In the past efforts were made to etch lenses into a diamond substrate, since established etching processes exist. However, they are only used for very shallow etch depths. The required etch depth in order to achieve high aspect ratios could not be realized [Nöh+03; Boy09]. The etch process is severely disturbed and needles are formed at the bottom of the etched substrate. Currently, a new technique is evolving that uses high-intensity short-pulse lasers in order to structure one- and two-dimension lenses out of diamond [Pol+15; Ter+15]. However, the process is still at an early stage and achieved curvatures are large.

When further looking for appropriate materials sapphire (Al_2O_3) is a very promising material as well. Unfortunately there exist no established etching methods. However, the deposition of thin films using the technique of atomic layer deposition (ALD) is well established. At first glance it seems contradictory to create a refractive lens, which has to have a parabolic refraction profile given by Equation (4.1), out of thin films with equal thickness and homogeneous material properties. The only way to create some kind of thickness change was by bending this thin film like a piece of paper to create a distinct projected thickness. The concept on how to "bend" this Al_2O_3 film in order to create a parabolic thickness profile in projection geometry is described in the following.

Shape Calculation

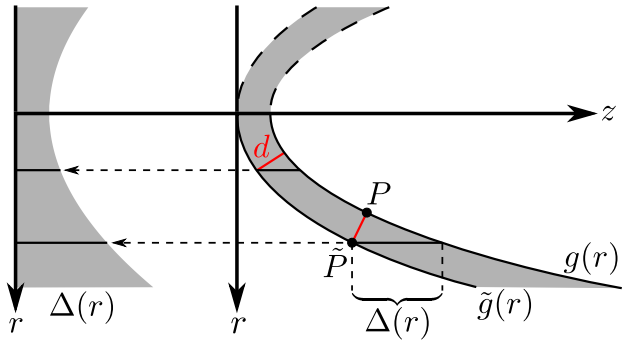

Figure 4.3: The parabolic thickness profile is generated in projection of a lamella of constant thickness d. The lamella shape is defined by the two functions $g(r)$ and $\tilde{g}(r)$ to yield a projected thickness $\Delta(r)$ that grows parabolic with r. (Reprinted with permission from [Sei+14a]. Copyright 2014, AIP Publishing LLC.)

The concept to calculate the shape is depicted in Figure 4.3. The refractive lamellar lens (RLL) consists of many thin lamellae with a constant thickness d. The projected thickness along the optical axis z, however, shall follow the parabolic lens profile as derived earlier in Equation (4.1):

$$\Delta(r) = \frac{r^2}{2R} + d\,. \tag{4.3}$$

To calculate the shape we will describe a single lamella by the two surfaces $g(r)$ and $\tilde{g}(r)$. The simple condition for a parabolic profile in projection is then

$$g(r) = \tilde{g}(r) + \Delta(r) \, . \tag{4.4}$$

To enforce a constant thickness we demand that the minimal distance between g and $\tilde{g}$ shall be d. On the optical axis we set $g'(0) = 0$ and hence $g(0) = d$. The shortest distance from any point $\tilde{P}(\tilde{r}|\tilde{g}(\tilde{r}))$ on $\tilde{g}$ to g is given by the orthogonal projection from $\tilde{P}$ onto g, marked by the point $P(r|g(r))$ and is given with $\tilde{P} = P + d \cdot n_g(r)$. This can be written as

$$\begin{pmatrix} \tilde{r} \\ \tilde{g}(\tilde{r}) \end{pmatrix} = \begin{pmatrix} r \\ g(r) \end{pmatrix} + \frac{d}{\sqrt{1 + g'^2(r)}} \begin{pmatrix} g'(r) \\ -1 \end{pmatrix} \, , \tag{4.5}$$

where we used the normal n_g on g given with

$$n_g(r) = \begin{pmatrix} g'(r) \\ -1 \end{pmatrix} \frac{1}{\sqrt{1 + g'^2(r)}} \, .$$

Note that we could have also used the projection from P onto $\tilde{g}$. To ensure that the solution is monotonically increasing we set $g' \geq 0$. From the first equation in Equation (4.5) we obtain

$$\tilde{r} = r + d \frac{g'(r)}{\sqrt{1 + g'^2(r)}} \, . \tag{4.6}$$

When we follow the initial condition $g(r) - \tilde{g}(r) = d$ (Equation (4.4)) and substitute Equation (4.6) in the second equation of Equation (4.5) we obtain the nonlinear differential equation

$$g\left(r + d\frac{g'(r)}{\sqrt{1 + g'^2(r)}}\right) - \Delta\left(r + d\frac{g'(r)}{\sqrt{1 + g'^2(r)}}\right) = g(r) - d\frac{1}{\sqrt{1 + g'^2(r)}} \, . \tag{4.7}$$

This equation can be solved if we consider $d \ll 1$ and linearize the first term on the left side of Equation (4.7), yielding

$$d\sqrt{1 + g'^2(r)} - \Delta\left(r + d\frac{g'(r)}{\sqrt{1 + g'^2(r)}}\right) = 0 \, . \tag{4.8}$$

With the given expression for $\Delta(r)$ from Equation (4.3) and by approximating $\sqrt{1 + g'^2} \approx 1 + g'^2/2$ and $g'/\sqrt{1 + g'^2} \approx g'$ if we consider $g' \ll 1$ we obtain

$$0 = d\left(1 + \frac{1}{2}g'^2\right) - \left(\frac{1}{2R}\left(r + dg'\right)^2 + d\right) \, . \tag{4.9}$$

This ordinary nonlinear differential equation can be solved by numerical methods. The implemented algorithm uses a 5th-order *Runge-Kutta* method as described in [Pre+07]. The presented mathematical solution was obtained with the help of Jens Seidel from the Faculty of Mathematics at Technische Universität Chemnitz.

The lamella shape could be calculated with minimal errors for the desired parabolic thickness profile. As an example the results for the lens parameters $R = 20\,\mu\mathrm{m}$ and $d = 2\,\mu\mathrm{m}$ are shown in Figure 4.4 up

to $R_0 = 25\,\mu\text{m}$. The lens surfaces $g(r)$ and $\tilde{g}(r)$ are depicted on the left side together with the obtained thickness in projection $\Delta(r)$. The thickness error $\epsilon(r)$ shown on the right side was calculated by fitting Equation (4.3) to the result. Errors are well below $1\,\text{nm}$ and much smaller than process inaccuracies during microfabrication.

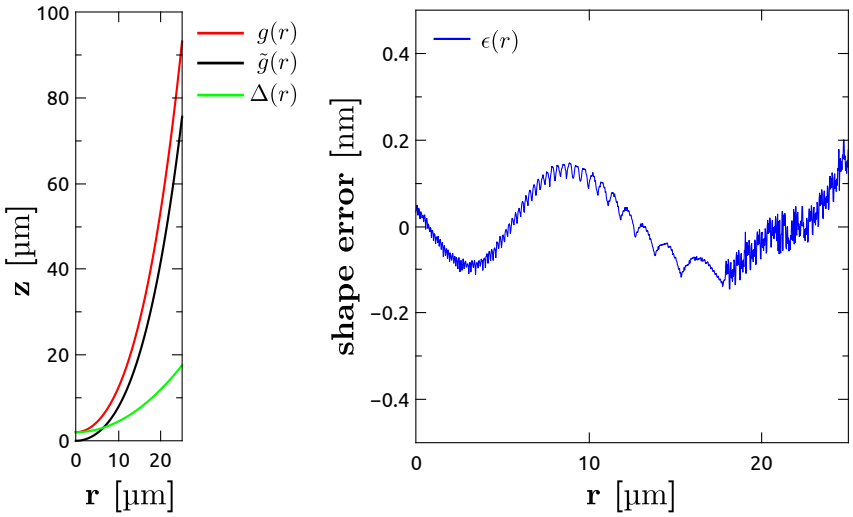

Figure 4.4: The result after solving the differential equation Equation (4.7) for the lens parameters $R = 20\,\mu\text{m}$ and $d = 2\,\mu\text{m}$ is shown on the left. The error of the projected thickness $\Delta(r)$ compared to a parabolic fit is depicted on the right side.

4.3 Basic Properties of Refractive X-Ray Lenses

While we have already discussed basic lens characteristics at the beginning of Section 4.1 we want to discuss more properties in order to assess suitable materials for x-ray optics more qualitatively and understand basic limitations. The theory from a thin lens will also be adapted to thick lenses, which is often the case when many lenses are stacked behind each other.

4.3.1 Focal Distance

We have already derived the focal distance for a single biconcave lens in Equation (4.2). However, this equation holds only in the limit of a thin lens, meaning the focal distance f is much larger than the single lens thickness l ($f \gg l$) as shown in Figure 4.1(b). We can adapt Equation (4.2) with ease to N stacked lenses with $(1/f_N) = \sum(1/f_i)$. If every lens in the stack has the same focal distance $f = f_i$, then

$$f_N = \frac{R}{2N\delta}\,. \tag{4.10}$$

Again, this formulation only holds if the whole lens stack with length $Nl_c \ll f_N$, which is typically not true for the lenses under consideration in this work. The stack length is greatly influenced by the casing width l_c of a single lens. Since we often want to achieve smallest spot sizes, focal distances need to be minimized, as we will see in Section 4.3.3.

In order to derive the focal distance of a thick lens one can imagine such a lens in the limit of infinite lenses $N \to \infty$ with constant lens stack length and refractive power. Under this assumption an off-axis

x-ray may oscillate within the lens stack if the length and refractive power are sufficient. The spatial oscillation frequency ω equals the refractive power per unit length and is given with

$$\omega = \sqrt{\frac{2\delta}{Rl_c}} \,. \tag{4.11}$$

Several properties of the lens can be derived from this approach. Two important positions along the optical axis are the focal plane position z_F and the principal plane position z_H, which is shifted against the center of the lens. Assuming the beginning of the lens stack at position $z = 0$ one can derive [Pat10]

$$z_H = L + \frac{\cot(\omega L)}{\omega} - \frac{1}{\omega \sin(\omega L)} \,, \tag{4.12}$$

$$z_F = L + \frac{\cot(\omega L)}{\omega} \,. \tag{4.13}$$

The focal length is defined as the distance between those two planes $f = z_F - z_H$ and hence

$$f = \frac{1}{\omega \sin(\omega L)} \,. \tag{4.14}$$

The minimal focal distance $f_{\min}$ can now be determined as the first intersection of the spatially oscillating x rays with the optical axis. The first intersection occurs at $\omega L = \pi/2$ and we can define a critical maximal lens length $L_{\max} = \pi/(2\omega)$. With this we can derive an expression for the shortest possible focal distance

$$f_{\min} = \frac{1}{\omega \sin(\omega L_{\max})} = \frac{1}{\omega} = \sqrt{f_s l_c} = \sqrt{\frac{Rl_c}{2\delta}} \,. \tag{4.15}$$

In order to achieve shortest focal lengths and smallest spot sizes one has to increase the refractive power per unit length. This means reducing Rl_c by smaller curvatures, shorter lenses, and by choosing a material with high refraction δ. Since δ/ρ is nearly constant over the x-ray spectrum, materials with highest densities are favorable. However, the spot size is not only determined by focal length, but also by the optics aperture. For visible light the aperture is limited by the lens geometry due to weak absorption. In the x-ray regime this is often not true. Absorption inside the lens can severely influence transmission and thus the effective aperture.

4.3.2 Transmission and Gain

Transmission or efficiency is one of the most crucial properties of any optics. The term efficiency is used for example in connection with Fresnel zone plates and mirror optics, describing diffraction and reflection efficiency, respectively. For refractive optics light is absorbed and the term transmission is more appropriate. Both terms describe the loss of photon flux. For refractive lenses the parabolic transmission profile and surface effects have to be considered. The transmission T_p is given by [Len+99]

$$T_p = \frac{1 - e^{-2a_p}}{2a_p} e^{-\mu N d} \qquad \text{with} \qquad a_p = \frac{\mu N R_0^2}{2R} + \frac{N\delta^2 k^2 \sigma^2 R_0^2}{R^2} \,. \tag{4.16}$$

While the fraction of the left equation relates to the parabolic transmission profile of the lenses, the exponential term $\exp(-\mu N d)$ describes a reduction due to an unavoidable material gap d at the apex of the parabolas. For CRLs made of Be this can be tens of μm per lens. For NFLs or RLLs this value is

typically $\leq 2\,\mu\mathrm{m}$. The absorption in the effective lens parabola is described by a_p considering absorption in the first term and surface roughness σ in the second. However, the influence of roughness greatly depends on the momentum transfer q for the transmitted beam at the lens interface. With $q \sim \delta k$ the effect is drastically reduced for x rays since $\delta \sim 10^{-6}$ and may be neglected.
The parabolic profile leads to an increasing absorption with increased distance from the lens apex. The outermost rays passing through the edge of the lens may thus not contribute to the numerical aperture. In order to calculate the diffraction limited spot size later on via the well known *Abbe* or *Rayleigh criterion* (cf. Equation (4.21)) it is convenient to define an effective aperture D_{eff} with [Len+99]

$$D_{\mathrm{eff}} = \sqrt{\frac{1 - e^{-a_p}}{a_p}} 2R_0 \,. \tag{4.17}$$

Another important attribute is the achieved gain G of the optics. It relates to the increase in intensity in the produced focal spot of the optical element compared to a pinhole with equivalent size. The gain is calculated by relating the geometric aperture area of the lens (πR_0^2) to the focal spot area ($^1\!/_4\,\pi B_{\mathrm{h}} B_{\mathrm{v}}$) while considering the transmission of the lens. One derives

$$G = T_p \frac{4R_0^2}{B_{\mathrm{h}} B_{\mathrm{v}}} \,. \tag{4.18}$$

4.3.3 Focal Spot Characteristics

The focal spot of any optics is formed by the convolution of the diffraction limited spot, which is a characteristic of the optical element, and the geometric image of the source, which is related to experimental parameters. When we consider the resulting transverse focus size B in both horizontal (h) and vertical (v) direction we may write

$$B_{\{\mathrm{h,v}\}} = \sqrt{b_{\{\mathrm{h,v}\}}^2 + d_{\mathrm{t},\{\mathrm{h,v}\}}^2} \tag{4.19}$$

with the assumption of both the diffraction limited spot d_{t} and the geometrical image b being of Gaussian shape and are all given as FWHM values. For the optics and x-ray sources considered here this assumption is very well fulfilled. The geometric image size is related to the demagnification of the optics given by the source distance L_{S} and the image distance L_{I} with

$$b_{\{\mathrm{h,v}\}} = \frac{L_{\mathrm{I}}}{L_{\mathrm{S}}} S_{\{\mathrm{h,v}\}} = \frac{f}{L_{\mathrm{S}} - f} S_{\{\mathrm{h,v}\}} \,. \tag{4.20}$$

The diffraction limit of the optics is determined by the wavelength λ of the radiation and the numerical aperture NA of the optics. It describes half the opening angle ϑ of the optics and gives a measure of contributing space frequencies of the spherical wave to the diffraction limited spot. The numerical aperture is given by $NA = n \sin\vartheta = nD_{\mathrm{eff}}/(2L_{\mathrm{I}})$ and takes the refractive index n of the surrounding medium into account. For x rays $n \approx 1$ and thus

$$d_{\mathrm{t}} = \zeta \frac{\lambda}{2NA} = \zeta \frac{\lambda L_{\mathrm{I}}}{D_{\mathrm{eff}}} \,. \tag{4.21}$$

The constant factor ζ is related to the shape of the aperture and is of the order unity. It also depends on the definition of d_{t}. Whether one wishes to express the first zero of the *Airy-disc* pattern or the width

(sigma or FWHM) of a Gaussian fitted to the central peak of the Airy-disc. Here, we measure d_t as FWHM width and for a Gaussian lens aperture $\zeta \approx 0.75$. Since lens stacks will not always be limited in their aperture by absorption one should also consider a circular lens aperture with $\zeta \approx 1$ (for the FWHM focal spot size as opposed to the well known 1.22 for the first zero point).

To achieve smallest focal spot sizes both the geometrical image $b_{\{\mathrm{h,v}\}}$ and the diffraction limited spot size $d_{\mathrm{t},\{\mathrm{h,v}\}}$ have to be minimized (cf. Equation (4.19)). In all experiments within this work the geometrical image $b < d_\mathrm{t}$. The source is sufficiently small and its distance is large enough from the lens so that the demagnification is very large. The domination of the focal spot by d_t also implies that the optics aperture was illuminated coherently, meaning that the lateral coherence length ξ_t at the lens aperture is larger than D_eff. This condition must be fulfilled in order to conduct coherent imaging experiments described in Chapter 5. From Equation (4.19) and (4.21) it is apparent that small foci demand high numerical apertures and coherently illuminated optics. On the other hand, these large opening angles also result in a decrease in focal depth, which may constrain the sample thickness. When moving out of focus the beam size increases continuously according to NA. The depth of focus B_l is defined by a widening of the beam to the value $\sqrt{2}B_{\{\mathrm{h,v}\}}$. Using the beam caustic for refractive lenses from [Len+99] one can derive

$$B_\mathrm{l} = \sqrt{\frac{2}{\ln 2}}\frac{B_{\{\mathrm{h,v}\}}}{NA} \overset{b<d_\mathrm{t}}{\propto} \frac{\lambda}{NA^2} \,. \tag{4.22}$$

The scaling of the focal depth B_l with NA^{-2} only holds in the coherent or diffraction limited case where $b < d_\mathrm{t}$. Otherwise the relation b/d_t is relevant. In the x-ray regime numerical apertures are very small. Refractive lenses used in this work have NA in the range 10^{-3} to 10^{-4}. Thus, the depth of focus is usually more than three orders of magnitude larger than the transverse focal spot size. For example a $100\,\mathrm{nm}$ diffraction limited focal spot will typically have a length of $100\,\mu\mathrm{m}$.

4.3.4 Chromaticity

Refractive lenses have an inherent chromaticity due to the dispersion in the lens material. However, for most storage ring applications this is not an issue as monochromators are used most of the time, enforcing narrow bandwidths of $\Delta E/E \approx 1.4 \times 10^{-4}$. But at the latest XFELs chromatic aberrations become important when conducting experiments. Refractive lenses made of beryllium are, amongst reflective mirrors, one of the few available optics that withstand the high-intensity XFEL pulses [Sch+01; Sch+04]. However, these SASE pulses have a broad bandwidth of $\Delta E/E \approx 2 \times 10^{-3}$ (cf. Section 3.3). Thus, chromaticity will be briefly discussed in the context of a highly coherent beam, where source size and distance are negligible ($B = d_\mathrm{t}$ and $L_\mathrm{I} = f$).

The position of the focal plane z_F is given by Equation (4.13). Note that this is not the focal length f (Equation (4.14)). The focal length will change considerably more for very thick lenses ($\omega L \to \pi/2$) due to an additional shift of the principal plane within the lens [Pat10]. We can derive the change in focal position from Equations (4.13), (4.11), and (2.20):

$$\frac{dz_F}{dE} = \frac{d}{d\omega}\left(\frac{\cot(\omega L)}{\omega}\right)\frac{d\omega}{d\delta}\frac{d\delta}{dE} \qquad \longrightarrow \qquad \Delta z_F = \underbrace{\left(\cos(\omega L) + \frac{\omega L}{\sin(\omega L)}\right)}_{=:\alpha_F} f\frac{\Delta E}{E} \,. \tag{4.23}$$

For a thin lens ($\omega L \to 0$) the chromaticity parameter $\alpha_F \to 2$, whereas for a thick lens $\alpha_F \to \pi/2$. A

comparison of the different scaling between changes in focal length Δf (by α_f with $\Delta f = \alpha_f f \Delta E/E$), focal plane position Δz_F (by α_F with Equation (4.23)), and principal plane position Δz_H (by α_H with $\Delta z_H = \alpha_H f \Delta E/E$) is shown in Figure 4.5.

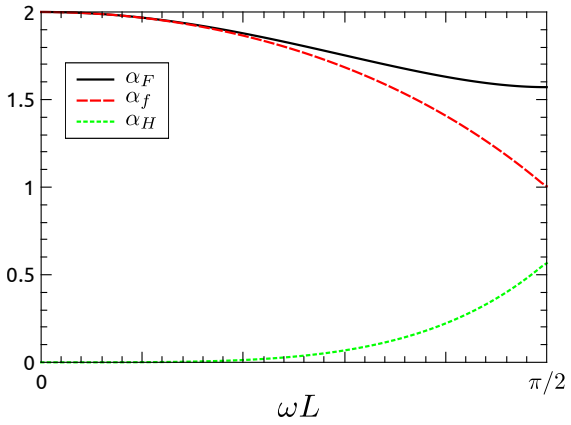

Figure 4.5: Chromaticity parameters for focal plane position α_F, focal length α_f, and principal plane α_H as a function of the lens parameter ωL. (adapted from [Pat10])

The influence of the focal plane shift can be neglected if the lateral beam size due to chromaticity is equal or smaller than d_t:

$$\Delta z_F NA \leq d_\mathrm{t} = \zeta \frac{\lambda}{2NA} = \zeta \frac{\lambda f}{D_\mathrm{eff}} \,. \tag{4.24}$$

With Equation (4.23) we can derive a condition for the tolerable bandwidth

$$\frac{\Delta E}{E} \leq \frac{2}{\alpha_F} \zeta \frac{\lambda f}{D_\mathrm{eff}^2} \,. \tag{4.25}$$

We can now estimate the total lateral beam size B by a convolution:

$$B = \sqrt{d_\mathrm{t}^2 + (\Delta z_F NA)^2} = \sqrt{d_\mathrm{t}^2 + \left(\alpha_F \frac{D_\mathrm{eff}}{2} \frac{\Delta E}{E}\right)^2} \,. \tag{4.26}$$

For a given lens set and experimental bandwidth the spot size can be calculated with the given equation. In the case of a Gaussian aperture that is dominated by attenuation in the lens, both d_t and D_eff scale with $\sqrt{f}$ and the relative influence of the chromaticity is independent of the focal length [Sei+14b]. However, when using available beryllium CRLs at XFELs this is typically not the case and the aperture resembles a truncated Gaussian. In this case the scaling of D_eff and hence d_t is more complicated.

To highlight the focal broadening in dependence of the focal length f we will consider a theoretical lens stack at $E_\mathrm{ph} = 8.2\,\mathrm{keV}$ made of Be lenses with $R = 50\,\mu\mathrm{m}$, $l = 1.1\,\mathrm{mm}$, and $2R_0 = 300\,\mu\mathrm{m}$ as used later on in Chapter 6 (cf. Table 6.2). These parameters give us a fixed refractive power per unit length ω (cf. Equation (4.11)). By varying the virtual lens length L up to L_c we can decrease the focal length towards $f_\mathrm{min} = 1/\omega$ (see Equation (4.15)). The chromatic broadening in relation to the diffraction limit is depicted in Figure 4.6. The white line delineates the border between diffraction and chromaticity limited spot size ($\Delta z_F NA = d_\mathrm{t}$). The lens stack discussed throughout Chapter 6 is highlighted by the white triangle, where $(\Delta z_F NA)/d_\mathrm{t} \approx 4.3$ and the focal spot is significantly dominated by the x-ray bandwidth. While a monochromator was used to characterize this lens set, the broadening with the pure SASE beam is interesting for applications demanding smallest spot sizes. A detailed analysis of focal spot intensity profiles for a perfect CRL and for the aberrated CRL discussed in Chapter 6 can be found

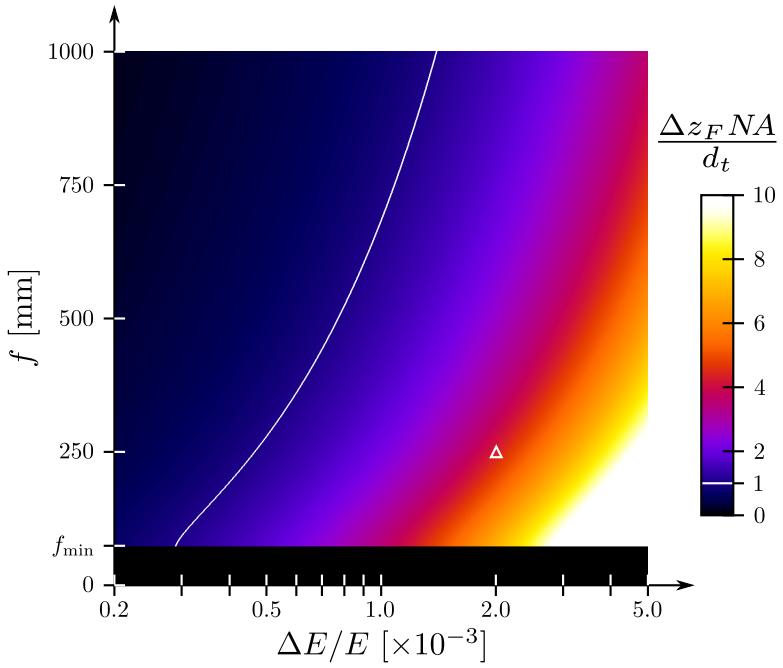

Figure 4.6: Chromatic broadening $\Delta z_F NA$ relative to the diffraction limit d_t as a function of bandwidth $\Delta E/E$ and focal length f The experimental situation at LCLS is highlighted by the triangle.

in [Sei+14b]. It is shown that a broadening of the focal spot is less critical with the aberrated lens, as the focal spot is already significantly increased due to spherical aberrations and chromatic broadening is only a minor contribution. However, the case is different for perfect lenses and hence also for the aberration corrected lens presented in Chapter 6. If highest intensities of the XFEL beam are of interest (e. g. to heat samples), one has to consider the higher energy of SASE beams versus the increase in focal spot size of chromatic optics in order to find optimal experimental parameters. With the emerging seeded SASE beam another option besides monochromators becomes available to decrease bandwidth while achieving higher pulse energies as compared to a monochromatized SASE beams.

4.4 Material Choices for Refractive X-Ray Optics

Throughout the preceding chapters we discussed x-ray interaction with matter and derived properties for refractive lenses. The mass attenuation coefficient μ/ρ is strongly dependent on the atomic number Z of the material (cf. Figure 2.5) due to varying electron binding energies, whereas the specific refraction δ/ρ is nearly constant for all elements distant of any absorption edges. The general rule of thumb is to use materials with low atomic number Z to minimize absorption and high density ρ in order to maximize refraction. At first, a high ratio δ/μ seems to be desirable. Here, lithium shows a superior value. But due to its extremely low density refractive power per unit length is very weak and too many lenses are needed to achieve focal spot sizes below $100\,\mathrm{nm}$, increasing attenuation [Sch+03].

Thus, the selection of an appropriate material is beyond a high δ/μ ratio. Nowadays most relevant properties of x-ray optics are diffraction limited spot size d_t and gain G. Small spot sizes are needed for highest resolution in conventional scanning microscopy were the sample is scanned through a confined beam and, for example, absorption and emission spectra are recorded. Here, resolution is limited by the beam size. Modern coherent scanning microscopy techniques like ptychography (cf. Section 5.2) depend not so much on the beam size, but rather on the applied coherent intensity to the sample [SS10; Sch+12]. This favors gain G over d_t since a small focus is inferior if transmission and thus intensity in the focal

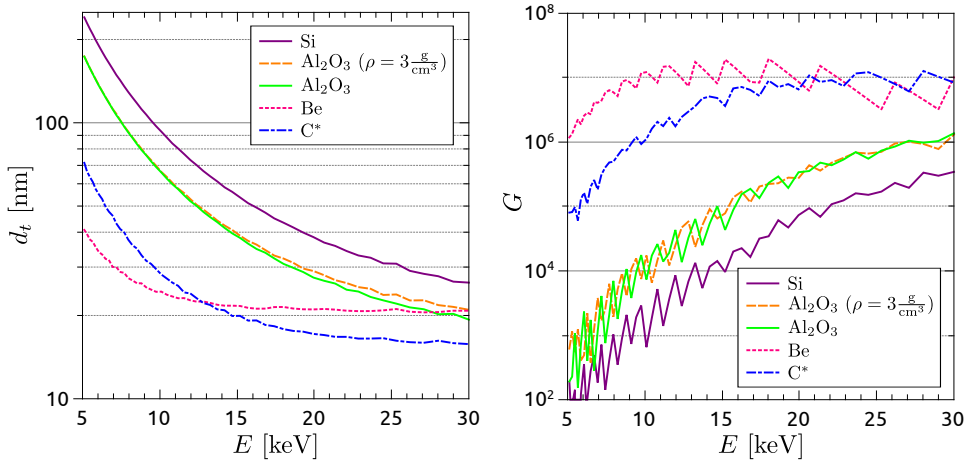

Figure 4.7: Diffraction limited spot size d_t and gain G for parameter optimization towards minimum achievable d_t (constraints: $WD > 10\,\mathrm{mm}$, $R \geq 5\,\mu\mathrm{m}$, $10\,\mu\mathrm{m} \leq 2R_0 \leq 400\,\mu\mathrm{m}$, $d = 1.5\,\mu\mathrm{m}$, and $L \leq 500\,\mathrm{mm}$).

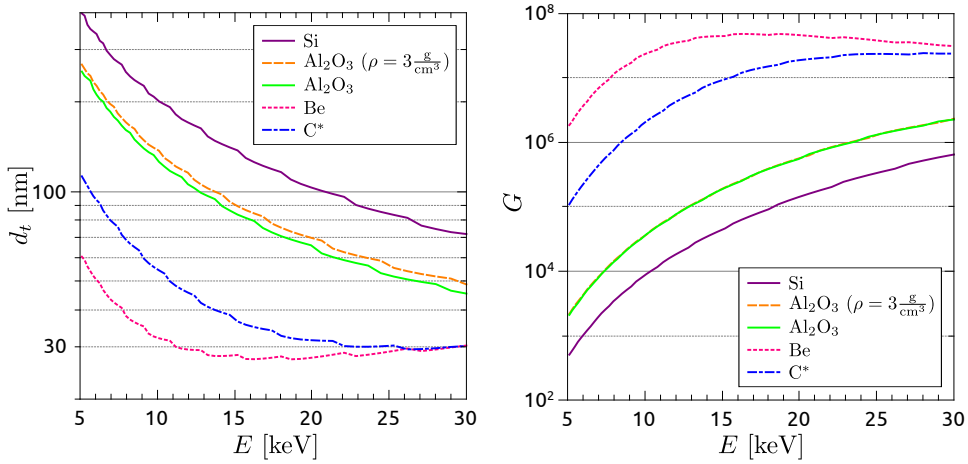

Figure 4.8: Diffraction limited spot size d_t and gain G for parameter optimization towards maximum achievable G (constraints as in Figure 4.7). This optimization will always use the highest available R_0 with the smallest R in order to collect as much intensity as possible.

plane decrease stronger than the focus area.

In order to assess different materials we will compare relevant ones (Be, diamond C*, Al_2O_3, Si) under the two scenarios of minimized d_t and maximized G. The boundary conditions are as follows: We demand $R \geq 5\,\mu\mathrm{m}$ which is still feasible for Si or Al_2O_3 but only theoretical for Be and C* due to current manufacturing techniques. The focal spot should be at least $10\,\mathrm{mm}$ in front of the lens to ensure space for real experimental scenarios (working distance WD). The aperture is limited to $10\,\mu\mathrm{m} \leq 2R_0 \leq 400\,\mu\mathrm{m}$ and the total lens should be $L \leq 500\,\mathrm{mm}$ long. The thickness d at the lens apex is set to $d = 1.5\,\mu\mathrm{m}$, which is again feasible for Si and Al_2O_3 but not for Be and C* at the moment. Results are plotted in Figure 4.7 for an optimization of d_t and Figure 4.8 for optimized G. Due to the finite search space some graphs oscillate, especially in the G plot. This phenomenon occurs when at a given curvature R the aperture R_0 is increased to reduce d_t for higher energies. At a certain point the next available curvature R is favorable instead of increasing R_0 further. Within the presented lens materials Si is the worst choice. Due to its high Z attenuation is strong. In addition the density $\rho_\mathrm{Si} = 2.33\,\mathrm{g\,cm^{-3}}$ is not that high, leading

to moderate refraction in the material. Both achievable d_t and G are only mediocre. Nevertheless the material is used to produce nanofocusing optics [Sch+03]. Reason is foremost the very high quality of substrate materials from single crystals and highly developed manufacturing techniques originating from the semiconductor industry. Thus, very small lenses with radii of curvature of $R = 5\,\mu\mathrm{m}$ are feasible.

Recently, also Al_2O_3 was discovered as a lens material [Sei+14a]. While no suitable nanostructuring techniques exist, the deposition of thin films by atomic layer deposition can be used to create lenses with geometric parameters similar to Si (see Chapter 7). Challenge here is the fragile nature of the thin films as well as the amorphous material growth and thus a reduced density of $\rho_\mathrm{Al2O3} = 3.0\,\mathrm{g\,cm^{-3}}$ as compared to $3.95\,\mathrm{g\,cm^{-2}}$ for the crystalline case. While the reduced density causes slightly enlarged focal spot sizes (cf. Figures 4.7 and 4.8 left side), the achievable gain is the same in both cases, since δ/μ is constant (cf. Figures 4.7 and 4.8) right side).

Diamond is a very interesting material for refractive lenses due to the already mentioned low Z and high density of $\rho_{\mathrm{C}^*} = 3.52\,\mathrm{g\,cm^{-3}}$. But attenuation in C* is stronger than in Be below roughly $40\,\mathrm{keV}$ (cf. Figure 2.5). That is, why diamond is outperformed by Be for low energies below $13\,\mathrm{keV}$ if optimizing for d_t (cf. Figure 4.7). Above that energy Be is already limited by Compton scattering while for C* the superior refractive strength is beneficial. Due to the higher absorption the gain of a C* lens is always lower than for Be until both materials are in a regime dominated by Compton scattering above $40\,\mathrm{keV}$.

For lower photon energies the material of choice is Be. It is superior in minimal achievable focal spot size d_t and provides the highest gain G over the whole plotted energy range. Beryllium is extremely well suited due to $Z = 4$ and its high density $\rho_\mathrm{Be} = 1.848\,\mathrm{g\,cm^{-3}}$ as compared to its neighbor Li, which we dismissed at the beginning.

However, problems with C* and Be arise from available material qualities and structuring techniques. As mentioned earlier in Section 4.2 diamond structuring is difficult and promising techniques are currently evolving. While substrate qualities increased and monocrystalline substrates are available, surface shape and roughness are still inferior. Nevertheless, new approaches of short-pulse high-intensity laser microstructuring may lead to high quality diamond lenses. On the other hand beryllium CRLs are commercially available and the manufacturing process is highly sophisticated. However, Be substrate quality and the current cap of $R > 50\,\mu\mathrm{m}$ limit the performance. Over the years several Be substrates were evaluated and today quality Be substrates with reduced small angle x-ray scattering exist (Materion Beryllium X-Ray IF-1) that have been successfully used in coherent imaging experiments [Sch+13; Sch+15].

To compare Si and Al_2O_3 lenses with Be and C* we will use additional constraints on the two latter to account for available or foreseeable fabrication techniques. These constraints are: The radius of curvature is limited to $R \in \{12, 50\}\,\mu\mathrm{m}$ with a lens thickness of $l \in \{0.5, 1.0\}\mathrm{mm}$ (corresponds to available Be substrates). This leads to apertures of $2R_0 \in \{150, 214, 300, 440\}\,\mu\mathrm{m}$. Due to the embossing process the residual thickness at the apex is set to $d = 30\,\mu\mathrm{m}$. These values represent current geometries of Be CRLs for $R = 50\,\mu\mathrm{m}$. Consequences of substituting Be with C*, smaller curvatures and a comparison to Si and Al_2O_3 are given in Figure 4.9.

If optimized for gain G (right side of Figure 4.9) we see the same behavior as in the prior graphs. Be and C* dominate due to superior δ/μ. The optimized achievable spot size d_t (left side of Figure 4.9) is dominated by Be until approximately $17\,\mathrm{keV}$ for $R = 50\,\mu\mathrm{m}$. For lower curvatures of $R = 12\,\mu\mathrm{m}$ this point is already reached at $13\,\mathrm{keV}$, similar to Figure 4.7. Depending on upcoming developments in laser microstructuring of C* [Pol+15; Ter+15], these lenses might be an interesting alternative at higher

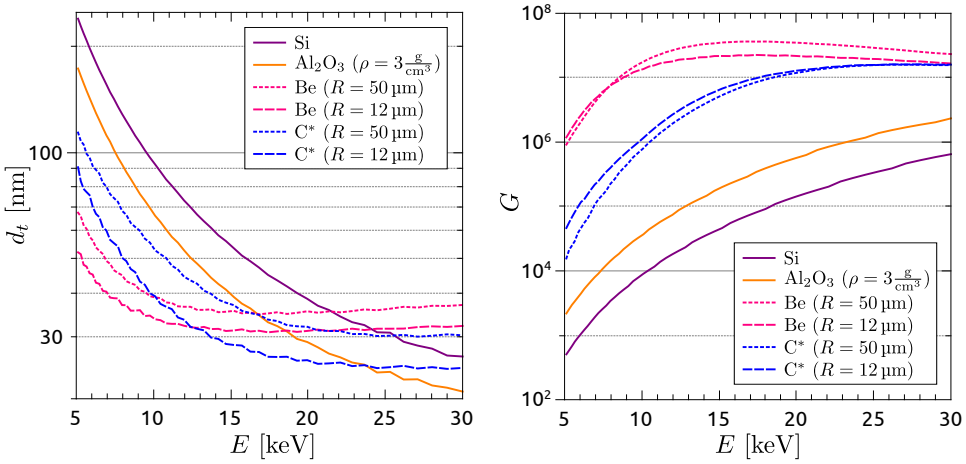

Figure 4.9: Diffraction limited spot size d_t and gain G for parameter optimization towards minimum achievable d_t and maximum G, respectively. While Si and Al_2O_3 have the same constraints as in Figure 4.7, other constraints for Be and C* are enforced to reflect feasible parameters ($R \in \{12, 50\}\,\mu\mathrm{m}$, $l \in \{0.5, 1.0\}\mathrm{mm} \;\rightarrow\; 2R_0 \in \{150, 214, 300, 440\}\,\mu\mathrm{m}$, $d = 30\,\mu\mathrm{m}$).

energies.

All considerations were made under the assumption of perfectly fabricated lenses, as often is not the case. While Si NFLs have a very good shape accuracy, they are limited by the material Si and by the fact that lenses are only one-dimensional, requiring two NFLs in a crossed geometry. The same applies for Al_2O_3, whereas several manufacturing challenges have to be overcome (cf. Chapter 7). Beryllium lenses are in theory very well suited for all applications up to several tens of keV. Unfortunately, shape errors resulting from inaccuracies in the embossing process lead to spherical aberrations, preventing the generation of smallest spot sizes and also high gains. While they are the only refractive lens choice at XFELs, at synchrotron radiation facilities these lenses are mainly used as a prefocusing device to manipulate beam properties at the experimental station, where typically another nanofocusing optics is used (e. g. FZP, NFL, KB-mirror). In this application the minor shape errors are insignificant. Another factor to consider is the large aperture of CRLs of $2R_0 > 300\,\mu\mathrm{m}$, exceeding the horizontal coherence length at most storage rings. Here, nanofocusing is only possible if additional prefocusing lenses are used to manipulate coherence accordingly. In order to effectively use Be CRLs as nanofocusing devices not only at XFELs, where their large aperture and radiation hardness is unchallenged, but also at storage ring sources, the residual aberrations must be corrected.

Characterization and correction of aberrations in Be CRLs will be the main topic throughout the rest of this thesis. Chapter 5 will describe the determination and quantification of aberrations in x-ray optics and outline a possible solution in the form of a corrective phase plate. In Chapter 6 experiments are presented and evaluated to assess the performance of the corrected Be CRL.

5 Optics Characterization and Aberration Correction

Optical elements are used in a broad range of scientific areas, covering nearly the complete electromagnetic spectrum. Performance and quality of these optics often play a crucial role for the specific application. Highest advanced optics and characterization methods can be found in the visible light regime. The easy observation by eye has led to an incredible fast development in this area.

Today, a variety of different optical tests exists [Mal07], while only a few of them are applicable in the x-ray regime. Limitations are mainly imposed by the extremely small wavelength of x rays ($10^{-10}\,\mathrm{m}$), leading to completely different optical properties for all materials in the x-ray regime (cf. Section 2.2). Also the unavailability of highly coherent x-ray sources for a long time (cf. Chapter 3), demanding manufacturing criteria for test samples, and the lack of low-noise x-ray detectors with suitable resolution and efficiency were problematic.

In the beginning of x-ray based research the demand for optics characterization was low. In the 20th century, after the discovery of x rays in 1895, main research fields included full-field absorption imaging used in medical applications and diffraction on solids for structure determination. Both techniques have very low demands on x-ray optics - they work without any or only rely on simple slits to define the area exposed to x rays.

For a long period the only available sources for x rays were x-ray tubes. Later on synchrotron radiation sources became available. While temporal coherence of x-ray beams could be very high with the help of crystal monochromators, they all suffered from very low lateral coherence. Nevertheless, the increased brilliance of these sources and the desire to probe samples more locally led to the advent of x-ray optics (cf. Chapter 4). Thus, the need was born to characterize their focusing properties. The simplest technique to adopt from visible light optics is the knife-edge test. For visible light one can even identify transversal aberrations by partially blocking the beam in one plane while observing appearing shadows over the aberrated region [Mal07]. For x-ray optics this test is simplified by measuring only the total intensity with a simple point detector. While scanning the highly absorbing knife-edge across the beam in horizontal and vertical direction, one can deduce the overall beam size by a simple deconvolution of the measured intensity signal with the known knife-edge shape. Also fluorescence signals or diffraction from the knife-edge itself can be evaluated [Kan+06; Suz+05], although signal levels may be too low to characterize side lobes. In addition, the test may be limited by knife-edge quality and the problem to find thin enough knife-edges that fully block the beam. This gets crucial when focal spot sizes are very small ($d_t < 50\,\mathrm{nm}$) and the focal depth is in the range of a few micro meters.

More advanced optical tests often require a coherent beam since they are based on interferometry. For x-ray optics it was impossible for a long time to illuminate their aperture coherently. The continuous development of synchrotron radiation sources during the last decades has led to facilities of the 3rd generation (cf. Section 3.2) and x-ray free-electron lasers (cf. Section 3.3) that now provide sufficiently small sources in order to coherently illuminate suitable x-ray optics and several new beam characterization methods evolved. These advanced optical characterization methods that are used in this work will

be briefly described in the following sections. With the information gained on wave-field errors methods are described on how to correct aberrations, in principle, for any kind of x-ray optics.

5.1 Ronchi Test

The Ronchi test is a shearing interferometry method first described by Italian physicist Vasco Ronchi in the 1920s [Ron64]. It was used to characterize telescope lenses and mirrors. For the Ronchi test a grating is placed in the vicinity of the focal plane. Depending on the grating period g the incident beam gets diffracted into the m-th order. The diffraction angle ϕ_m is given by

$$\sin \phi_m \approx NA = \frac{m\lambda}{g} \,. \tag{5.1}$$

Depending on the given wavelength λ and numerical aperture NA of the optical element a grating period g can be chosen so that the orders overlap by half as shown in Figure 5.1. If the incident beam has

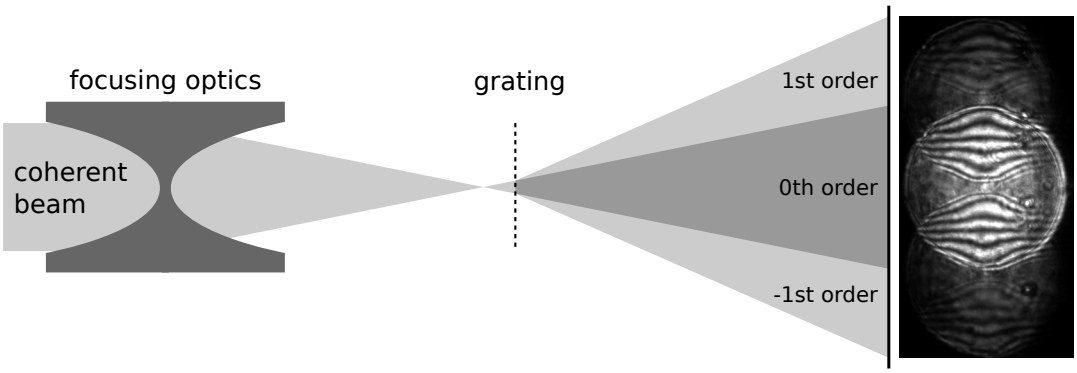

Figure 5.1: Schematic of the Ronchi test. The grating is illuminated by a divergent coherent x-ray beam formed by a focusing optics. The diffraction orders of the grating overlap exactly by half, if the grating period g is chosen so that $g = \lambda/NA$. Interfering diffraction orders create a distinct pattern on the two-dimensional x-ray detector.

sufficient coherence properties, that is a lateral coherence length of at least half the optics aperture, the wave-field amplitudes of different orders can interfere with each other. If the grating period g is chosen such that $g = \lambda/NA$, the zeroth-order interferes only with the first-order amplitudes since they overlap exactly by half (cf. Figure 5.1). The visible interference pattern is called a Ronchigram. If g is too large, the diffraction angles would decrease and all kinds of amplitudes from many orders could interfere with each other, making the interpretation of the measurement difficult. If g is chosen too small, the beam gets diffracted to large angles and different orders do not overlap at all so that no interference can be observed.

Another important aspect is the diffraction efficiency, describing the fraction of the incident light that gets diffracted in the different orders. For the Ronchi test with the desired diffraction geometry described before the best contrast is achieved if the $m = 0$ and $m = \pm 1$ orders are equally strong. In the context of this work we use a grating that can best be described by a simple binary phase grating with a ratio between lines and spaces of $50\,\%$ and a phase shift $\Delta\varphi$. For this kind of grating the diffraction efficiency η is given by [Goo05]

$$\eta_m = \frac{1}{2}\left(1 - \cos \Delta\varphi\right) \mathrm{sinc}^2\left(\frac{\pi m}{2}\right) \,. \tag{5.2}$$

Note that only odd diffraction orders exist for that kind of grating due to the lines and spaces ratio being exactly 1:1 and thus $\eta_{m=\text{even}} = 0$ due to $\text{sinc}(n\pi) = 0$. With $\sum_{n=1}^{\infty} \text{sinc}^2(\pi m/2) = 1/2$ the total intensity in the diffraction orders, accounting for both positive and negative ones, is $2\sum_{n=1}^{\infty} \eta_m = (1 - \cos\Delta\varphi)/2$. This also gives us the intensity for $m = 0$ which is the not diffracted portion of the incident light with $\eta_0 = (1 + \cos\Delta\varphi)/2$. The ideal phase shift to achieve an equal amount of intensity for $m = \{0, \pm 1\}$ is then given by

$$\Delta\varphi = \arccos\left(\frac{4 - \pi^2}{4 + \pi^2}\right) \approx 0.64\pi \; . \tag{5.3}$$

This results in $\eta_{\{0,\pm1\}} \approx 0.29$. The remaining intensity is found in higher diffraction orders. The grating thickness d should be chosen in a way so that $k\delta_{\text{grating}}d = 0.64\pi$ for best contrast in the experiment.

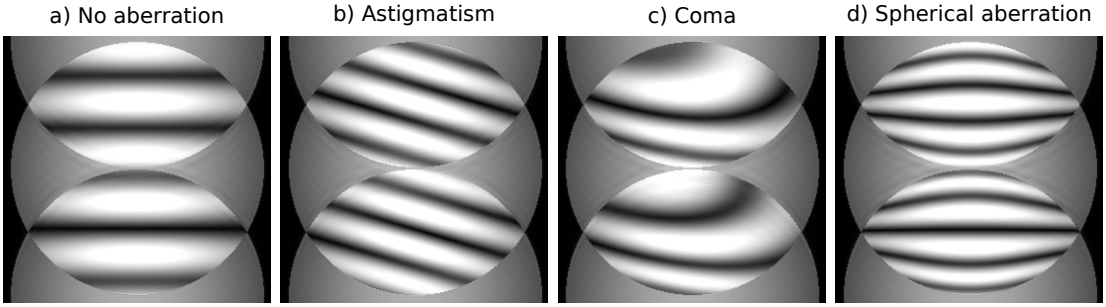

Figure 5.2: Simulated Ronchigrams for an optical system with (a) no aberration, (b) astigmatism, (c) coma, and (d) spherical aberration.

A series of simulated Ronchigrams for a perfect optical system and common aberrations of x-ray optics is shown in Figure 5.2. In visible light optics these aberrations are often described by a set of basis functions called Zernike polynomials Z_ν^μ. The subscript ν denotes the order of the aberrations. The superscript μ is called angular frequency and describes the repetition of the pattern. The Zernike polynomials can be described by

$$Z_\nu^\mu(r,\phi) = R_\nu^\mu(r)\cos(\mu\phi) \quad \text{and} \quad Z_\nu^{-\mu}(r,\phi) = R_\nu^\mu(r)\sin(\mu\phi) \; ,$$

where ϕ is the azimuthal angle and r the normalized radial distance. The radial polynomials R_ν^μ are defined as

$$R_\nu^\mu(r) = \sum_{k=0}^{(\nu-\mu)/2} \frac{(-1)^k(\nu-k)!}{k!(\frac{\nu+\mu}{2}-k)!\,(\frac{\nu-\mu}{2}-k)!}\, r^{\nu-2k} \qquad \text{if } (\nu-\mu) \text{ is even}$$

$$\text{and} \quad R_\nu^\mu(r) = 0 \qquad \text{if } (\nu-\mu) \text{ is odd.}$$

In the context of this work Zernike polynomials up to Z_8^0 will be used to describe measured aberrations in the lens pupil by ptychography. With this approach certain types of aberrations can be quantified and their development with aberration corrections can be monitored. The strength of each aberration is controlled by Zernike amplitudes or coefficients $c_\nu^{\pm\mu}$. The Zernike polynomial Z_0^0 is called piston and relates to a phase offset, Z_2^0 is defocus, Z_1^1 and Z_1^{-1} are tilt. Basic spherical aberrations and higher orders are represented by Z_4^0, Z_6^0, Z_8^0 and so on. Other polynomials are related to coma and astigmatism of basic and higher orders.

5.2 Ptychography

Ptychography is a scanning coherent x-ray diffraction imaging (CXDI) method that was first described by Hegerl and Hoppe [HH70] in the context of electron microscopy. It is one of many iterative phase retrieval methods developed in the 1970s for electron microscopy and astronomy [Fie82]. At first, with the advent of coherent x-ray sources, only methods trying to solve the phase problem from a single diffraction pattern alone found application in the x-ray community [Mia+99; Mar+03]. The limitation to object sizes equal or smaller than the illuminating x-ray beam led to the development of algorithms using a shifting illumination [RF04]. Nevertheless, an accurate model of the illuminating wave field was still crucial for the convergence of the algorithm. Later on the model was extended such that only minimal a priori knowledge of the illumination is necessary, allowing one to reconstruct the illuminating wave field $\mathcal{P}$ simultaneously with the object $\mathcal{O}$ [Thi+08; MR09]. With these scanning CXDI techniques a spatially confined and coherent x-ray beam is scanned over the sample region while ensuring sufficient overlap between neighboring scan points [Bun+08]. In this way the recorded dataset contains several diffraction patterns that share redundant information. This over-determination is essential for a fast and robust convergence of the phase-retrieval algorithm.

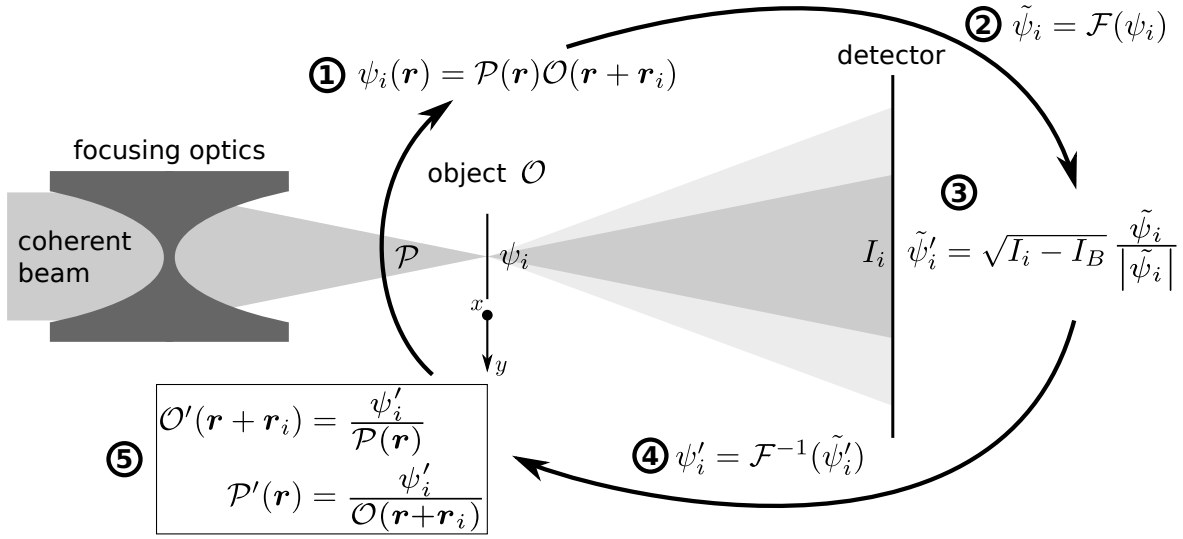

Figure 5.3: Schematic of ptychography setup and algorithm. A coherent probe $\mathcal{P}$ illuminates the object $\mathcal{O}$ at different transverse positions r_i. The intensity I_i of the exit wave field ψ_i is recorded in the far-field by a two-dimensional detector. The algorithm recovers object and probe by an iterative approach in five steps for all positions i: (1) Probe and object are initialized by guess and the exit wave field ψ_i is calculated. The wave field is propagated to the far-field (2) and amplitudes are replaced by measured ones (3) while accounting for background noise I_B. The updated wave field is propagated back into the object plane (4) and both probe and object function are updated (5). One iteration is complete if all positions were used once.

Many algorithmic implementations exist today that can deal with position errors [Mai+12; Zha+13], transverse incoherence [TM13], multiple sample planes [Suz+14], and even broadband x-ray radiation [End+14]. The implementation used in this work is based on the algorithm proposed by Maiden and Rodenburg [MR09] together with corrections for positioning errors and for background noise due to scattering in air and Compton scattering inside the detector material [Bau14]. A sketch of the experimental setup with a simplified algorithm is depicted in Figure 5.3 together with a brief description in the

caption.

One obvious difference to implementations mentioned before is the use of a background intensity I_B. It can describe the noise of air and detector scattering that is neglected by basic algorithms. The idea is that both air and detector scattering remain nearly constant for all recorded diffraction patterns, while the relevant signal changes from pattern to pattern.

Another addition is the correction of object positions $\boldsymbol{r}_i$. In this work a brute-force approach was used that compares the simulated diffraction pattern intensity at neighboring positions to the measured one. The position with the highest correlation is used as the new object position $\boldsymbol{r}'_i$. This correction is typically enabled after probe and object are already sufficiently well reconstructed. The position correction will then rectify sample drifts and other instabilities that may have led to a distorted object.

Object and probe functions are updated for every position and diffraction pattern. The basic formalism given at position (5) in Figure 5.3 is modified in the algorithm:

$$\begin{aligned} \mathcal{P}'(\boldsymbol{r}) &= \mathcal{P}(\boldsymbol{r}) + \frac{\mathcal{O}^*(\boldsymbol{r}+\boldsymbol{r}_i)}{||\mathcal{O}||^2_{\max}+\alpha}(\psi'_i - \psi_i) \\ \mathcal{O}'(\boldsymbol{r}+\boldsymbol{r}_i) &= \mathcal{O}(\boldsymbol{r}+\boldsymbol{r}_i) + \frac{\mathcal{P}'^*(\boldsymbol{r})}{||\mathcal{P}'||^2_{\max}+\alpha}(\psi'_i - \psi_i) \end{aligned}$$

This formalism includes a strong weighting to constraint updates locally and to prevent divergence of the algorithms due to divisions by zero through the regularization parameter α [MR09]. An important modification is the use of the already updated probe function $\mathcal{P}'$ in the object update. Thus, the illumination is always updated before the object and the object update may benefit since discrepancies are caught by the locally varying illumination function.

The algorithm typically converges after a few tens of iterations (each iteration involves all positions and diffraction patterns). With the addition of position refinement a few hundred iterations may be necessary, depending on the magnitude of position errors. Typically, if mainly the illumination function is of scientific interest rather than the object itself, a strongly scattering and well-known test sample is used in order to enhance the scattering signal and facilitate the ptychographic reconstruction. The retrieved complex wave field $\mathcal{P}$ can then be propagated along the optical axis by applying the Fresnel-Kirchhoff propagator (cf. Equation (2.18)) to calculate a beam caustic or to retrieve the wave field directly behind the lens.

5.3 Analysing and Correcting Phase Errors

The two methods described in Section 5.1 and 5.2 offer very different ways to investigate phase errors. Each technique has unique advantages over the other method. The Ronchi test on the one hand side offers a very quick way to get a qualitative feeling for dominant aberrations of an optical system. The ability to recognize the type of aberration and to get insight on the strength of that aberration from a single shot makes this technique appealing for fast beam characterization and its use at an XFEL. However, the drawback of the method is the lack of quantitative results. The modeling relies on the Zernike polynomials described in Section 5.1. While they offer a very fast and intuitive description of aberrations, finer structural details would need the consideration of very high order Zernike polynomials. This, however, introduces a high amount of free variables that have to be refined. Due to uncertainties of

the actual grid nanostructure and resolution limitations of the detector, the refinement of these variables seems to be impossible due to insufficient information.
On the other hand ptychography in combination with Fresnel propagation offers the ability to resolve phase errors in the lens pupil with a few nanometer resolution, limited only by the strength of the diffraction signal at higher angles. However, the need for several diffraction patterns taken from the same sample can lead to challenges when trying to use this technique at extremely high power densities like they are present at XFELs. The problem can be overcome by attenuating the XFEL beam. Another aspect against the method is the slightly longer data acquisition time for several hundreds of diffraction patterns and the more time-consuming reconstruction of the wave field. Since acquisition time and algorithm performance greatly improved recently (on-the-fly scanning mode at XFELs and the use of graphic processors for the algorithm) nanofocused x-ray beams can be characterized by ptychography in a few minutes.

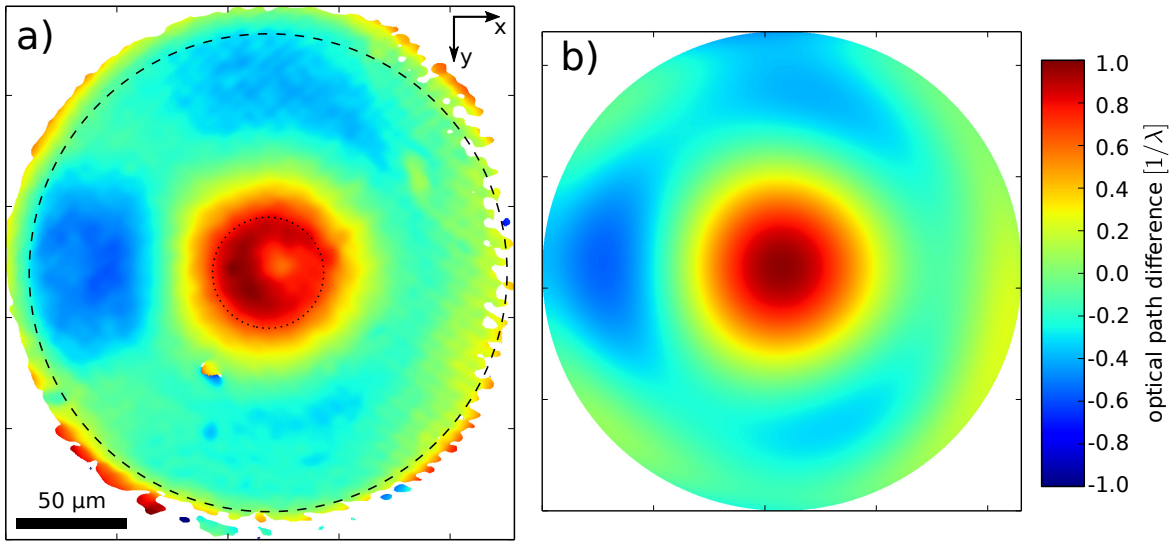

Figure 5.4: Optical path difference at lens exit measured with ptychography and Fresnel propagation (a) versus a Zernike polynomial fit (b). The dashed circle in (a) denotes the fitting region for the Zernike polynomials. The concentric dotted circle in the center is for aligning reference only.

In order to illustrate the difference in level of details of wave-field deformations the phase error at the lens exit is shown as reconstructed with ptychography versus the same measurement fitted to the first 22 Zernike polynomials ($Z_0^0 - Z_6^0$) in Figure 5.4. Please note, however, that for the modeling of Ronchigrams often only the first 8 Zernike polynomials for primary aberrations are considered ($Z_0^0 - Z_3^1$) [Nil+12; Uhl+14] and only one Ronchigram is used for refinement. This leads to an even more inaccurate description compared to ptychography. In the context of this work both methods are used to provide independent results that can be compared to each other, e. g. in Section 6.4.2. The Zernike polynomial decomposition used in this work is calculated with a python library provided by Tim van Werkhoven [Wer12] and involves up to 37 polynomials.

5.3.1 Modeling Shape Errors of CRLs

The first step to correct aberrations of an optical system is to have quantitative information about them, which both the Ronchi test and ptychography can provide. Unfortunately, knowledge of aberrations and

their strength does not mean one can always correct for them. Since accuracy demands on fabrication of x-ray optics are very high, technological limitations are often the main source of errors [Mim+10; CS14; Mor+15]. Therefore, a careful simulation of lens errors in view of manufacturing tolerances and its comparison to experimental data is essential [Kew+10; Vil+11].

In this work the influence of shape errors of parabolic beryllium CRLs will be investigated. In the theoretical model all lenses of a given CRL stack are considered being equal to one another. Each lens is treated like a thin lens, since their focal distance f is very long compared to their thickness l (cf. Section 4.3.1). Within these conditions the lens aperture is illuminated by a spherical wave originating from a distant point source. The beam is propagated from lens to lens with the Fresnel propagator $\mathcal{K}_z(x, y)$ (cf. Equation (2.18)). Each lens is represented by a complex transmission operator $\mathcal{T}(x, y)$ (cf. Equation (2.22)). If the lenses are separated by a distance l_c the propagation trough N lenses can be written as

$$\psi(x, y) = \mathcal{T}\mathcal{K}_{l_c/2} \left[\mathcal{K}_{l_c/2}\mathcal{T}\mathcal{K}_{l_c/2}\right]^{N-2} \mathcal{K}_{l_c/2}\mathcal{T}\psi_0(x, y).$$

The simulated exit wave field $\psi(x, y)$ can now be compared to the previously computed one from ptychographic measurements and the transmission operator $\mathcal{T}(x, y)$ can be further refined. Since the beam converges while propagating through the lenses the problem is not trivial. An educated first guess was made judging from the initial ptychographic measurements and further refined in a few steps by hand.

To assemble the lens stacks that are investigated in this section and later on in Chapter 6 lenses from two distinct production runs were used. Details of these lenses and the number of available lenses N is shown in Table 5.1. Both lens batches labeled “#1” and “#2” show nearly identical properties, except for the gap d at the lens apex. However, as we will see in this section and also in Chapter 6, lenses from these two runs turn out to be not identical in their shape.

Label	Production Date	Material	Lenses N	Curvature R [µm]	Aperture D [µm]	Gap at Apex d [µm]
#1	2011-03-02	Materion X-Ray IF-1	36	50	300	37.2
#2	2012-06-12	Materion X-Ray IF-1	24	50	300	44.7

Table 5.1: Summary of Be CRLs used during all experiments. For a reference of the lens geometry see Figure 4.1(b). In theory all lenses are equal except for a small difference in the material gap d at the lens apex that slightly influences lens transparency.

The investigation of shape errors started with the lens stack called “2012 MEC” and details can be found in Table 5.2. The unique feature of this lens stack compared to all subsequent measurements is its composition of lenses only from batch “#1”.

The measured and computed exit wave field, which were used as a reference for all further efforts to correct aberrations, are shown in Figure 5.5 together with a beam caustic in the vicinity of the focal plane. The reconstructed phase difference from ptychography is noisy at the edge of the aperture and some artifacts originating from either dirt particles on the lenses or from inhomogeneities in the sintered beryllium material can be seen in Figure 5.5(a). Nevertheless, the agreement to the modeled lens stack shown in Figure 5.5(b) is reasonable for the central region. This is proven by the very similar beam caustics in Figure 5.5(c),(d) for the measured and modeled lens stack, respectively.

Since this initial characterization of the lens stack in 2012 at LCLS’ Matter in Extreme Conditions

Label	Facility	Lenses N	Lens Composition	Lens width l_c [mm]	Stack length Nl_c [mm]
2012 MEC	LCLS (MEC)	20	#1	1.1	22
2013 MEC	LCLS (MEC)	30	(#1 + #2)[a]	1.1	33
2013 XPP	LCLS (XPP)	20	(#1 + #2)[a]	1.1	22
2013 DLS	DLS (I13-1)	30	(#1 + #2)[a]	1.1	33
2015 MEC	LCLS (MEC)	20	(#1 + #2)[a]	1.1	22

[a] random composition from both production runs, see Table 5.1 for details

Table 5.2: Overview of different beam-characterization experiments together with the specific lens configuration employed. Except for the first measurement "2012 MEC" individual lenses were taken from two different production runs. All lenses are indistinguishable and the lens composition for experiments past 2012 is unknown.

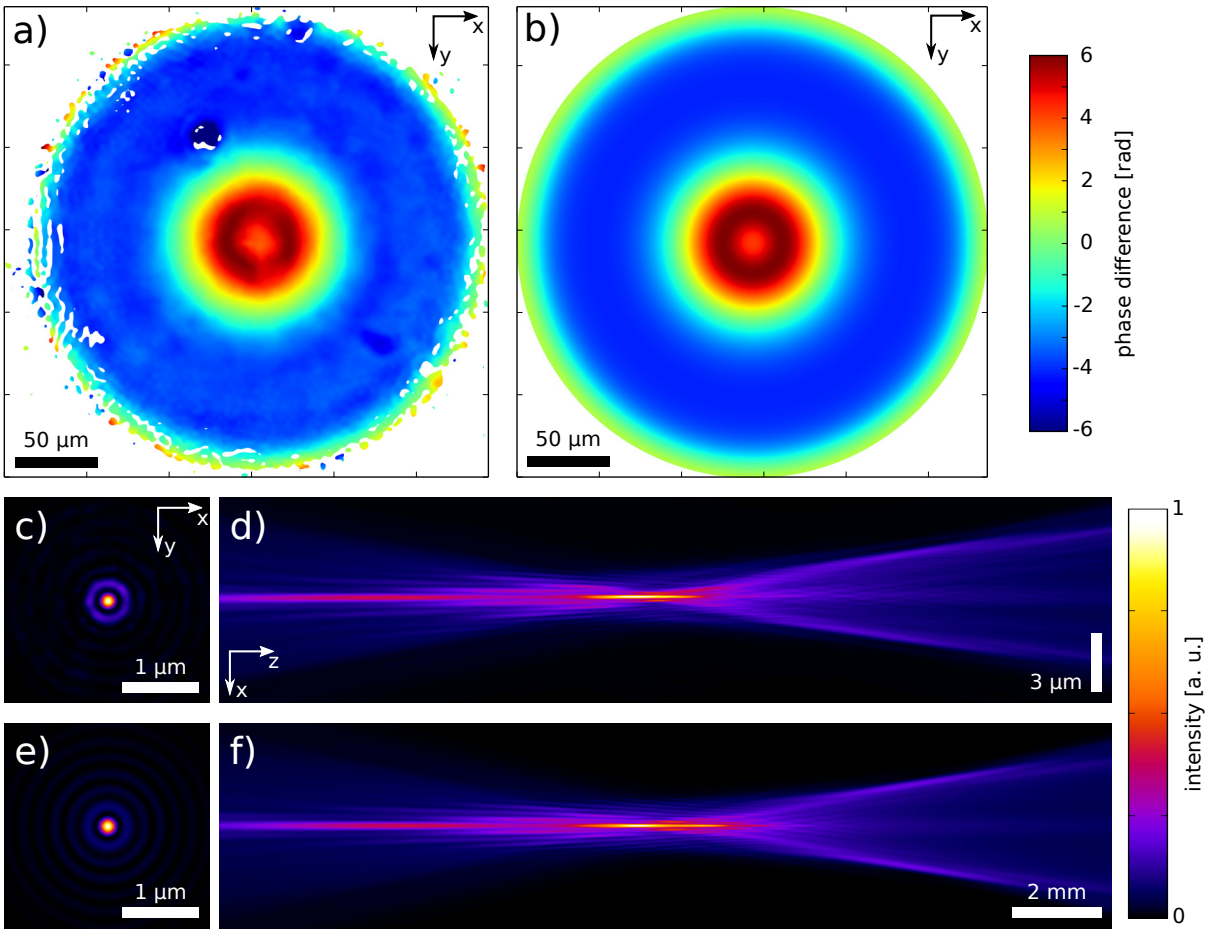

Figure 5.5: Aberrations in the Be CRL lens stack "2012 MEC" (see Table 5.2). Measured phase difference compared to ideal spherical wave at lens exit (a) and corresponding beam caustic (d) in the vicinity of the focal plane (c). Results for the modeled lens stack are shown in (b), (e), and (f) for comparison.

(MEC) instrument, the lenses were used in various experiments at the LCLS (MEC instrument as well as X-ray Pump Probe (XPP) instrument) and also at the Diamond Light Source (DLS) at beamline I13-1 (cf. Table 5.2). In all these experiments we were able to characterize the lens stack with the help of ptychography. The reconstructed wave field was again propagated to the lens exit with the Fresnel

propagator and the phase was compared to an ideal spherical wave. Different horizontal line scans through the center of the wave field along the x-axis for various experiments are shown in Figure 5.6.

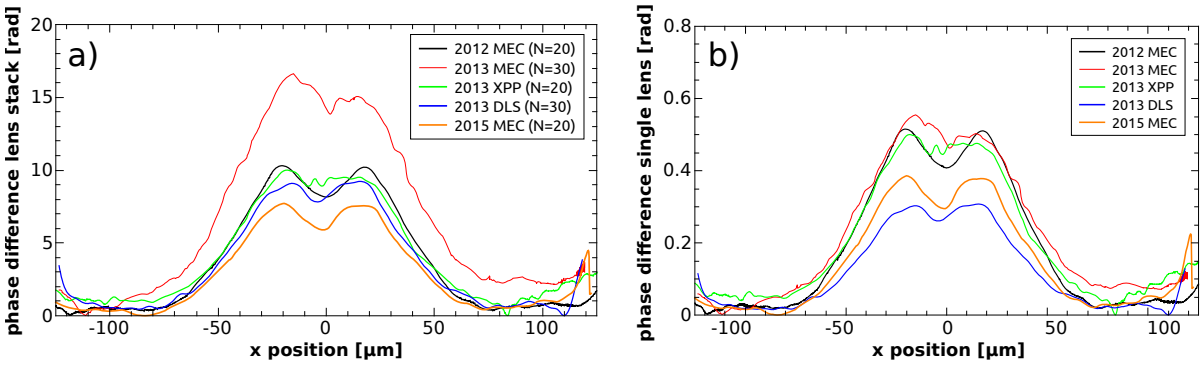

Figure 5.6: Horizontal line scans along the x-axis through the center of the wave field at the lens exit. Shown in (a) is the phase difference compared to an ideal spherical wave for the complete lens stack. Since the number N of individual lenses varied during these experiments, a normalized line scan is shown in (b).

When looking at Figure 5.6(a) two measurements stand out. The blue line of "2013 DLS" with $N = 30$ lenses shows an identical error to experiments using only $N = 20$ lenses. Also the orange line of "2015 MEC" shows a smaller error than the other experiments. This is more emphasized when looking at the normalized plot in Figure 5.6(b). Since lenses from two different production runs were used (cf. Table 5.1 and Table 5.2), one can reason that shape deviations are not consistent between production runs. However, most experiments (3 out of 5) agree well with the initial experiment "2012 MEC" and we can be certain that only lenses from one production batch were used during this particular experiment (as batch "#2" was fabricated after the "2012 MEC" experiment). Thus, the computed shape deviation for a single lens surface (taken from the simulation already shown in Figure 5.6) is presented in Figure 5.7 as a representative overall lens surface shape of the Be CRLs used. The lens surface shape was obtained by iteratively comparing the exit wave field of the lens stack and the computed beam caustic along the focal plane with measured data from ptychography (final simulation results already shown in Figure 5.5) and changing the shape of all lenses in the stack simultaneously. The simulated shape plotted with a solid blue line in Figure 5.7 shows nearly a perfect agreement with the parabolic fit represented by the dashed green line. On this scale shape errors are nearly invisible. Thus, the difference between the two is plotted by the solid orange line on a different scale on the right side. Shape errors are smaller than $500\,\mathrm{nm}$ over the whole lens aperture of $300\,\mu\mathrm{m}$. The mechanical coining process of these kind of lenses makes it extremely challenging to correct such small shape derivations. But since every lens is coined in the same way, the relatively small error of a single lens is amplified by stacking many of them. To better understand necessary lens shape accuracies for aberration free focusing a simulation was carried out where the surface shape error was reduced by a factor of five (shape errors $\leq 100\,\mathrm{nm}$ compared to $500\,\mathrm{nm}$). The results in comparison to an ideal aberration free lens stack are shown in Figure 5.8. Even these small shape errors lead to a noticeable shift in the focal distances. This manifests in the slightly visible tail before the focus and split tails of intensity behind the focal plane (Figure 5.8(b)). In the view of the focal plane in Figure 5.8(a) this is discernible by the prominent high intensity ring around the central speckle. Despite the central speckle being of equal size to the perfect lens stack (Figure 5.8(c)), a lot of intensity is lost and found in the surrounding ring. For a perfect lens $93\,\%$ of the total intensity

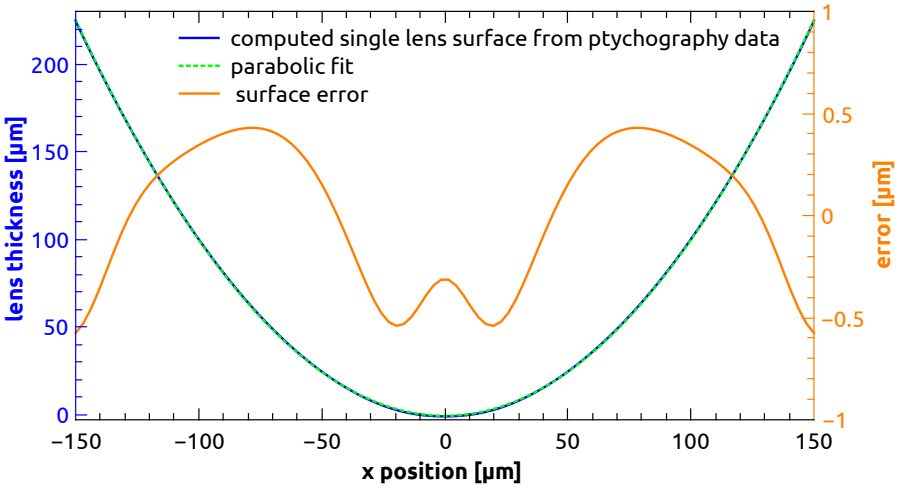

Figure 5.7: Single lens surface shape (solid blue line) computed by iteratively comparing lens stack simulations with measured ptychography data. The solid orange line shows a magnified plot of the surface error, which is the difference between the reconstructed surface error (blue line) and an ideal parabolic lens shape (dashed green line). The corresponding scale bar is given on the right side.

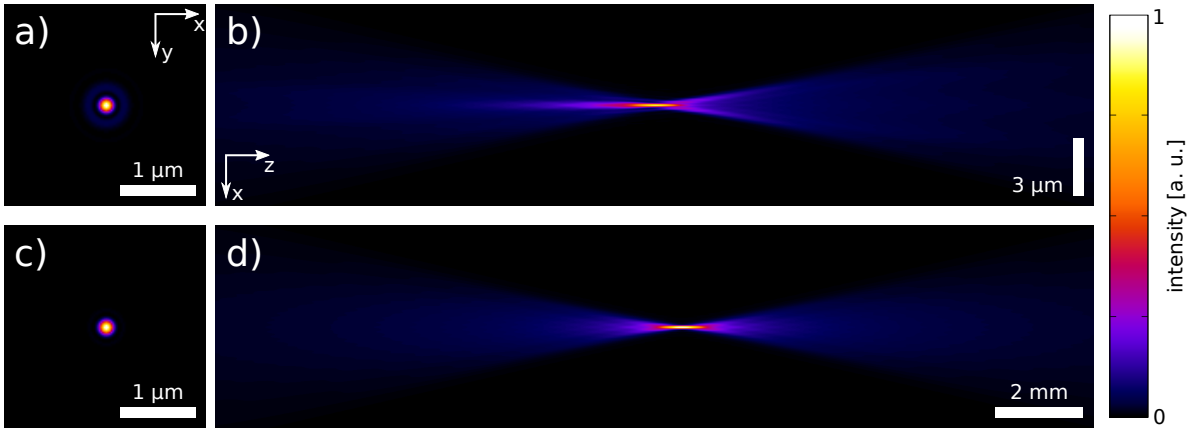

Figure 5.8: Simulated wave field produced by a lens stack with surface shape errors $< 100\,\mathrm{nm}$ (a), (b) and for an aberration free lens stack (c), (d). The intensity distribution in the focal plane (a), (c) is shown next to the beam caustic (b), (d) in its vicinity.

is concentrated within the central speckle. In the slightly aberrated case it is just $68\,\%$. The situation for the simulation of the real aberrated lens stack with only $500\,\mathrm{nm}$ surface deviation is even more dramatic. Only $23\,\%$ of the total intensity is found in the central speckle.

These simulations demonstrate how sensible the focusing quality of the lenses reacts to smallest shape errors. The fact that every lens of the production lot is likely to have similar shape errors leads to a strong increase of aberrations within the stack. Errors of individual lenses add up and contribute to a significant total phase error. Currently it seems impossible to correct the production quality of individual lenses to surface errors $\leq 100\,\mathrm{nm}$. The idea presented in the following sections is to correct shape errors of a certain lens stack with a single optical component. In most relevant applications many lenses (≥ 10) are being stacked in order to achieve desired spot sizes of a few hundred nanometer. The buildup of phase errors during propagation through the lenses allows for relatively relaxed manufacturing tolerances of

the corrective optical component, since the summed up errors are corrected at once. Assuming a similar shape quality of the corrective element like for a single lens surface ($\approx 500\,\mathrm{nm}$), the final phase error for a stack of 20 lenses could be reduced by a factor of 40 (each lens has two surfaces). Even if the production quality of Be lenses could be increased to errors $\leq 100\,\mathrm{nm}$ the single optical element would still be able to reduce total phase errors by an additional factor of 8 (assuming a constant manufacturing error for the corrective element of $\approx 500\,\mathrm{nm}$). Thus, a single corrective element with comparable manufacturing tolerances as the lenses will result in less aberrated optics due to the disadvantageous summation of errors within lens stacks. The concepts for this corrective optical element which we call a phase plate are introduced in the following section.

5.3.2 Phase Plate Design and Materials

The basic idea behind the phase plate is quite simple. We introduce another refractive optical element behind the actual CRL lenses that will correct phase errors by a distinct thickness profile. But when designing such a phase plate we have to cope with nearly the same problems as for refractive lenses. In order to understand the difficulties explained in the next paragraphs, the ideal three-dimensional shape for a phase plate made out of silicon is shown in Figure 5.9.

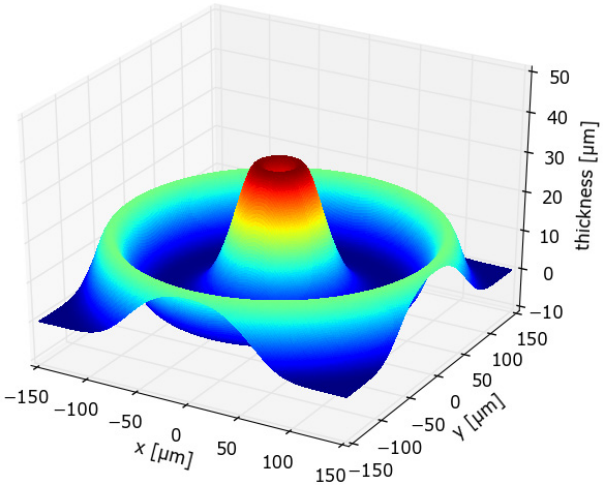

Figure 5.9: Three-dimensional shape of an ideal phase plate out of silicon made to correct aberrations for the lens stack “2012 MEC” (cf. Table 5.2)

Since the lenses and the encountered phase errors are rotationally symmetric, the phase plate has the same property. In the given example with silicon as a phase plate material the central cone should have a thickness of almost $36\,\mu\mathrm{m}$. Ideally, the depicted shape should be produced with surface errors $\leq 1\,\mu\mathrm{m}$. The relatively small diameter paired with the requested thickness profile imposes some challenges when trying to fabricate the phase plate:

Phase plate material: Similar restrictions as for refractive lenses apply. For a very high efficiency the phase plate should be made out of a material that provides strong refraction while keeping attenuation at a minimum. As mentioned in Section 4.4 already this means that a low-Z high-ρ material is required. This includes materials considered before for lens fabrication like aluminum, beryllium, diamond, sapphire, and silicon.

Availability of thin substrates: For typical applications and aberration strength of current Be CRLs the

overall thickness of a phase plate made of any of the afore mentioned materials would be of a few tens of micrometer. Typically, these thicknesses are achieved by polishing the surface of the desired material or by rolling in the case of metals. For all of the mentioned materials suitable thin plates are available.

Ability to structure the material with sufficiently high precision: This is by far the most demanding point for phase plate fabrication. Due to the shape of the phase plate with the central cone and the small dip in the middle, mechanical machining by turning or milling seemed not feasible. While the property of a rotational symmetry would be easily satisfied, the structure is too complex for stamp production. This disqualifies the mentioned metallic materials. Another option would be a lithographic structuring and subsequent etching process. The drawback of these methods is the cylindrical symmetry. Thus, only two-dimensional projections can be realized. To obtain a three-dimensional phase plate structure many projections have to be combined. More sophisticated approaches by selective etching techniques are under development. Structuring by focused ion beams (FIB) looks very promising, but the sheer size of the phase plate and quantity of material that needs to be removed are not in favor of this technique. Recent developments in high-power short-pulse laser systems has led to a new structuring technique of laser ablation. Depending on wavelength, pulse energy, and pulse duration several ablation mechanisms can occur. Here, we use a tightly focused beam of a few micrometers and pulse durations of several femtoseconds. Due to these short pulses the electrons in a small volume of the sample are heated massively, creating a highly excited state of charged ions. Subsequent Coulomb explosions remove these ions from the sample, without introducing heat to the bulk material. This technique seemed very promising and is already used to structure fused silica for optical applications.

Radiation hardness: Corrected CRLs will be predominantly used at XFEL and eventually storage ring sources. Especially at XFELs the lenses are supposed to focus the incoming short pulses down to below $100\,\mathrm{nm}$ in order to create extremely high power densities in the focal spot volume and also to image ultrafast processes in matter with highest spatial resolution. Therefore, radiation hardness of the phase plate, that can withstand these high intensities in a similar way than Be CRLs, is very important. For fused silica the damage threshold is roughly $4.7\,\mu\mathrm{J}\,\mu\mathrm{m}^{-2}$ [Koy+15]. The assumed intensity of a SASE beam with $3\,\mathrm{mJ}$ pulse energy hitting the phase plate of $300\,\mu\mathrm{m}$ diameter would be roughly $0.04\,\mu\mathrm{J}\,\mu\mathrm{m}^{-2}$, which is far below the estimated damage threshold. Thus, a fused silica phase plate should withstand a flat XFEL-SASE beam.

5.3.3 Phase Plate Fabrication

After evaluating all possibilities the decision was made to use the technique of laser ablation and silicon as a starting material. The advantage of silicon is that the material is widely used in the semiconductor industry and can thus be manufactured with a very high purity, is mono-crystalline with low density of defects, and can be ordered with various crystal orientations and substrate thicknesses. The structuring of the phase plates was done at Friedrich-Schiller-Universität Jena in the institute of applied physics. We used a short-pulse laser system of type TruMicro5050 from Trumpf with a wavelength of $1030\,\mathrm{nm}$, pulse energies up to $200\,\mu\mathrm{J}$, and a pulse duration of $8\,\mathrm{ps}$. The problem encountered with silicon were unknown operation parameters for the ablation laser. Despite the technique being used to structure fused silica for visible light optics, a transition to silicon was not easy. Especially surface roughness and the deposition of debris particles were unsatisfying as shown exemplarily in Figure 5.10(a).

Due to these struggles we moved to amorphous fused quartz of type Vitreosil® 077 ($\rho_{\mathrm{SiO_2}} = 2.2\,\mathrm{g\,cm^{-3}}$)

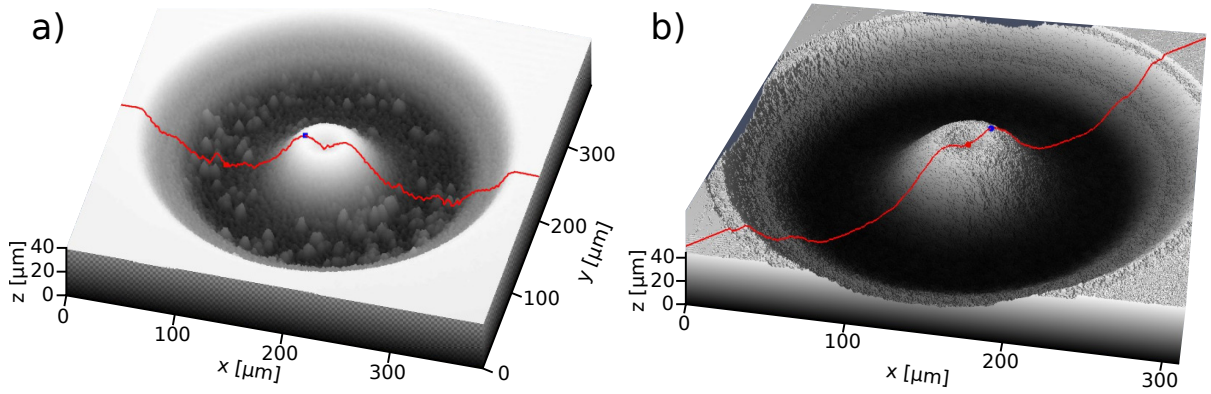

Figure 5.10: Three-dimensional image of prototype phase plates measured by a laser scanning microscope (LSM). For the silicon phase plate undesired deposited debris particles and high surface roughness can be seen (a). When using amorphous SiO_2 as a substrate material the surface roughness could be dramatically reduced (b).

with a nominal substrate thickness of $100\,\mu m$. The results shown in Figure 5.10(b) were promising. The surface roughness could be reduced and almost no debris particles were created during the laser ablation process. Final phase plate surface profiles are plotted against the theoretical necessary thickness for SiO_2 in Figure 5.11. Phase plate 1 (solid black line) and phase plate 2 (solid green line) were used in the experiments presented in Chapter 6. For phase plate 1 the shape on the outer parts matches very well, but the central cone is too thick. For phase plate 2 the central cone is in good agreement with the simulated shape, but the outer parts are too flat. The optimized phase plate (solid blue line) could not be experimentally tested yet.

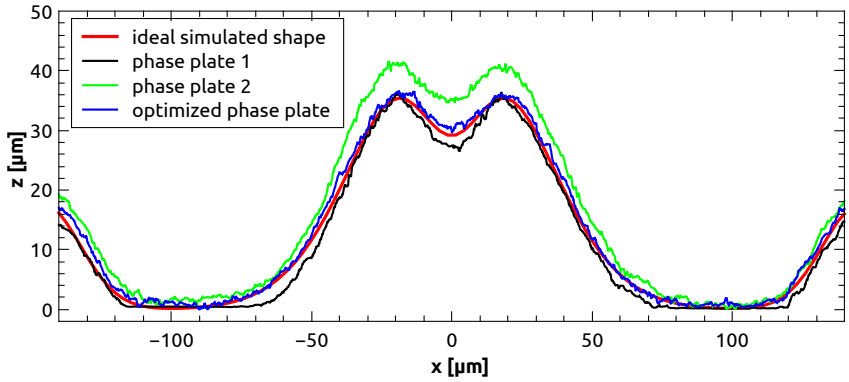

Figure 5.11: LSM surface measurements of various SiO_2 phase plates in comparison to the design goal (solid red line).

Another crucial aspect of the phase plate is its exact alignment with respect to the aberrated lens. Here, the Be CRLs are housed in the center of a cylinder with $12\,mm$ diameter. In order to be able to use the phase plate without any extra alignment, the phase plate was also placed on a cylindrical housing with $12\,mm$ diameter. The challenge here is the concentric positioning of the phase plate with lateral errors $< 5\,\mu m$. A simulation of the degrading beam quality with a misaligned phase plate is shown in Figure 5.12. For the perfectly aligned case (not shown) $92.5\,\%$ of the total intensity is in the central speckle within the focal plane. For a $1\,\mu m$ misalignment as shown in Figure 5.12(a),(b) we still have $91.6\,\%$ of the intensity within the central speckle. For a $2\,\mu m$ displacement shown in Figure 5.12(c),(d)

this reduces to $89.1\,\%$. For $5\,\mu m$ and $10\,\mu m$ shown in Figure 5.12(e),(f) and Figure 5.12(g),(h) we measure $73.6\,\%$ and $41.2\,\%$, respectively. One can see that the intensity decreases drastically beyond a misalignment of $5\,\mu m$. To stay within this tolerance, the raw SiO_2 wafer was glued into the casing before the actual laser ablation process. The casings have a very precise outer diameter of $(12.000 \pm 0.002)\,mm$ with a central hole of $400\,\mu m$ diameter which is concentric to $\pm 4\,\mu m$. Due to restrictions in the available setup the phase plate could only be aligned with respect to the small central hole and not to the much more accurate outer diameter. In the future a more accurate alignment of the phase plate using the outer diameter of the casing as a reference is planned.

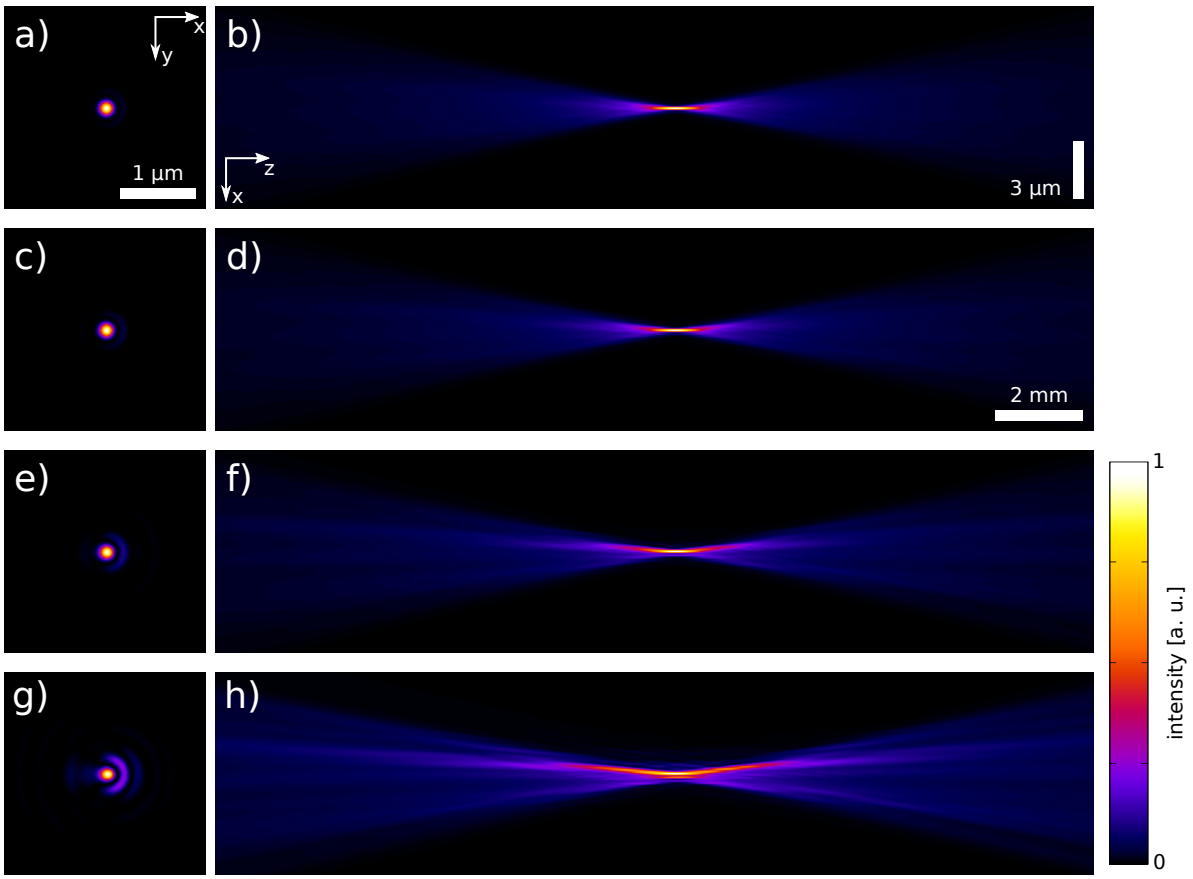

Figure 5.12: Simulated intensity distribution in the focal plane and along the beam axis for a phase plate displacement of $1\,\mu m$ along the x axis (a, b). The distributions for $2\,\mu m$, $5\,\mu m$, and $10\,\mu m$ displacements are shown in (c, d), (e, f), and (g, h), respectively.

6 Aberration Correction for CRLs

In this chapter the phase plate described in Section 5.3.3 is used to correct aberrations in a set of Be CRLs. When initially designing the phase plate, not only the position lateral to the x-ray beam plays an important role to the resulting focusing quality, but also its placement longitudinal to the beam path is crucial. Since the beam converges inside the lens and of course also after exiting, the phase plate diameter has to follow this convergence of the beam when placed at different longitudinal positions. In the experimental scenarios described here, the numerical aperture of the lens stack is $NA \approx 0.5\,\mathrm{mrad}$. The difference in beam diameter directly after the lenses to a position $10\,\mathrm{mm}$ further downstream would only be roughly $10\,\mu\mathrm{m}$ compared to the overall $280\,\mu\mathrm{m}$ diameter of the relevant structured area on the phase plate. Hence, a slightly different position of the phase plate along the beam axis will have far less dramatic effects than lateral displacements discussed in Section 5.3.3.
During prototype production we discovered early that the lateral alignment of the structured phase plate was very difficult on the $12\,\mathrm{mm}$ casing with accuracies $< 5\,\mu\mathrm{m}$. That is why the first prototype called "phase plate 1" (cf. Figure 5.11) was not perfectly centered within its casing. For this reason an easy positioning inside the lens holder together with the other lenses of the stack was not possible if we wanted the phase plate on the optical axis for optimal correction of aberrations. Therefore, the phase plate was placed closely behind the Be CRL holder at a distance z_{l-p} (cf. Figure 6.1). It was mounted on a set of motorized stages to align it laterally to the beam (x-y plane). All further details of the various experimental setups are described in the following section.

6.1 Principal Experimental Setup

The basic setup for experiments at beamline I13-1 of DLS, beamline P06 of PETRA III, and the MEC instrument of the LCLS were very similar when considering only the setup from the Be CRL lens stack further downstream. Main concerns that influenced the beamline setup at storage ring sources were related to lateral coherence issues, whereas at the LCLS the main concerns were to have monochromatic x-ray pulses instead of the full SASE spectrum (cf. Section 3.3) for appropriate longitudinal coherence and reduced intensities in order to not destroy the samples.
When neglecting these beam conditioning aspects further upstream the experimental setup for all scenarios is depicted in Figure 6.1. In all experiments basic properties of the lens stack were kept constant. We always used $N = 20$ Be CRLs with $R = 50\,\mu\mathrm{m}$ that were randomly selected from a pool of available lenses originating from two different production series. Only for the experiment at the LCLS the lenses were screened beforehand with the help of an optical microscope. Lenses with dirt or other visible surface artifacts were sorted out. Depending on whether we recorded Ronchigrams or far-field diffraction patterns for ptychography, detectors and sample – detector distances z_{s-d} varied (cf. Figure 6.1). For example the Ronchi test requires a detector with very high resolution to resolve interference features within the central cone of the beam. For these types of experiments we used a scintillator in combina-

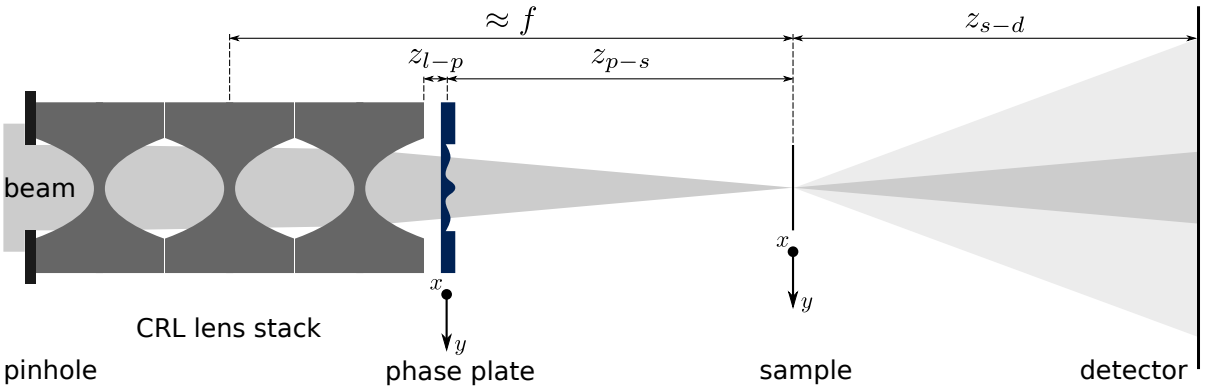

Figure 6.1: Experimental setup. A coherent beam is confined to the lens aperture by a pinhole and focused by the lens at focal distance f. The sample is placed in the vicinity of the focal plane and diffraction patterns are recorded at a distance z_{s-d} by a two-dimensional detector. The aberrated CRL is corrected by adding a phase plate behind the lens at distance z_{l-p}. If the phase plate is outside the lens holder $z_{l-p} \approx 16\,\mathrm{mm}$ and the phase plate can be aligned laterally. If the phase plate is within the lens holder $z_{l-s} \approx 0\,\mathrm{mm}$ and the phase plate is fixed.

tion with a magnifying optical setup that images the scintillator to a CCD camera. This setup was often placed closer to the sample. At the LCLS we used at fibre-coupled PIXIS-XF with $13.5\,\mu\mathrm{m}$ pixel size at larger distances. For ptychography on the other hand one requires a detector that covers a significant solid angle for sufficient resolution in reciprocal space that has, ideally, single photon counting capabilities. Here, we used detectors based on the Medipix 3 chip [Bal+11] called Merlin at DLS [Pla+13] and the LAMBDA detector at PETRA III [Pen+13]. At the LCLS we used a small in-air CSPAD-140k [Her+13] in order to scan a sample using the available repetition rate of $120\,\mathrm{Hz}$. Due to the short LCLS pulse length of about $50\,\mathrm{fs}$, the ptychography samples could be scanned "on the fly", meaning that it was not necessary to stop the sample at each individual scan position. Instead, it could be moved at a small steady velocity of about $1\,\mu\mathrm{m\,s}^{-1}$ while the CSPAD continuously recorded diffraction data at $120\,\mathrm{Hz}$. These detectors were placed far away from the sample in order to guarantee sufficient sampling of the diffraction patterns despite the large pixel sizes of $55\,\mu\mathrm{m}$ and $110\,\mu\mathrm{m}$ for the Medipix 3 based detectors and the CS-PAD, respectively.

A more detailed review about the individual beamtimes will be given in the following subsections.

6.1.1 Experimental Details of I13-1 at DLS

One benefit of CRLs next to their high degree of radiation hardness is undoubtedly their large aperture. This is a highly desired property for the LCLS, where a large part the coherent beam should be captured by the aperture. Unfortunately at synchrotron radiation sources one often struggles to illuminate large optics coherently. In our case the complete aperture of $2R_0 = 300\,\mu\mathrm{m}$ has to be illuminated by a coherent beam in order to perform the Ronchi test or ptychography (cf. Chapter 5). The source size of I13-1 at DLS is given with $S = 400\,\mu\mathrm{m} \times 13\,\mu\mathrm{m}$ (horizontal $\times$ vertical) and the beamline length is roughly $L = 250\,\mathrm{m}$ [Rau+11]. Using Equation (3.10) given in Section 3.4.3 leads to a lateral coherence length of $l_t = 83\,\mu\mathrm{m} \times 2566\,\mu\mathrm{m}$ (h$\times$v) at the used photon energy of $E_\mathrm{ph} = 8.2\,\mathrm{keV}$. While there is sufficient coherence in the vertical direction, the horizontal coherence is poor.

When trying to increase the coherence length in one direction the Ronchi test can be extremely useful for a very fast qualitative analysis. If the lens is illuminated with an x-ray beam having a smaller lateral coherence length than the size of the aperture, the visibility of interference fringes reduces [Uhl+14]. The method to increase horizontal coherence used here was the creation of a smaller secondary source after the undulator by simply closing the horizontal front-end slits to $50\,\mu\mathrm{m}$. This gives a theoretical horizontal coherence length of $667\,\mu\mathrm{m}$ at the experiment. Here, the Ronchi test is very convenient to check the coherence properties of the beam by just maximizing the visibility of interference fringes. Source size can also be increased virtually by vibrating optical components along the beamline, e. g. the cooling of monochromator crystals can lead to vibrations that increase the virtual x-ray source size significantly. This can reduce the lateral coherence properties at the experiment considerably. Here, the cooling of the monochromator was switched off to achieve stable conditions. This was possible since the heat load was drastically lowered due to the reduced front-end slit opening.

6.1.2 Experimental Details of P06 at PETRA III

At PETRA III the diameter of the storage ring is much larger than at DLS. This leads to a reduced horizontal source size. For the undulator used at beamline P06 the source size if given with $S = 82\,\mu\mathrm{m} \times 16\,\mu\mathrm{m}$. Experiments were carried out in the microprobe endstation which is roughly $L = 90\,\mathrm{m}$ away from the source. The lateral coherence length is calculated to $l_t = 146\,\mu\mathrm{m} \times 750\,\mu\mathrm{m}$ at $E_{\mathrm{ph}} = 8.2\,\mathrm{keV}$. Here, another concept was used to correct the degree of coherence to the experimental demands. The beamline is equipped with a set of prefocusing CRLs that can generate a secondary source. With the help of these lenses coherence properties can be adjusted in a wide range. In the experiment we used one Be CRL with $R = 50\,\mu\mathrm{m}$ to create a secondary source of size $11\,\mu\mathrm{m} \times 2\,\mu\mathrm{m}$ at a distance of $L_p = 48.6\,\mathrm{m}$ after the undulator source. Using again Equation (3.10) and $L - L_p = 41.4\,\mathrm{m}$ as the new source distance gives a lateral coherence length of $l_t = 502\,\mu\mathrm{m} \times 2762\,\mu\mathrm{m}$, which is sufficient in order to characterize the aberration corrected optics. We also used the Ronchi test in order to confirm adequate coherence properties during setup.

6.1.3 Experimental Details of MEC at the LCLS

The challenges encountered at XFELs are very different compared to synchrotron radiation sources. This is also reflected by the different setup described here. While coherence properties of the LCLS are very high and the laser can be represented by only one transverse mode in the hard x-ray regime [Gut+12], problems arise from the broad SASE bandwidth and the high peak brilliance of individual pulses. The SASE bandwidth is not only a concern in general when performing CXDI experiments, but as described earlier (cf. Section 4.3.4) is also not favorable when using refractive optics since the focal length changes with x-ray energy. Therefore, we used a four-bounce (Bartels type) monochromator at a fixed energy of $E_{\mathrm{ph}} = 8.2\,\mathrm{keV}$. Even when filtering out only a small part of the spectrum, the pulse intensity would still be too high when focused down to a few $100\,\mathrm{nm}$ and destroy our sample with a single pulse. To mitigate radiation damage to the sample silicon filters were used before the optics and the beam intensity was attenuated by 10^{-3} to 10^{-4}.

6.1.4 Summary of Be CRL and phase plate combinations used

This short section provides an overview of combinations of Be CRLs and phase plates that were used in different experiments (cf. Table 6.1). In each of these experiments a new lens stack was used that consists of lenses from two different production runs (cf. Table 5.1). As these lenses are indistinguishable the stack is randomly composed of lenses from these batches. In order to judge the quality of the aberration correction by using the phase plate a measurement with and without the phase plate was done. However, at the LCLS the measurement without phase plate was not carried out for the fixed mounted phase plate due to experimental constraints.

				Performed Measurements			
	Lens	Phase Plate[b]	PP Position[c]	Ptychography		Ronchi Test	
Facility	Composition[a]	(PP)	z_{l-p}	w/o PP	w/ PP	w/o PP	w/ PP
DLS (I13-1)	#1 + #2	1	16 mm	•	•	•	•
PETRA III (P06)	#1 + #2	2	0 mm	•	•	•	•
LCLS (MEC)	(#1 + #2)[d]	1	16 mm	•	•	•	•
	(#1 + #2)[d]	2	0 mm		•		•

[a] compare Table 5.1 for details
[b] see Figure 5.11 for phase plate shapes
[c] geometry as in Figure 6.1
[d] lenses were hand sorted with an optical microscope, excluding ones with visible particles

Table 6.1: Overview of experiments and optical setups used. The lens stack of $N = 20$ Be lenses was assembled for each experiment individually. Thus, all lens stacks differ from one another and lenses were randomly selected from batches "#1" and "#2".

6.2 Phase Unwrapping

When trying to determine aberrations of the given optical element we investigated the phase distribution near the lens exit compared to a spherical wave. Often these phase differences are larger then 2π and therefore need special treatment. This is necessary since the phase is mathematically limited to the interval $(-\pi, \pi]$, which corresponds to the principal value of the arctangent function. Hence, a fast two-dimensional phase-unwrapping algorithm [Her+02] was used in order to show phase errors $> 2\pi$. The algorithm is quality guided and follows a non-continuous path, preventing error propagation. To illustrate encountered problems the phase difference between two nearly identical measurement is shown for the algorithm used in this work and the previously implemented global algorithm based on fast-Fourier transforms in Figure 6.2. Most serious differences between these two algorithms can be seen on the edges of the field-of-view. During processing a cut-off was enforced on the phase maps that is based on intensity I. Phases were set to zero if the intensity was below $0.02\, I_{\max}$ for the global method. For the quality guided method these areas were masked, so that the algorithm would not process these regions. It is clearly visible that these discontinuities at the edges propagate into the relevant area in the case of the global algorithm in Figure 6.2(b). Smaller phase irregularities, originating from dust particles or other errors of the lens inside the field-of-view, are highlighted by the upper dashed pair of circles. Also non-connected areas do not interfere with each other in the case of the non-continuous path algorithm

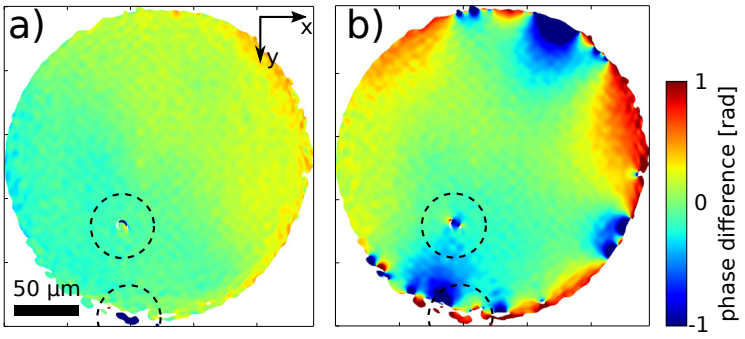

Figure 6.2: Comparison of phase-unwrap algorithms. Difference in the reconstructed phases of two nearly identical measurements when using (a) a quality guided non-continuous path algorithm [Her+02] and (b) a global fast-Fourier based algorithm. In addition to the significant differences at the border of the field-of-view, smaller features are highlighted by dashed circles.

(lower circles in Figure 6.2). In general a global algorithm is not suited to unwrap phases in a localized area, surrounded by ill phase information.

6.3 Repeatability of Phase Error Determination

During the description of the phase plate design and manufacturing in Section 5.3 the observation was made that the magnitude of the measured phase errors varied quite a lot between various measurements. Here, we want to confirm that individual measurements are reproducible within a certain error margin. This is very important to confirm that ptychographic reconstructions and the subsequent propagation to a plane near the lens exit actually delivers reliable results on phase errors. It will also give a sense on how to interpret the measured data for the aberration corrected case.

The measurements for repeatability were carried out at the MEC instrument of the LCLS within the same conditions as previously described in Section 6.1. This environment is especially challenging when trying to compare distinct measurements with each other since the reconstruction of the wave field may suffer from strong beam fluctuation of the XFEL beam. However, it has been shown that the pointing stability of an XFEL may be poor, but the phase front seems to be very stable when only considering full hits of the optics aperture [Sch+13]. That said, we filtered all data taken at the LCLS to only use diffraction patterns with highest overall intensity. This will automatically discard diffraction pattern where the aperture was only partially illuminated, enforcing good pointing stability and reproducible phase distributions of the incoming laser beam.

The reconstructed object phase shift and the probe function for two consecutive measurements are shown in Figure 6.3. The algorithm converged well in both cases. The test object was made of $1\,\mu\mathrm{m}$ thick tungsten and the reconstructed phase shift of $1.8\,\mathrm{rad}$ is in good agreement with the theoretical value of $1.85\,\mathrm{rad}$. Both objects show identical defect features on the spokes of the siemens stars. Also the reconstructed illuminations shown in Figure 6.3(b),(d) appear nearly identical. In order to better reveal small differences the reconstructed wave field was propagated back at the lens exit by a distance z_{p-s} to a position where later on the corrective phase plate was positioned (cf. Figure 6.1). The corresponding phase differences to a spherical wave and the phase difference between these two measurements are

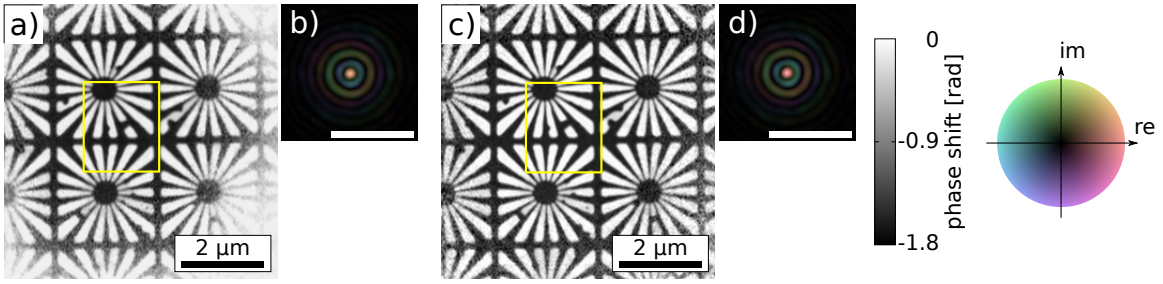

Figure 6.3: Comparison of two consecutive measurements and their ptychographic reconstructions. The respective object phase shift is shown in (a) and (c). The magnitude of the phase shift encoded by hue is given by the color bar. The yellow rectangle denotes the scanned area. The reconstructed probe functions are shown in (b) and (d), respectively. The white scale bar represents $2\,\mu\mathrm{m}$, thus all images are equally scaled. The amplitude and phase in (b) and (d) are encoded by hue and color as stated by the color wheel.

depicted in Figure 6.4. Again, both phase differences to a spherical wave shown in Figure 6.4(a),(b) are in good agreement, besides a small phase offset. Also small features, as indicated by the dotted circle, are represented very accurately in both cases. This is proven by the difference of the two measurements in Figure 6.4(c). The small feature inside the dotted circle vanishes completely. Instead, a small phase wedge becomes visible. When we correct for this wedge the standard deviation of the phase is $\sigma = 0.041\,\mathrm{rad}$ in this case.

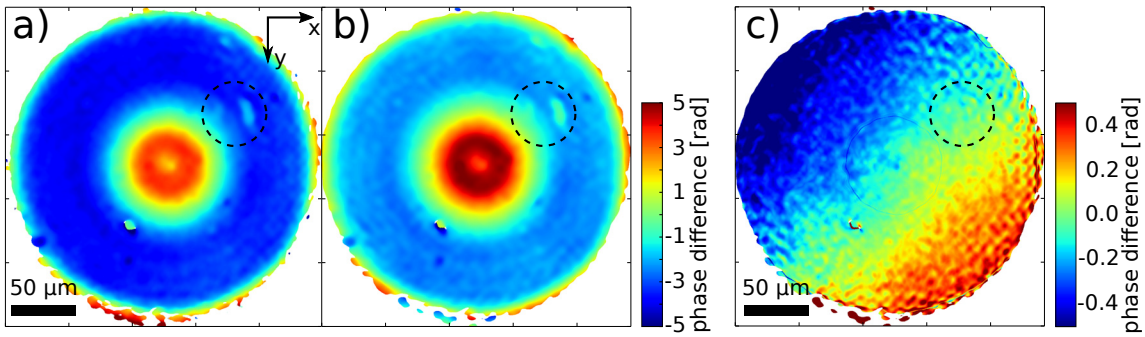

Figure 6.4: The phase differences compared to an ideal spherical wave near the lens exit corresponding to the ptychographic reconstructions in Figure 6.3 are shown in (a) and (b). Phases are offset to each other. The phase difference between (a) and (b) is shown in subfigure (c) on a different scale indicated on the right. A distinct lens feature is highlighted by the dashed circle.

The same procedure was also undertaken with the phase plate installed after the lens. The individual reconstructions are omitted here. Instead, only the back propagated wave field and its difference to a spherical wave is shown in Figure 6.5(a),(b) together with the phase difference between these two measurements (Figure 6.5(c)). Due to the phase offset the colors do not match perfectly in Figure 6.5(a),(b), but the overall shape and small features are present in both images. Indeed, the phase difference presented in Figure 6.5(c) shows nearly no visible signs of features from Figure 6.5(a),(b). This is highlighted by the prominent feature marked by the dashed circle. The previously discovered phase wedge is also present here. When correcting for it the measured phase deviation is determined to $\sigma = 0.043\,\mathrm{rad}$.
Both evaluations showed a small phase wedge when comparing consecutive measurements. In between measurements the complete setup was left unchanged. Successive measurements were carried out within

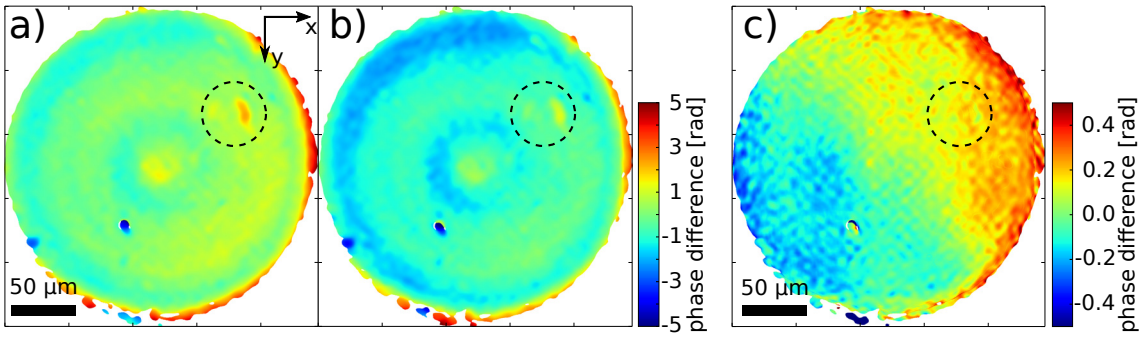

Figure 6.5: The phase differences compared to an ideal spherical wave after the phase plate are shown in (a) and (b). Phases are offset to each other. The phase difference between (a) and (b) is shown in subfigure (c) on a different scale indicated on the right. A distinct lens feature is highlighted by the dashed circle.

half an hour. Handling of the diffraction patterns (dark-field correction, cropping, and intensity sorting) was performed equally and also parameters for the ptychographic reconstruction were kept constant. Subsequent propagation and subtraction of a perfect spherical wave were also carried out the same way. In both cases the phase wedge is approximately $0.8\,\mathrm{rad}$ over a wave-field extent of $200\,\mu\mathrm{m}$. With a wavelength of $\lambda = 1.51\,\text{Å}$ this equals to an angle of $0.6\,\mu\mathrm{rad}$. A general reason for a phase wedge in the ptychographic reconstruction is often a mismatch of the optical axis and the center of the diffraction pattern due to cropping errors. Here, this wedge would correspond to a shift of the diffraction patterns of $3\,\mu\mathrm{m}$ on the detector placed $5\,\mathrm{m}$ behind the sample, which is very small compared to the detector pixel size in this case of $110\,\mu\mathrm{m}$ (CSPAD-140k [Her+13]). Hence, the shift is not caused by processing errors when handling diffraction patterns since only integer pixel steps are possible. Small thermal drifts in the experimental setup, e. g. of the detector or the lens mount, could also cause this phase wedge. The fact that such small drifts of a few micrometer can be detected demonstrates the high sensitivity of the technique. A mean standard deviation of phase errors of $\sigma_{\mathrm{mean}} = 0.042\,\mathrm{rad}$ at $E_{\mathrm{ph}} = 8.2\,\mathrm{keV}$ corresponds to a Be thickness of $200\,\mathrm{nm}$ (equals $5\,\mathrm{nm}$ per lens surface in a stack of $N = 20$ lenses) and a fused quartz (SiO_2, $\rho = 2.2\,\mathrm{g\,cm^{-3}}$) thickness of $150\,\mathrm{nm}$. This illustrates the quality of the optics characterization with the help of ptychography. With these data the uncertainty of initial Be lens surface deviations presented in Figure 5.7 can be stated with $\sigma = 5\,\mathrm{nm}$, which is equal to a phase plate surface shape uncertainty of $\sigma = 150\,\mathrm{nm}$ (cf. Figure 5.11).

6.4 Correcting Spherical Aberrations with a Phase Plate

In this section the focusing properties of an uncorrected set of Be CRLs are compared to the same set of lenses, but equipped with the newly developed phase plate in place. The whole evaluation is presented on selected data only. Results from all three facilities will be presented together in several comprehensive figures.

The nominal properties of a stack of $N = 20$ Be CRLs at the photon energy of $E_{\mathrm{ph}} = 8.2\,\mathrm{keV}$ are summarized in Table 6.2. These values assume aberration-free optics. Please note that the specific composition of the CRL stack varied between experiments (cf. Table 6.1). Here, all 20 lenses are treated equal. In reality, however, lenses from two production runs were mixed that may have slightly different

Property	Value (for $E_{\mathrm{ph}} = 8.2\,\mathrm{keV}$)
Number of lenses N	20
Radius of curvature R	$50\,\mu\mathrm{m}$
Lens thickness l	$500\,\mu\mathrm{m}$
Apex thickness d	$33\,\mu\mathrm{m}$
Geometric aperture $2R_0 = D$	$300\,\mu\mathrm{m}$
Lens casing width l_c	$1.1\,\mathrm{mm}$
Numerical aperture NA	4.94×10^{-4}
Focal length f	$250\,\mathrm{mm}$
Effective aperture D_{eff}	$249\,\mu\mathrm{m}$
Transmission T	0.44
Diffraction limited spot size d_{t}	$115\,\mathrm{nm}$

Table 6.2: Theoretical properties of the Be CRL lens stack during all conducted experiments assuming a perfect lens shape. However, the composition of the 20 single lenses varied between experiments (cf. Table 6.1). All lens parameters are explained in Chapter 4. See especially Figure 4.1 for geometric details.

properties as already indicated in Section 5.3.1.

The samples used in all following experiments were fabricated by the group of Ulrich Vogt at KTH Royal Institute of Technology in the Albanova Nanofabrication Facility with the same method used mainly for zone plate fabrication [Uhl+11]. A thick tungsten film ($1\,\mu\mathrm{m}$ to $1.5\,\mu\mathrm{m}$) is sputter-deposited onto a $100\,\mu\mathrm{m}$ thick diamond substrate. Structures from a chromium hardmask are etched into the tungsten layer with a gas mixture of SF_6 and O_2. A scanning electron microscope (SEM) image of the grating used for the Ronchi test and the siemens star test structure for ptychography experiments is shown in Figure 6.6. Both images were taken on a comparable sample from the same production batch as the sample used during experiments. Nevertheless they illustrate the manufacturing quality, showing edge roughness on the grating in Figure 6.6(a) and also defects in the siemens star in Figure 6.6(b).

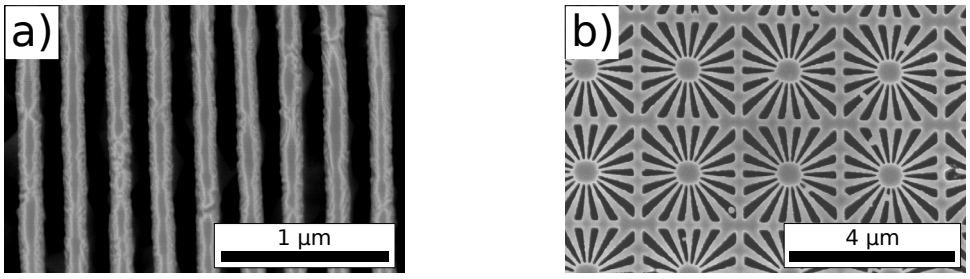

Figure 6.6: SEM images of the utilized grating structures with $270\,\mathrm{nm}$ period (a) and the ptychographic test structure consisting of a siemens star array with $100\,\mathrm{nm}$ smallest features (b). The samples shown here are structured in $1\,\mu\mathrm{m}$ thick tungsten on a $100\,\mu\mathrm{m}$ diamond substrate.

In the following sections characterization experiments using both structures and hence the methods of the Ronchi test and ptychography are presented.

6.4.1 Ronchi Test

As already described earlier in Section 5.1 the Ronchi test is best suited for a quick and qualitative assessment of present aberrations of the optical system [Nil+12] and also to ensure sufficient coherence

properties at the beamline [Uhl+14]. Here, the Ronchi test was also successfully used to align the phase plate with respect to the CRL lens stack on the optical axis with a lateral accuracy $< 5\,\mu\mathrm{m}$. First, a very coarse alignment of the phase plate was carried out by simply centering the phase plate with the help of phase-contrast imaging on a high resolution x-ray camera. The phase plate acts as a sample in the beam path that can be imaged directly onto a 2D detector.

After this initial aligning procedure a Ronchi grating was placed near the focal plane of the CRL stack. The Ronchi sample consisted of horizontal and vertical lines and spaces with varying grating periods. Samples were structured in a $d_1 = 1\,\mu\mathrm{m}$ or $d_2 = 1.5\,\mu\mathrm{m}$ thick tungsten layer placed on a $100\,\mu\mathrm{m}$ thick diamond substrate. At the energy of $E_{\mathrm{ph}} = 8.2\,\mathrm{keV}$ this corresponds to a phase shift of $\Delta\varphi_1 = 1.85\,\mathrm{rad}$ and $\Delta\varphi_2 = 2.78\,\mathrm{rad}$, respectively. Best contrast is achieved if the intensity in the diffraction order $m = 0$ equals $m = \pm 1$, which is the case for $\Delta\varphi \approx 2$ (cf. Equation (5.3)). Here, the given $\Delta\varphi$ yield $(\eta_0 = 0.36, \eta_{\pm 1} = 0.26)$ and $(\eta_0 = 0.03, \eta_{\pm 1} = 0.39)$, respectively. However, these numbers are only valid for a pure phase grating. The transmission T of the utilized gratings is $T_1 = 0.87$ and $T_2 = 0.82$. Nevertheless contrast during experiments was still sufficient when using the first grating. We chose a period of $g = 270\,\mathrm{nm}$ such that diffraction orders overlap approximately by half (cf. Equation (5.1)).

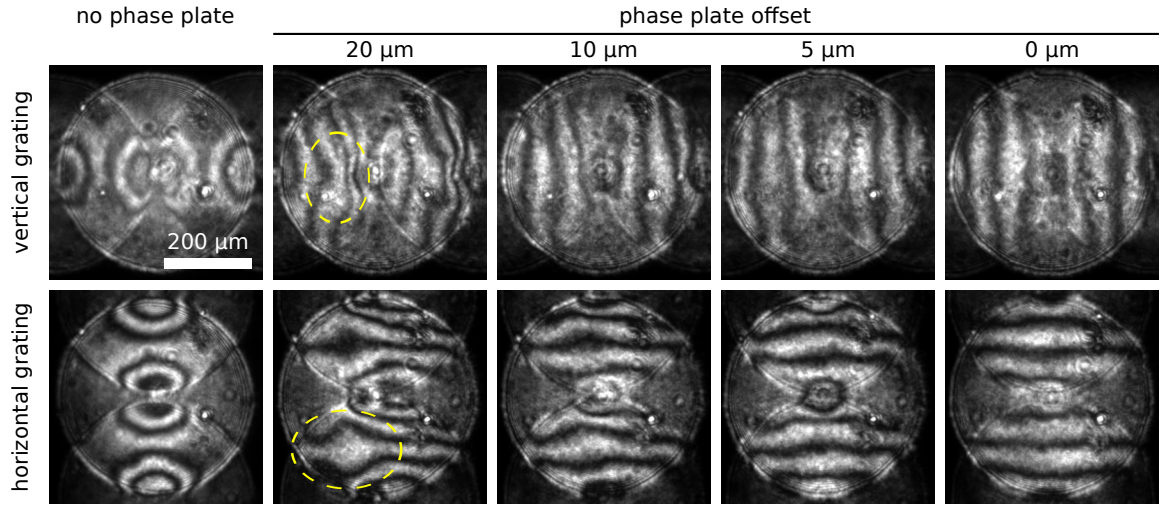

Figure 6.7: Ronchigrams for the vertical and horizontal grating without a phase plate and for various phase plate misalignments in horizontal direction ($20\,\mu\mathrm{m}$ to $0\,\mu\mathrm{m}$). The scale bar indicates the size of the beam on the high resolution x-ray camera. Relevant features used for alignment are highlighted by the dashed lines in first image set of the alignment series. The data was recorded at beamline P06 of PETRA III.

To give a short insight into the alignment process with the help of the Ronchi test several Ronchigrams with a similar count of visible fringes for various alignment positions recorded at beamline P06 at PETRA III are shown in Figure 6.7. In the example the phase plate was misaligned in horizontal direction. One can clearly see the distinct deformation of the fringes highlighted by the dashed lines in the first image set of the alignment procedure. The phase plate was moved in small steps of a few micrometer in order to straighten the interference fringes. For aberration-free optics all lines should appear straight as already shown in Figure 5.2(a). However, this is only true for a perfect grating. Here, the edges of the nanostructured grating are rough (cf. Figure 6.6(a)), sometimes the grating may even suffer from imperfections. Since the grating sample is very large ($20\,\mu\mathrm{m} \times 20\,\mu\mathrm{m}$) compared to the beam

size ($< 2\,\mu\mathrm{m}$), the exact location on the sample is not known. This fact makes a qualitative analysis of the Ronchigrams difficult in the case of very small aberrations where interference fringes may appear slightly distorted due to grid imperfections or aberrations of the optics. These effects are hard to disentangle without a thorough grating characterization and exact knowledge of the beam location. Another aspect, which is visible in the image series of Figure 6.7, is the different fringe contrast between the vertical grating, diffracting the beam horizontally, in the top row and the horizontal grating, deflecting the beam vertically, in the bottom row. This difference is caused by unequal coherence properties for the horizontal and vertical beam direction due to different source sizes at storage ring facilities in horizontal and vertical direction (cf. Section 6.1.2).

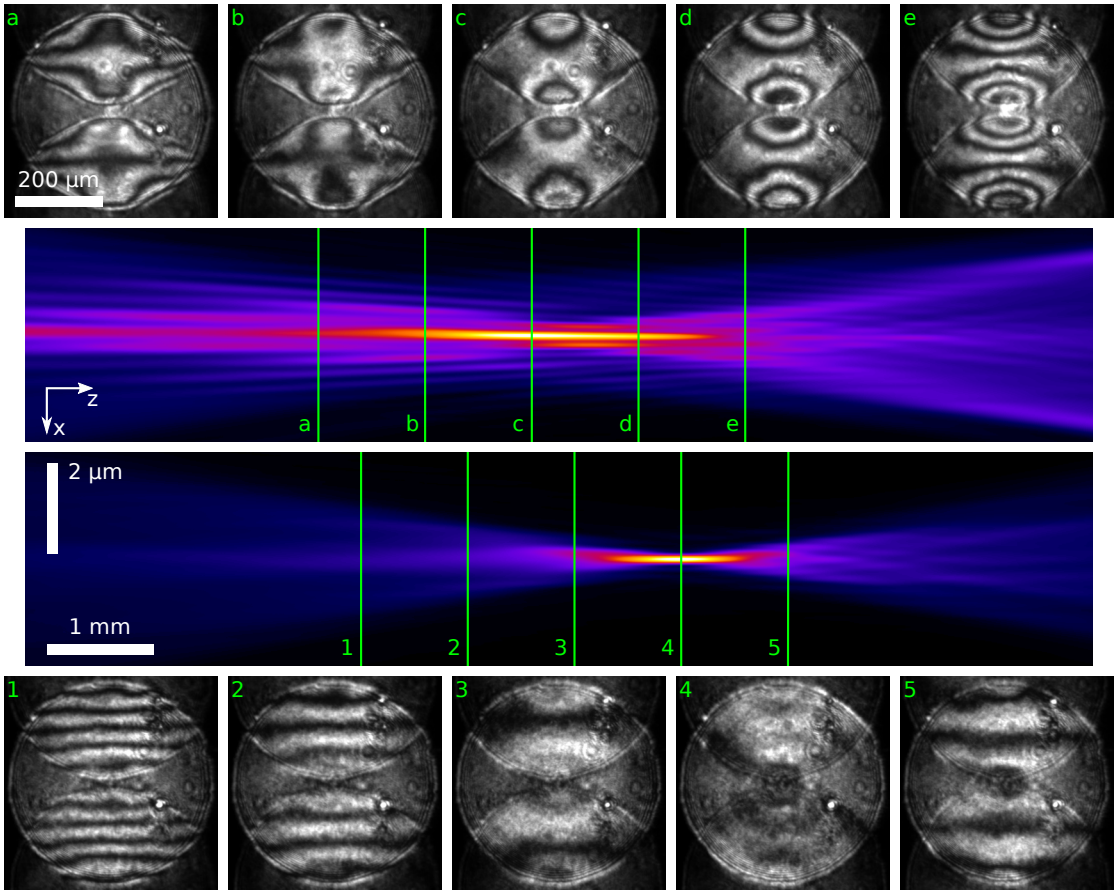

Figure 6.8: Ronchigrams for different positions along the optical axis for both an uncorrected Be CRL stack and the phase-plate corrected one. The exact positions of the gratings are marked by the green lines. Between two Ronchigrams the grating was moved by $1\,\mathrm{mm}$ along the x-ray beam. The reference caustics in the center are taken from ptychographic measurements of the same experiment and are aligned to one another. All data shown was recorded at beamline P06 of PETRA III.

Besides the ability to characterize aberrations qualitatively in a very fast way, the Ronchi test is also especially well suited to locate the focal plane of the optics. The results from such a scan for an uncorrected and corrected lens are shown in Figure 6.8. The caustics as reference for the respective grating plane are taken from ptychographic measurements (cf. Section 6.4.2). If the grating is scanned along the optical axis, the number of visible interference fringes decreases when moving closer to the focal plane since the illuminated grating area shrinks. If the grating period is matched closely to the NA of the optic, only

a black and white area will be visible directly in focus (Figure 6.8 lower Ronchigram “4”). After passing the focal plane the number of visible fringes increases again. This can be clearly seen for the corrected lens in the lower part of Figure 6.8 (Ronchigrams 1-4). Due to spherical aberrations the focal depth in the upper caustic is, however, very large. This is particularly reflected by the Ronchigrams labeled “b” and “c” with almost the same fringe count of two. Not only the intense central region is contributing to the fringe count, but also the weaker outer parts of the illumination.

6.4.2 Ptychography

During all experiments the lens stack was also characterized by ptychography. After locating the focal plane with the help of the Ronchi test an array of small siemens stars (cf. Figure 6.6(b)) was placed in the vicinity of the focal plane. The sample was scanned perpendicular to the beam in a grid-like fashion, recording far-field diffraction patterns at each scan point. From this data the object transmission function as well as the complex illuminating wave field were reconstructed (c.f. Figure 6.3). The complex wave field can now be propagated along the optical axis with the help of the Fresnel-Kirchhoff propagator (cf. Equation (2.18)). With this approach a beam caustic can be created. By propagating the reconstructed two-dimensional wave field (x-y-plane) in small increments of several micrometers along the optical axis (z-axis) a three-dimensional wave field is obtained. When projecting this intensity distribution along the x- or y-axis a beam caustic in the y-z- or x-z-plane is generated, respectively. In these caustics wave-field aberrations are easily identified. However, when wave front errors become small enough these caustics cannot deliver sufficient information. Therefore, the wave field was also propagated back to near the exit of the lens stack to the phase plate position. The phase distribution at this position was compared to the phase of a perfect spherical wave. The radius of curvature for this wave was adjusted to coincide with the distance to the focal plane of the investigated optics. Afterwards the phase error was unwrapped as described earlier in Section 6.2.

A representative example for this evaluation process is shown in Figure 6.9. The central sketch of the setup clarifies the position along the optical axis for the shown phase differences in Figure 6.9(a),(c). They are shown at the phase plate position after the Be CRL. The caustics in Figure 6.9(b),(d) show the intensity of the wave field near the focal plane. The phase error could be reduced from roughly $8\,\mathrm{rad}$ in Figure 6.9(a) to under $2\,\mathrm{rad}$ as shown in Figure 6.9(c). The dramatic effects on the caustic around the focal plane by this correction can be seen in Figure 6.9(b),(d). While the width of the central speckle does not change, the surrounding intensities are drastically reduced, leading to a nearly Gaussian focal spot. Another detail is the overall shift of the focal plane when inserting the phase plate. As indicated by the white lines marking the assumed focal plane, a shift of $0.7\,\mathrm{mm}$ was measured. This would be equivalent to a change in the lens curvature R by less than $0.2\,\mu\mathrm{m}$ and is likely caused by a slight mismatch of the phase plate shape.

One can now also prove the correctness of the reconstructed wave field from ptychography by comparison with the prior recorded Ronchigrams. By using the retrieved wave field at the former position of a Ronchi grating (e. g. positions from Figure 6.8) and with knowledge of the grating parameters (material, thickness, period), one can model Ronchigrams and compare these with the independently measured ones. Exemplary results are shown in Figure 6.10 for a single position of the uncorrected and corrected case. The modeled Ronchigrams and measured fringe patterns match qualitatively very well and even small features due to lens imperfections match closely. Note that the contrast in the modeled

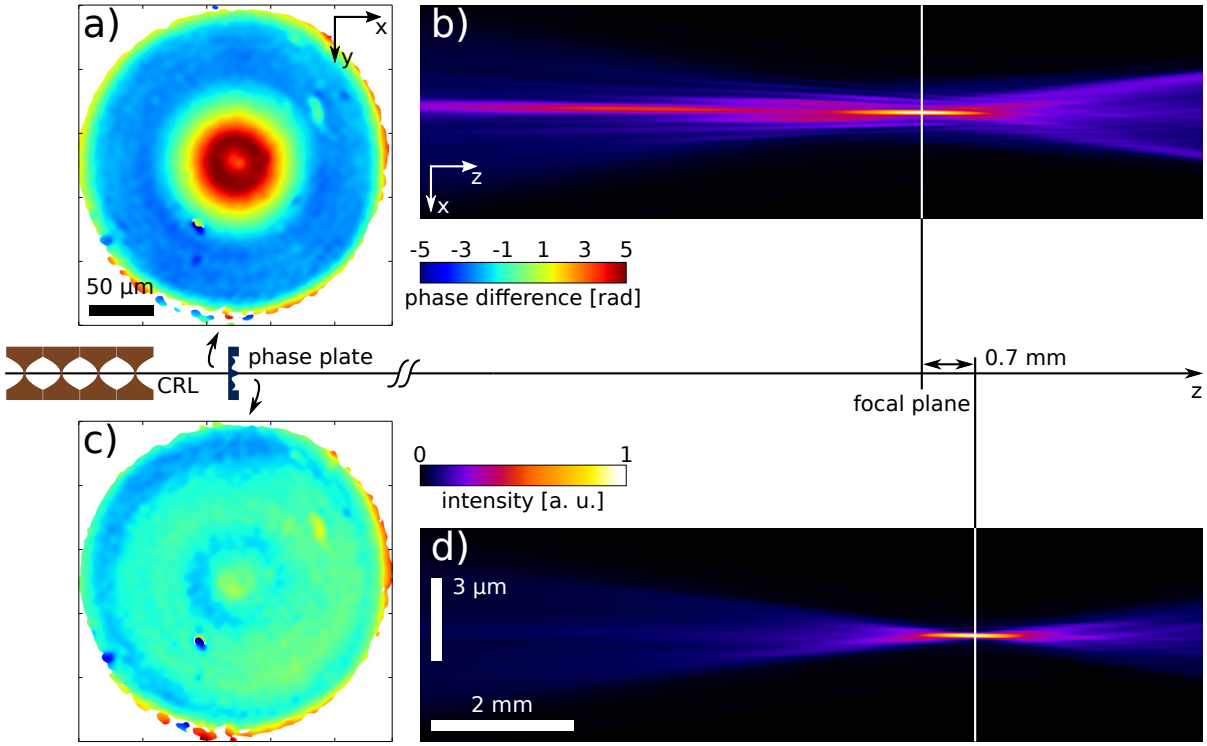

Figure 6.9: Beam characterization for a set of Be CRLs without (a, b) and with (c, d) a phase plate at the LCLS. The phase difference compared to a perfect spherical wave at the eventual position of the phase plate is shown in (a, c) and the corresponding beam caustics in the vicinity of the focal plane are depicted in (b, d), respectively.

Ronchigrams is higher due to perfect coherence assumptions in the calculations. This independent comparison demonstrates that complex wave fields obtained by ptychography are indeed consistent with data acquired by the Ronchi test.

This section should clarify the evaluation process each ptychographic measurement has received. A more quantitative assessment and summary of all measurements will be given in the following section.

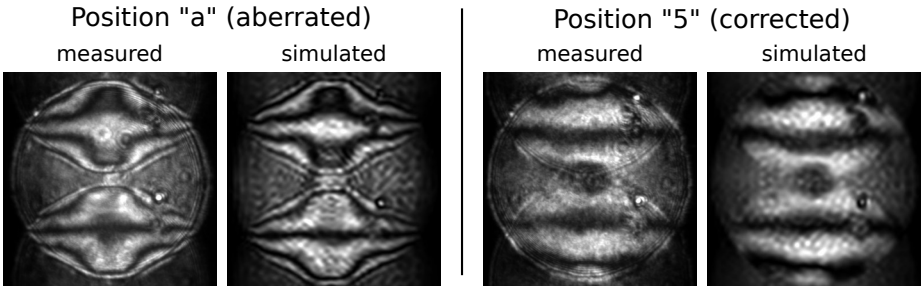

Figure 6.10: Two modeled Ronchigrams from ptychography data compared with measured Ronchigrams. The left side showcases the aberrated lens at position “a” and the right side shows position “5” for the aberration corrected case (positions as shown in Figure 6.8).

6.5 Quantifying Focusing Quality

Until now, the discussion on aberration correction was more focused on showing qualitative results. In the following sections a more quantitative description of the achieved beam properties with the corrective phase plate in comparison with the uncorrected Be CRL stack shall be given.

6.5.1 Focal Spot Characteristics

Focal spot size and magnitude of side lobes are properties of high interest for many applications. While the existence of strong side lobes can be inherent to the optics due to their sharp aperture (e. g. KB-mirrors, FZPs), they are often undesired. Refractive lenses, in theory, have the advantage of a Gaussian aperture due to absorption effects. This leads to an also Gaussian shaped focal spot. However, in the application presented here the Be CRLs have an aperture that resembles more a truncated Gaussian profile. The lens is still very transparent at the outer diameter ($T = 0.17$ for the lens as described in Table 6.2) and, therefore, the Gaussian profile is cut-off. This results in a Gaussian focal spot with considerable side lobes. The horizontal profile of a perfect CRL focus is compared to the experimentally achieved foci of aberrated and corrected CRL optics in Figure 6.11.

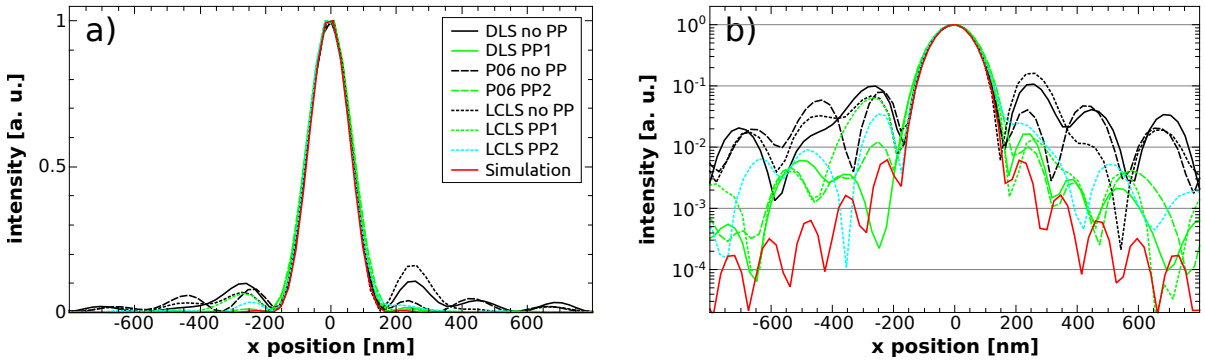

Figure 6.11: Horizontal line profile through focal spot. Normalized intensity is plotted on a linear scale in (a) and logarithmic in (b). Data for the uncorrected lens ins shown in black, the corrected lens is drawn green. A simulation for a perfect lens for reference is plotted in red. Individual beamtimes are encoded by line styles.

First of all the spot size of the central speckle is nearly identical for every measurement and is in very good agreement with the modeled focal spot size of $138\,\mathrm{nm}$ (cf. Figure 6.11(a)). The previously stated analytical value of $115\,\mathrm{nm}$ (cf. Table 6.2) is smaller since we assumed a Gaussian aperture. However, for a circular aperture the Airy disc is described by a Bessel function. Applying a Gaussian profile approximation to the central speckle yields $d_\mathrm{t} \approx 1\lambda/(2NA) = 153\,\mathrm{nm}$ instead of $d_\mathrm{t} \approx 0.75\lambda/(2NA) = 115\,\mathrm{nm}$ for a Gaussian aperture (cf. Section 4.3.3). The Be CRL described here lies in between these two extreme cases. Main improvements related to the phase plate were the intensity reduction in the side lobes by an order of magnitude (cf. Figure 6.11(b)). The first side lobe intensity of the corrected lens is only a factor of two larger than the simulated perfect case.

While overall focus quality could be investigated by these normalized profiles, another interesting value that is closely related to side lobe intensity is the achieved peak focal-intensity. This number is maximized for a perfect optical system that shows the smallest amount of side lobes while also being highly transparent. However, the peak focal-intensity is often reduced due to aberrations. By adding a phase

plate to the systems these aberrations can be corrected for and side lobes are reduced, leading to an increased peak focal-intensity. The crux of the phase plate in this regard is the added absorption to the optical system due to the phase plate substrate material. In the worst case the phase plate would perfectly correct aberrations, but the added attenuation of the beam can, nevertheless, lead to the same or even a reduced peak focal-intensity. Since one of the main applications for the optics will be the creation and diagnosis of plasmas and warm dense matter at XFELs, the peak intensity is a crucial value. However, determination of this value in the reconstructed images is difficult. Due to the finite pixel size in the reconstructions the peak value can be decreased when the position of the pixel does not lie in the exact center of the central lobe. While different pixel sizes between reconstructions can be accounted for, this alignment problem is not easily solvable. Fortunately, the relative peak intensity and the relative intensity in the central lobe of aberrated optics compared to ideal ones are nearly the same here as simulations have shown. A summary of measured and simulated intensities is given in Figure 6.12.

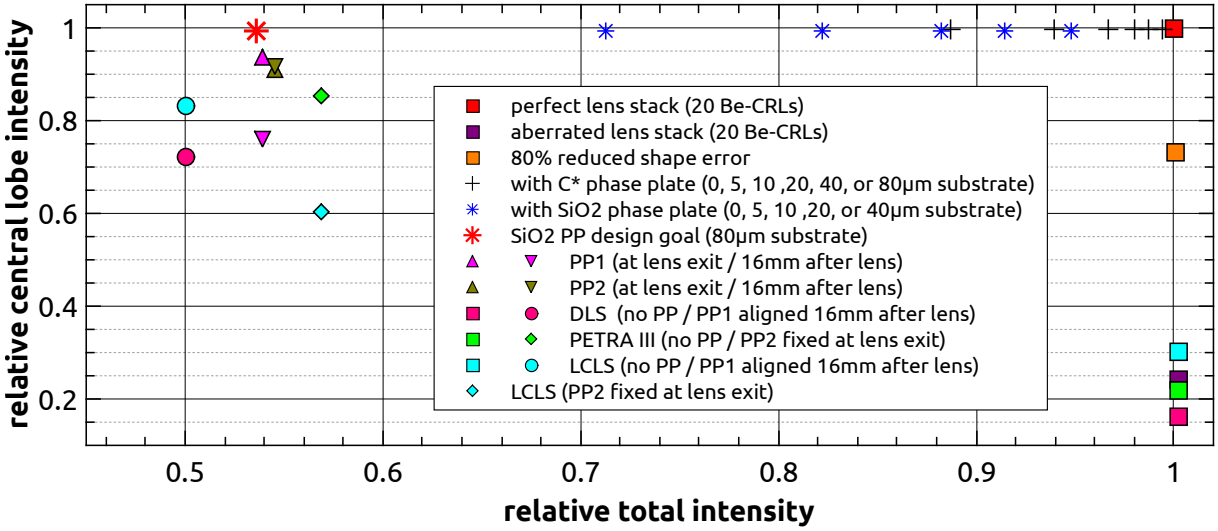

Figure 6.12: Relative total and central lobe intensity in focus of investigated optics compared to a perfect lens stack. Optics without any corrective phase plate are plotted by colored squares. Achievable intensities for a corrected stack for both diamond and fused silica phase plates are marked by crosses and stars, respectively. Simulations with the measured phase plate profiles (cf. Figure 5.11) and a simulated lens are indicated by triangles. Experimentally achieved intensities are marked by circles and a diamond.

First, all data points are compared to a perfect lens stack marked by the red square. This lens has a relative transmission of one and also the maximum achievable central lobe intensity in focus. The aberrated lens system has nearly the same total intensity, but due to strong side lobes the central lobe intensity is decreased considerably down to $24\,\%$ compared to perfect optics. The purple square indicates the initial measurement in 2012 that was used to design the corrective phase plate. One can see that recent measurements at PETRA III (green square) agree well. However, the measurement at the LCLS (cyan square) shows a higher central lobe intensity that is likely caused by a careful sorting of lenses before the experiment (cf. Section 5.3.1 and Figure 5.6), while the data from DLS (pink square) show a reduced performance. Adding a phase plate to the pure CRL stack corrects wave front errors but also increases attenuation. Even if the additional substrate thickness equals zero the phase plate contributes considerably to beam attenuation, depending on the material chosen (black crosses and blue stars in

Figure 6.12 for diamond and fused silica, respectively). The raw material used to structure the phase plate in was roughly $120\,\mu\mathrm{m}$ thick fused silica as subsequent measurements showed. This equals a remaining substrate thickness of $\approx 80\,\mu\mathrm{m}$ after the structuring process. The expected performance when using such a phase plate is marked by the red star in Figure 6.12. After structuring the phase plate the surface profile was measured by a laser scanning microscope (LSM) as shown in Figure 5.11. Using these profiles simulations were carried out with initial results from 2012 (purple square). Depending on the lateral position of the phase plate results can vary (cf. Figure 5.12). Here, the phase plate was positioned perfectly on the optical axis. However, the position along the optical axis was changed. While the position at the lens exit (triangle pointing upwards) corresponds to the initially designed one, the alternative position $16\,\mathrm{mm}$ further downstream (triangle pointing downwards) was also simulated since the phase plate was positioned there very often in the actual experiments. For both phase plates the position directly after the lens shows good results, as measured phase plate shapes are very close to the ideal one (cf. Figure 5.11). However, phase plate 1 shows a significant drop in central lobe intensity when positioned further downstream, which is not the case for phase plate 2. An explanation might be the relatively flat structured ring region around the central cone (cf. Figure 5.11). These four points give a rough estimation of what can be expected from the phase plates if aligned very well. The measured data for different beamlines with the phase plate positioned approximately $16\,\mathrm{mm}$ downstream of the lens exit is denoted by colored circles. The LCLS data for phase plate 1 (cyan circle) lies in between the simulation (magenta triangles). The data at DLS (pink circle) is slightly below, but it has to be noted that the aberrated lens at DLS (pink square) was not performing very well and showed the strongest aberrations. In all of these measurements the phase plate was aligned with the help of the Ronchi method. Measurements with a fixed installation of the phase plate into the lens stack are marked by diamonds (green at PETRA III and cyan at the LCLS). The results at PETRA III show an exceptionally good agreement with simulations and theoretical data. In fact this setup performed best. Here, a lot of care was taken to align the lenses with the fixed phase plate. After initial lens alignment with a high resolution x-ray camera a ptychogram was recorded and evaluated. By slightly tilting the whole lens stack with the mounted phase plate small corrections in the micrometer range could be made to the phase plate position. After only one iteration of the lens stack tilt the phase plate position was readjusted to an accuracy better than $5\,\mu\mathrm{m}$ on the optical axis, resulting in very good performance. On the other hand the data taken at the LCLS (cyan diamond) showcase a situation were alignment was not carried out very well and further refinement steps were skipped. The performance is inferior compared to all other cases. Here, one reason is for sure the slight off-center position of the phase plate in the casing that was not corrected for by slightly tilting the lens stack. Another unknown reason might also be different initial aberrations in the lens stack. Again, the lenses were presorted for this beamtime. Unfortunately this lens stack was not characterized without a phase plate, which makes the initial aberrations inaccessible.

Despite the good performance in central lobe intensity the phase plates showed significant deviations in total transmission. Unfortunately, the data are not complete and a transmission measurement with a diode was not carried out during all experiments. Instead, the integrated counts on the two-dimensional pixel detectors were used. This could only be done at DLS and PETRA III, since the beam at the LCLS fluctuates too much. At DLS the measurements are influenced by an additional filter in the beamline that was changed in between ptychography scans. Data and results are summarized in Table 6.3. While it is shown that a different placement of the phase plate along the beam causes no significant change

	Integrated counts [s^{-1}]		Filter transmission		Phase plate	
	w/o PP	w/ PP	w/o PP	w/ PP	trans.	thickness[a]
PP1 @DLS	5.513×10^6	1.937×10^7	0.141[b]	1	**0.499**	**98.5 µm**
theory (16 mm behind)					0.539	86.7 µm
theory (lens exit)					0.539	86.7 µm
PP2 @PETRA III	3.331×10^7	1.895×10^7	1	1	**0.569**	**79.1 µm**
theory (16 mm behind)					0.545	85.1 µm
theory (lens exit)					0.545	85.1 µm

[a] mean thickness with assumed Al_2O_3 absorption coefficient $\mu = 71.32\,\mathrm{cm}^{-1}$

[b] a 11.65 µm thick Cr filter was used to reduce photon flux

Table 6.3: The measured integrated intensity during experiments is used to calculate the total transmission and mean thickness of the phase plates. The experimental values are compared to theoretical results for two different phase plate positions.

in the total transmission (though there are small changes since the beam converges from the lens exit until 16 mm downstream), the two individual measurements show a clear deviation from theoretical numbers. The measurement at PETRA III shows a slightly more transparent phase plate. This could be explained by structuring the phase plate deeper into the substrate. The data gathered after fabrication by an LSM (cf. Figure 5.11) can only provide measurements relative to the sample surface. More remarkable is the data from DLS. Here the phase plate seems to be very absorbing. One reason could be the filter used in this case. However, the filter transmission was determined afterwards at the same photon energy and is very accurate. Since all detectors were only exposed to photon flux rates well below their counting capabilities in a linear regime, this error source can be excluded. The phase plates were fabricated out of three individual material samples with a nominal stated substrate thickness of 100 µm. The manufacturer states a tolerance for these samples of ±25 µm. Unfortunately, no thickness measurements were carried out before producing these phase plates. On an unused substrate sample the thickness could be determined afterwards to (118 ± 2) µm. For the substrates used the initial thickness remains unknown. One explanation might be a substrate thickness slightly above specification of 130 µm. Due to missing data this is rather speculative.

When neglecting these uncertainties in absolute substrate thickness the measured data points in Figure 6.12 (colored circles and diamonds) might be shifted horizontally. One can see that the performance was best for the combination used at PETRA III (green diamond). The initial aberrations (green square) are closest to the assumed one (purple square) so that the structured phase plate fits best in this case. In general it is crucial to match the phase plate exactly to the optics. It has been shown that performance can vary significantly for different combinations of the 20 Be lenses. However, the most important factor is the lateral alignment of the phase plate, as data for the fixed phase plate 2 at the LCLS (cyan diamond) has shown.

6.5.2 Zernike Amplitudes

The evaluation of aberrations is often done using Zernike polynomials. The corresponding Zernike coefficients are a quantitative measure of the strength of an aberration. Here, the Zernike coefficients are determined by fitting Zernike polynomials to the phase errors at the lens exit obtained by ptychography

(cf. Section 6.4.2). For a meaningful fit the region was chosen to be concentric with the recovered phase difference at the lens exit. An example of this procedure using the first 37 Zernike polynomials is shown in Figure 6.13.

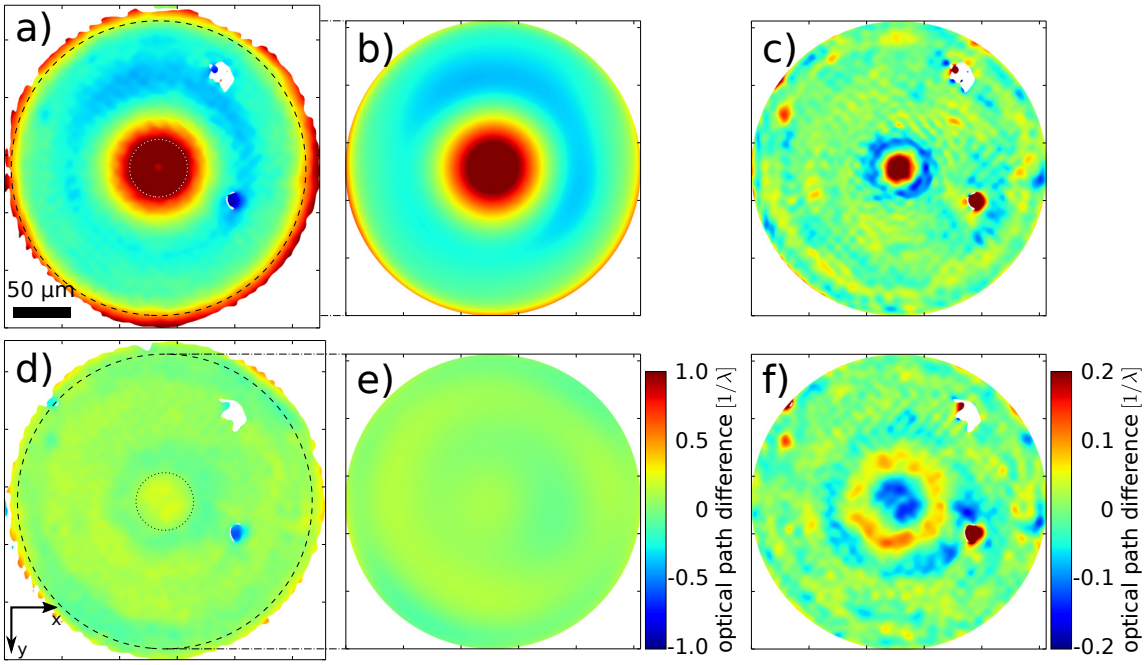

Figure 6.13: Fit of the first 37 Zernike polynomials to phase errors obtained by ptychography. The initial optical path difference from ptychography together with the fitting region marked by the dashed outer circle (inner concentric dotted circle for reference only) is shown in (a) and (d) for the aberrated and corrected optics, respectively. In each case the Zernike fit is depicted in (b) and (e). The difference between the initial data and the Zernike fit is shown in (c) and (f) on a different color bar scale.

The fitting region is marked by the outer dashed circle. The inner dotted circle is concentric and serves as a second reference for alignment. As discussed earlier the resulting optical path difference from the Zernike polynomials can represent the results from ptychography only on small spatial frequencies very well. Higher fluctuating phase errors due to surface roughness cannot be taken into account. This is demonstrated by the fit error shown in Figure 6.13(c),(f). In addition one can see that the fit has its largest error in the central region. Eventually these errors can be reduced by taking even higher Zernike polynomial orders into account. It should be noted that we started to perform fits with the first 22 Zernike polynomials up to Z_6^0. In this case the error maps showed larger errors and missing higher order spherical aberrations were evident. After increasing the number of polynomials to 37, taking the next higher order spherical aberration Z_8^0 into account, fit quality improved considerably. Going up to 56 polynomials (Z_{10}^0) did not lead to significant improvements, though.

The method provides a good assessment of dominant aberration types and can give a quantitative measure of present aberrations. A summary of Zernike amplitudes for all measurements is given in Figure 6.14. The piston aberration Z_0 only controls the global phase offset during fitting. Therefore, the corresponding coefficient is not plotted or used in further considerations. The total sum Σ displayed in the legend of the graphs in Figure 6.14 was calculated over the modulus of coefficients $c_\nu^{\pm\mu}$, excluding c_0. These sums represent the total strength of all present aberrations. Values are in very good agreement with previous

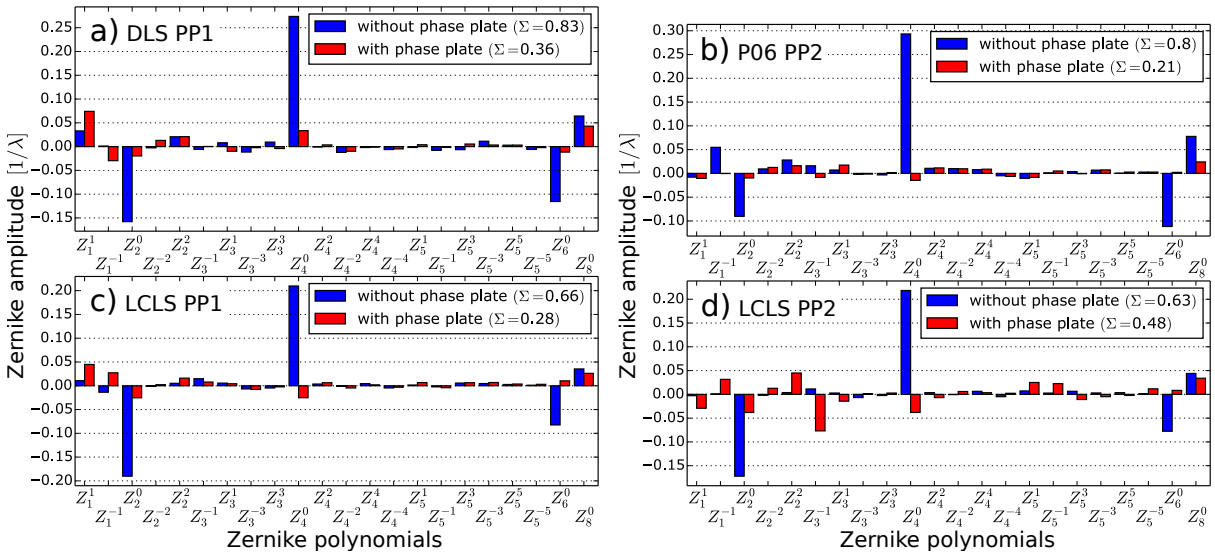

Figure 6.14: Amplitudes for selected Zernike polynomials after fitting. Close to zero amplitudes between Z_6^1 and Z_7^{-7} are not shown. The sum Σ was calculated over the modulus of all coefficients $c_\nu^{\pm\mu}$, excluding only c_0. In (a), (b), and (c) results for aligned phase plates are shown. (d) shows the result at the LCLS for a fixed phase plate.

observations for the central lobe intensity shown in Figure 6.12. For example, the uncorrected lens in Figure 6.14(a),(b) shows stronger aberrations than the LCLS lens in Figure 6.14(c),(d). This is equivalent with the lower central lobe intensity for the DLS and PETRA III lenses as compared to the LCLS lens in Figure 6.12 (pink, green, and cyan square). Also the fixed mounted phase plate in Figure 6.14(d) shows the strongest remaining aberrations of all measurements with phase plate installed. This agrees with the discussed relative central lobe intensity in Figure 6.12 (cyan diamond) which is also the lowest in this case.

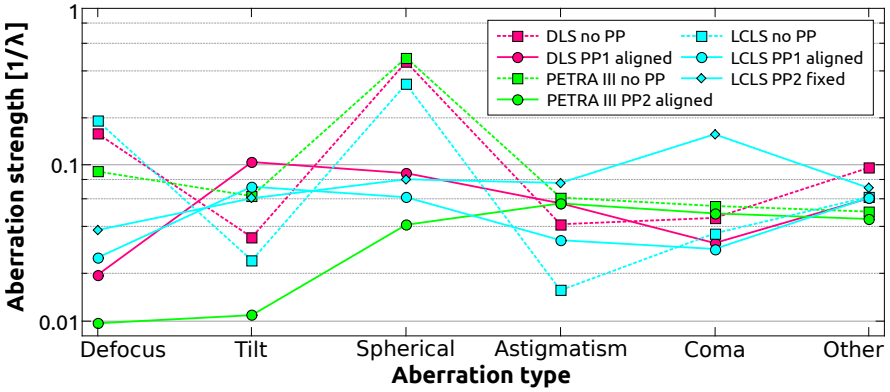

Figure 6.15: Sum of absolute Zernike coefficients grouped into aberration types. Uncorrected optics are represented by dotted lines and squares. Corrected optics by solid lines and circles or diamonds. The group "Other" sums up all higher angular frequency aberrations $|\mu| \geq 3$ such as Trefoil, Pentafoil, and so on. All 36 coefficients from c_1^1 to c_8^0 are considered.

To display certain types of aberrations and the influence of the phase plates in more details, the summation of absolute coefficients grouped by aberration type is shown in Figure 6.15. The most dominant spherical aberration could be significantly reduced with the use of a phase plate in all measurements. The same can be stated for the defocus coefficient. Even though the defocus strength is not directly an

aberration, these wave-field deformations are necessary to describe the data if assuming focal planes like indicated in Figure 6.9. Astigmatism and other coefficients show rather an erratic behavior. In some cases these aberrations are enhanced by the phase plate, in others they are reduced. Here, the data is not sufficient to draw any conclusions. While coma is not affected by the phase plate in general, strong coma can be induced by a misaligned phase plate (LCLS fixed phase plate 2, cyan diamond). The tilt aberration observed is a systematic effect that is strongly influenced by errors in between measurements. The tilt coefficient error encountered in between consecutive measurements of the same optics is roughly $|c_1^1| + |c_1^{-1}| \approx 0.045\,\lambda^{-1}$ and depends on the experimental setup stability as discussed in Section 6.3. Thus, all data points for this aberration type are not very accurate and should not be taken into account when comparing different optics. On the other hand, tilt aberrations do not reduce image quality. For all other aberration groups these systematic errors are $< 0.016\,\lambda^{-1}$.

6.6 Influence of Beamline Optics

In all the measurements additional beamline optics were used in order to tailor the x-ray beam to specific needs of the setup. These optics are often located at the beginning of the beamline far away from the actual experiment. In addition, the quality of monochromator crystals is often very high. Thus, phase deformations caused by these optics are often neglected when investigating the main optics. In this section a short example from the LCLS is presented, where aberrations induced from prefocusing optics significantly influence beam properties. While the stability of the phase front from pulse to pulse at XFELs is a current research topic, successful ptychographic reconstructions in this work and elsewhere [Sch+13] are strong indicators for a reasonable stable wave front. The setup discussed here is identical to the one described in Section 6.1.3. The only difference is an additional Be CRL set consisting of $N = 7$ single lenses with a curvature $R = 500\,\mu\mathrm{m}$. The lens set was positioned roughly $4\,\mathrm{m}$ in front of the main Be CRL. This prefocusing optics with a nominal focal distance $f = 7\,\mathrm{m}$ was introduced in order to reduce the size of the LCLS beam to the aperture size $D = 300\,\mu\mathrm{m}$ of the main optics. By using this aperture matching technique the photon flux passing through the optics can be maximized. One important aspect to note here is that both optics were not positioned on the same optical axis. The resulting influence on the wave front is shown in Figure 6.16. The reconstructed intensity and phase distribution of the aberrated main CRL is shown in Figure 6.16(a),(d). In the intensity map small grain features can be seen that originate presumably from dust particles on the lenses and eventually inhomogeneities in the lens material itself. When inserting the prefocusing CRL the wave field is converging towards the main CRL. The setup is chosen to match the XFEL intensity distribution closely to the main CRLs aperture. The main CRL is not completely illuminated as can be seen on the right edge in Figure 6.16(b). The dotted circle that represents the main CRLs aperture is added to every image for reference and has always the same size. Another prominent feature seen in Figure 6.16(b) is highlighted by the dashed circle. This darker area represents the apex of the prefocusing lens. The influence on the phase after the main CRL is depicted in Figure 6.16(e) and shows a clear deviation compared to Figure 6.16(d). The phase error induced by the prefocus CRL alone is shown in Figure 6.16(f) by subtracting Figure 6.16(d) from Figure 6.16(e). This reveals a phase error of cylindrical symmetry (highlighted by the concentric dashed circles) and agrees very well with the offset position of the prefocusing CRL. From this limited data one could already come to conclusions about the shape error of the utilized prefocusing CRLs assuming

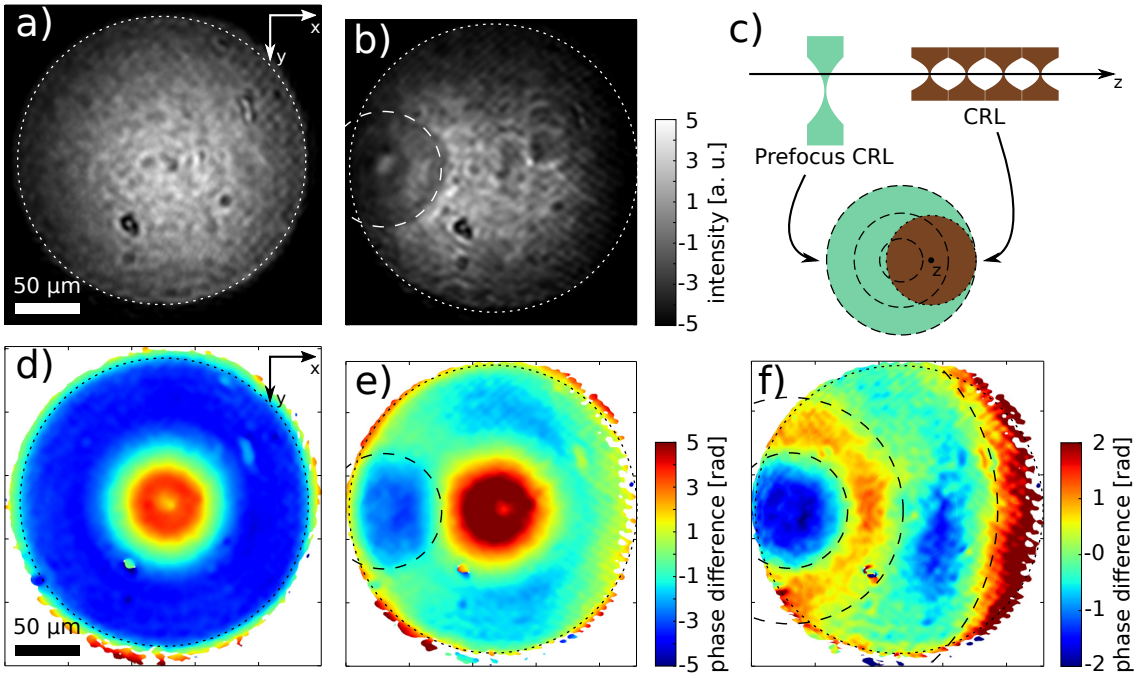

Figure 6.16: Reconstructed intensity and phase distribution at the exit of the main CRL. The stack of $N = 20$ Be CRLs alone is shown in (a) and (d). After inserting a prefocusing CRL stack distinct features of that optics appear in the intensity and phase map in (b) and (e) highlighted by dashed circles. The misalignment of the prefocusing CRL with respect to the main CRL is depicted in (c). The phase difference between (d) and (e) is presented in (f) and shows features originating from the prefocusing CRL alone. The concentric dashed circles representing the prefocusing lens and the dotted circles for the main optics are for reference only.

that the cylindrical symmetry holds. This was not considered in this case. Instead, this example is meant to highlight the influence of beamline optics. These two separate measurements enables us to disentangle imaging effects related to the prefocusing and main lens. Therefore, in order to retrieve qualitative information about specific optics along the beamline, each component has to be characterized individually or in various combinations with each other.

6.7 Phase Shift Consistency

Throughout this chapter the performance of the phase plate in various experiments and on different synchrotron radiation sites has been investigated. Both, phase plate 1 and 2 were used with great success. However, as shown earlier in the manufacturing of these phase plates in Figure 5.11, their shapes were not ideal. In addition it was noted that the phase error of newly arranged lens stacks, especially for the LCLS measurement, was lower than expected (cf. Figure 5.6). Despite these discrepancies the phase plate performance was almost optimal if the time was spent to correctly align the device. One observation made earlier was the small shift of the focal plane of roughly $\Delta z_F \approx 0.7\,\mathrm{mm}$ as shown in Figure 6.9. Here, we want to investigate the relationship between phase plate shape, smaller lens error, and focal plane shift observed in more detail.

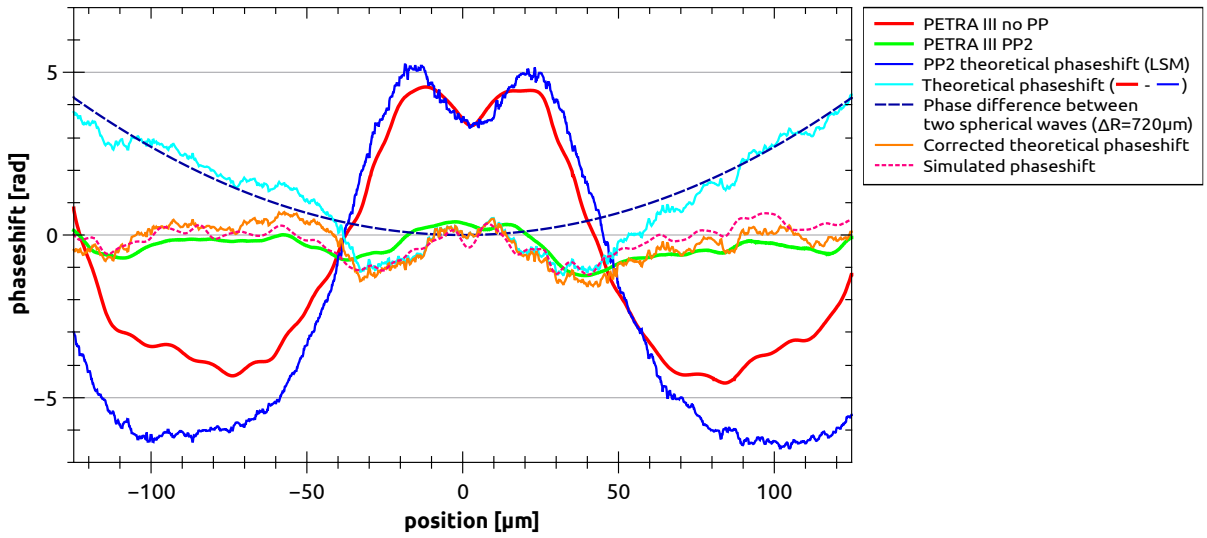

Figure 6.17: Measured phase error at PETRA III without (solid red line) and with (solid green line) phase plate 2. The theoretical phase plate shift (solid blue line) leads to a remaining wave front error (solid cyan line) that does not match the experimental one (solid green line). After introducing an additional phase shift due to a decrease in wave front curvature (dashed dark blue line) the corrected phase error (solid orange line) agrees well with the experiment and simulations (dotted pink line).

Consider Figure 6.17 where the phase error for various situations is plotted. We start from the top of the legend. The solid red line shows the phase error as measured at PETRA III for the uncorrected lens stack obtained by ptychographic wave field reconstruction. The solid blue line on the other hand was calculated from the measured shape profile of the phase plate (LSM data) using a theoretical δ value for SiO_2. Interestingly, the LSM data seem to disagree with the ptychography data and structures appear too deep (as already shown in Figure 5.11). When we use these two phase shifts and subtract them from one another we obtain the remaining theoretical phase error (solid cyan line). This error differs significantly from the experimental results obtained with the installed phase plate (solid green line). However, we observed a shift in the focal plane position. Further modeling revealed a shift of $\Delta z_F = 720\,\mu\mathrm{m}$, which is very close to the experimentally obtained $0.7\,\mathrm{mm}$. Thus, one can consider the shape mismatch of the phase plate also as an effective reduction in phase front curvature. The dashed dark blue line in Figure 6.17 shows the phase difference between two spherical waves of curvature $R_1 = 234.8\,\mathrm{mm}$ and $R_2 = 235.52\,\mathrm{mm}$, leading to $\Delta R = R_2 - R_1 = 720\,\mu\mathrm{m}$. This corresponds to the shift of the focal plane and the additional phase (dashed dark blue line) matches the trend of the theoretical phase shift (solid cyan line). When subtracting this phase shift from the theoretical value we obtain a corrected phase shift with respect to the new wave front curvature (solid orange line). The remaining phase error is in very good agreement with the experimental result with the phase plate installed (solid green line). Also performed simulations on the experimental data without phase plate using the phase plate profile from LSM measurements show a good agreement (dotted pink line) when processed identical to experimental data with the phase plate installed. In order to maximize the overlap between different lines an arbitrary phase offset was added in some cases.

These additional wave-front deviations, related to a mismatch of the focal plane, are encountered often during evaluation. Main reason is the determination of the exact focal plane within the reconstructed beam caustics and hence the wave-front curvature assumed. The focal plane is determined by the plane

with highest intensity in the central speckle. If there is a slight deviation of the focal length from that plane we introduce an additional wave-front curvature. This is represented very clearly by the Zernike polynomials for defocus Z_2^0 in Figure 6.14 and Figure 6.15. The strength of this defocus is highest for the uncorrected cases. Here, the determination of the focal plane by central speckle intensity does not seem to be very accurate. For the corrected cases with a nearly aberration free focus the approach is more suited. The initial characterization measurements in Section 5.3 may also be influenced by the additional wave-front curvature due to defocus. Although the determination of the focal plane was always carried out in the same way by taking the plane with highest peak intensity, slight differences might occur due to the aberrated wave field.
Despite the non-optimal phase-plate shape for the actual lenses used (discrepancy between solid red and blue line in Figure 6.17), wave-front errors were corrected to a minimum. The expected larger deviations due to the shape mismatch could be addressed to a reduction in wave-front curvature, leading to no additional aberrations but to a slightly increased focal length. The results also prove that the structuring of the phase plate was successful and LSM profiles used for monitoring during phase plate fabrication are meaningful. In addition, we did not observe any degradation of the remaining phase plate material related to the high-intensity short-pulse laser interaction with the substrate during fabrication.

6.8 Summary of Results

In order to wrap-up the multitude of results from this chapter key findings are presented concisely.

- During this thesis a phase plate to correct aberrations of refractive x-ray lenses was successfully developed, fabricated, implemented, and their performance thoroughly characterized.
- Performance analysis was carried out by the two methods of ptychography and the Ronchi test. Both techniques are independent from one another and obtained data from them was found to agree very well with each other (cf. Figure 6.10).
- Obtained data can be evaluated not only qualitatively, but quantitative results about the strength and type of various aberrations of the optical system are retrieved in great detail.
- Spherical aberrations in a stack of 20 Be CRLs could be reduced by an order of magnitude when comparing the modulus of relevant Zernike polynomial amplitudes as shown in Figure 6.15.
- The peak intensity in the focal plane was increased from only $25\,\%$ for the uncorrected lens up to $48\,\%$ with the corrective phase plate when compared to the perfect optical system. Main reason for the reduced peak intensity, despite the tremendous reduction in aberration strength, is the relatively high substrate thickness of these first phase plates investigated.
- Neglecting absorption effects in the phase plate a peak focal intensity of $85\,\%$ compared to the perfect optical system was achieved (cf. Figure 6.12), which demonstrates the high fabrication and alignment accuracy reached.
- Perfect alignment of the phase plate with respect to the optical axis is crucial, as can be seen from the spread of results in Figure 6.12.
- To further approach the goal of diffraction limited focusing, meaning a peak intensity in focus $> 95\,\%$ without neglecting phase plate absorption, the shape accuracy of the phase plate has to be improved, substrates made thinner, and, ideally, a more x-ray transparent material like diamond has to be utilized.

7 Nanofocusing with RLLs

In this chapter first experiments carried out with a completely new design of a refractive lens, named by refractive lamellar lens (RLL), are presented. The first experiment was conducted at beamline P06 of PETRA III and uses a compound RLL made of both silicon and aluminum oxide (Figure 7.1(a)). In the second experiment at beamline ID13 of the European Synchrotron Radiation Facility (ESRF) an RLL completely made of Al_2O_3 was used (Figure 7.1(c)). The idea behind the new shape is to fabricate lenses by coating techniques like atomic layer deposition (ALD). With this approach new materials like Al_2O_3 become accessible that have a higher density than silicon while at the same time providing good transmission for x rays due to their low atomic number. The higher density effectively leads to an increased refraction per unit length in the lens stack. Examples of lens prototypes are shown in Figure 7.1. The lamella shape is best visible in Figure 7.1(a), depicting the compound Si-Al_2O_3 RLL. Figure 7.1(b) shows the Si scaffold for the Al_2O_3-only RLL that will be coated by ALD. After coating the Si substrate is removed from the backside. A structure consisting only of a thin Al_2O_3 film remains, forming the actual RLL. All manufacturing steps were carried out at the Institute of Semiconductors and Microsystems (IHM) at TU Dresden. Further details are described in the following sections.

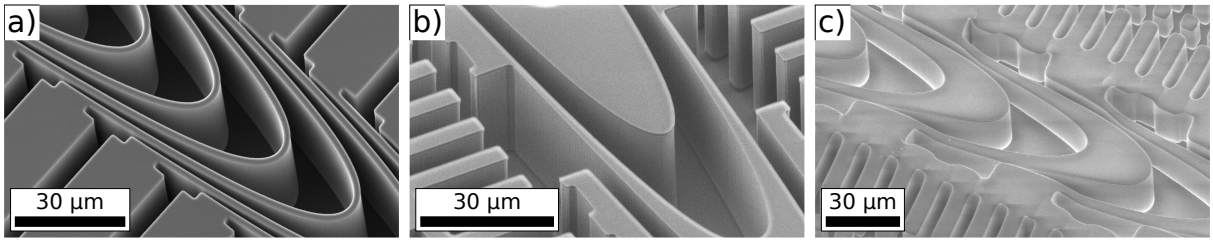

Figure 7.1: SEM images of RLL prototypes. A compound RLL made of Si and Al_2O_3 is shown in (a). (b) shows the Si scaffold that is used to produce the Al_2O_3-only RLL depicted in (c).

7.1 Crossed RLL Geometry

In both experiments RLLs were used in a crossed geometry. Due to the structuring process in silicon a single RLL stack has a cylindrical geometry and can only focus x rays in one direction. Thus, a horizontally and vertically focusing RLL have to be combined in order to create a point focus that can be evaluated by ptychography. The experimental setup is depicted in Figure 7.2. Directly upstream of the lenses guard slits limit the coherent beam to the optics aperture, that is in this case $40\,\mu\mathrm{m} \times 40\,\mu\mathrm{m}$. The confined beam passes the vertical lens first before entering the horizontally focusing lens. Both the vertical and horizontal lens are aligned to each other so that their respective focal planes, given by the focal lengths f_v and f_h, overlap in a common plane. The distance from the exit of the last lens to the common focal plane is called working distance WD.

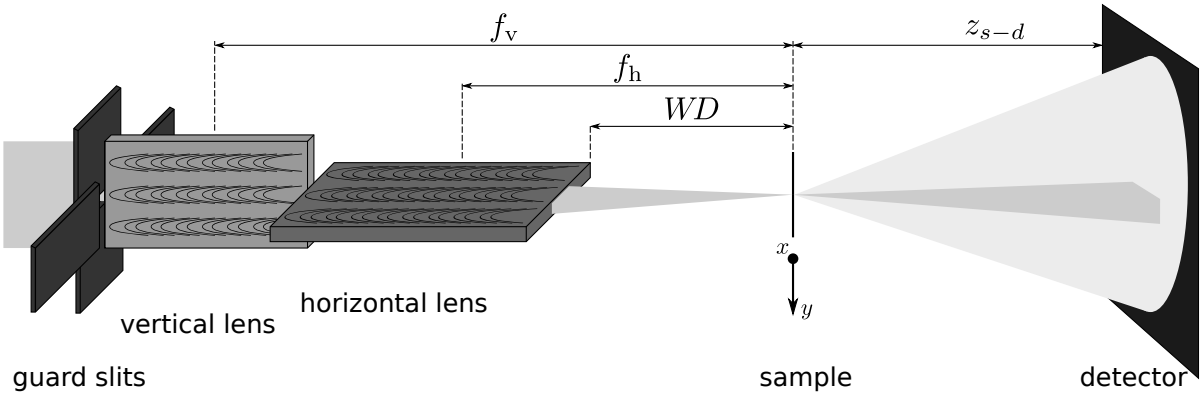

Figure 7.2: Crossed RLL setup sketch. The alignment of both lenses to each other and their focal length f_v and f_h are chosen to overlap in a common plane. The sample is placed in the vicinity of that plane and diffraction patterns are recorded with a two-dimensional detector at distance z_{s-d}.

7.2 Si-Al_2O_3 Compound RLL

The first prototype lens that should demonstrate the successful use of ALD-Al_2O_3 as a lens material was fabricated on a structured Si wafer that not only provides an initial structure for the lens profile, but also acts as a support for the thin aluminum oxide layer. The initial lamellae shape was first structured in a silicon wafer by optical lithography via a chromium hard mask and subsequent deep reactive ion etching. The lamellae are the starting point for the ALD process. Each Si lamella is now coated on all exposed surfaces with a thin Al_2O_3 layer by ALD. The very slow growth rate of these layers allows for a precise thickness control. In theory small etching errors in silicon (over- or underetching the structures) can be compensated this way. A schematic of this process and the resulting lamellae are shown in Figure 7.3.

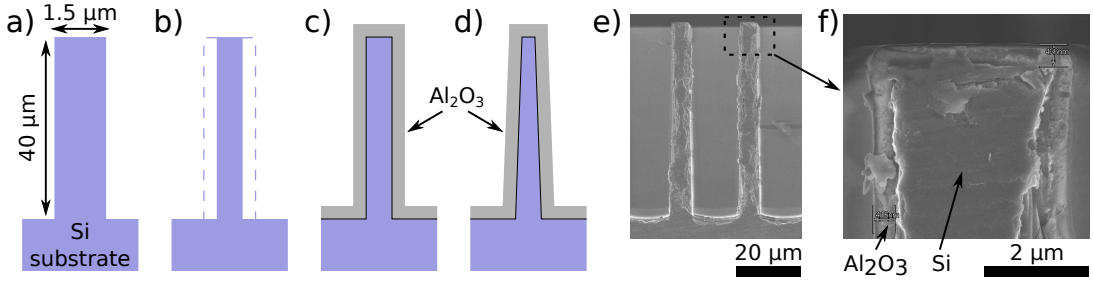

Figure 7.3: (a) - (d) Schematic cross-section along the optical axis z through a single lens lamella at different fabrication stages. (e), (f) SEM images on test lamellae with deposited Al_2O_3 layer. (Sub-figure (a) - (d) reprinted with permission from [Sei+14a]. Copyright 2014, AIP Publishing LLC.)

As discussed in Section 4.2 the lamella shape is dependent on its thickness. Initially, the shape is structured into the Si wafer based on a certain thickness goal (cf. Figure 7.3(a)). The lamella is underetched on purpose (Figure 7.3(b)). This scaffold is then coated with Al_2O_3 to reach the previously designed thickness again (Figure 7.3(c)). In practice, the thickness of the Si lamella is slightly depth dependent due to etching effects (Figure 7.3(d)). This can be seen in the cross-sections through test structures with $4\,\mu\mathrm{m}$ thickness in Figure 7.3(e), (f). The test structure shows a slight depth dependent thickness, that is not critical in this example. In general, the effect increases with reduced lamella thickness. In addition, the

thickness of the deposited Al_2O_3 layer also decreases slightly with increasing depth. These effects sum up to deviations in the lamella thickness over the lens depth in the order of a few $100\,\mathrm{nm}$. This results effectively in deformed parabolas in projection that differ for each depth, introducing aberrations to the beam. Nominal lens parameters are summarized in Table 7.1 for a photon energy of $E_{\mathrm{ph}} = 15.25\,\mathrm{keV}$.

	Lamella properties			Lens properties						
	d_{Si}	d_x	x	N	R	l	D	d_{t}	WD	T
H V	$0.7\,\mu\mathrm{m}$	$0.4\,\mu\mathrm{m}$	Al_2O_3	260 200	$20\,\mu\mathrm{m}$	$25\,\mu\mathrm{m}$	$40\,\mu\mathrm{m}$	$79\,\mathrm{nm}$ $93\,\mathrm{nm}$	$30.1\,\mathrm{mm}$	0.061
H V			Si					$99\,\mathrm{nm}$ $116\,\mathrm{nm}$	$34.7\,\mathrm{mm}$	0.034
H V			C*					$62\,\mathrm{nm}$ $75\,\mathrm{nm}$	$27.7\,\mathrm{mm}$	0.136

Table 7.1: Summary of various lens parameters for the investigated crossed RLL system at a photon energy of $E_{\mathrm{ph}} = 15.25\,\mathrm{keV}$. For comparison two fictive RLL systems, replacing Al_2O_3 by Si or diamond (C*) are shown.

The lens lamellae were designed around a final thickness of $1.5\,\mu\mathrm{m}$. For the creation of the Si scaffold the lamellae were produced with a thickness of $d_{\mathrm{Si}} = 0.7\,\mu\mathrm{m}$. The missing material was added by coating $d_{\mathrm{ALD}} = 0.4\,\mu\mathrm{m}$ thick Al_2O_3 on each side by ALD. The previously mentioned benefit of aluminum oxide as a lens material is highlighted by comparing the compound lens to a pure Si RLL in Table 7.1. Due to the overall lower Z and higher density ρ in the compound lamellae, the transmission T is increased while reducing the working distance WD at the same time. This is caused by an increased refraction per unit length, leading to higher numerical apertures and ultimately smaller spot sizes d_{t}. On the other hand, the comparison with diamond shows the possibilities with this geometry if an even better suited x-ray optical material could be coated to the Si scaffold instead of Al_2O_3. An important factor when calculating these lens properties is the actual density of the material. For silicon and diamond the nominal density for a perfect crystalline material are assumed. Silicon wafers used in the semiconductor industry have very high purity values and are grown as single crystals using the czoralsky process. Therefore, these substrates reach the theoretical density used here. For diamond this might not be true, but the nominal single crystal density for diamond was used to emphasize possible performance. However, for Al_2O_3 the achieved density of the coated layer was determined by x-ray reflectometry to $\rho_{\mathrm{Al2O3}} = 3.0\,\mathrm{g\,cm^{-3}}$. This is considerably lower than the value for crystalline Al_2O_3, also called sapphire, of $\rho_{\mathrm{Sapphire}} \approx 4.0\,\mathrm{g\,cm^{-3}}$. Nevertheless, this result is not surprising due to the amorphous epitaxial growth of Al_2O_3 and the temperature dependent embedding of hydroxyl groups ($Al(OH)_x$) [Gro+04].

The fabricated compound Si-Al_2O_3 RLL was successfully characterized at the nanoprobe endstation of beamline P06 at PETRA III. The lenses were used in a crossed geometry (cf. Figure 7.2) with an aperture defining entrance slit opening of $40\,\mu\mathrm{m} \times 40\,\mu\mathrm{m}$. Far-field diffraction patterns of an NTT-AT resolution test chart (model ATN/XRESO-50HC) were recorded using the LAMBDA detector [Pen+13]. The data set was evaluated using the ptychography algorithm (Section 5.2). From the reconstructed complex illumination function a beam caustic was generated by propagating the wave field using the Fresnel-Kirchhoff propagator. The results are presented in Figure 7.4. The beam caustics in Figure 7.4(a),(b) reveal a splitting of the wave field upstream of the focal plane as well as an astigmatism. The latter is

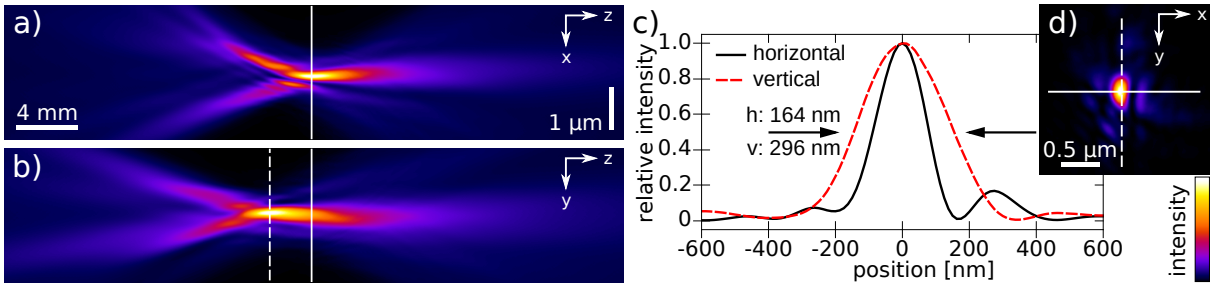

Figure 7.4: A propagated wave field of a crossed RLL lens set is shown in horizontal and vertical projection in (a) and (b), respectively. The dashed vertical focal plane lies $3\,\mathrm{mm}$ upstream of the horizontal one, marked by the solid line. The intensity profiles in (c) are taken from the plane shown in (d), which corresponds to the solid line in (a) and (b). (Reprinted with permission from [Sei+14a]. Copyright 2014, AIP Publishing LLC.)

caused by misaligning the lenses with respect to each other and is not a feature of the optics themselves. However, the characteristic splitting of the wave field is caused by spherical aberrations. As noted earlier in Figure 7.3(d) the etching process led to a depth-dependent Si thickness. Effectively this translates to a depth dependent deformed lens profile in projection, deviating significantly from the ideal parabolic shape, since the lamellar shape is only valid for the nominal design thickness d (cf. Equation (4.9)). In addition, this dependency also means varying focal distances for each etch depth, as lamella shape and thickness directly translate to a certain refractive power. These aberrations result in a focal spot size measured to $164\,\mathrm{nm} \times 296\,\mathrm{nm}$ (h×v) as shown in Figure 7.4(c),(d). When neglecting the astigmatism due to alignment errors, the vertical spot size can be determined to $201\,\mathrm{nm}$ if measured in the dashed plane of Figure 7.4(b). That is an increase by roughly a factor of two in both directions as compared to ideal focal spot sizes in Table 7.1. The results were published in 2014 by Seiboth et al. [Sei+14a] and further details can be found in the diploma thesis of Maria Scholz [Sch14].

7.3 Al_2O_3 RLL

After the initial proof-of-concept for the new lens shape with a compound lamella made of both Si and Al_2O_3 the aim was to create a lamellar lens solely made of Al_2O_3 to achieve the best possible performance by completely removing the Si. To achieve this objective the initial Si scaffold and subsequent processing of the wafer had to be changed completely. A schematic of the new Si scaffold and subsequent structuring steps are shown in Figure 7.5.

For each fabrication step the lens wafer is viewed from the top or from the side. The initial Si scaffold shown in Figure 7.5(a) and also Figure 7.1(b) is structured such that the space in between two lamellae is either filled with Si or etched out. The future lamellae are indicated by the dashed lines. After this initial Si structuring the scaffold is coated with Al_2O_3 by ALD, covering the wafer completely from the top (Figure 7.5(b)). One challenge is to remove the remaining Si between the lamellae. Since the wafer is covered by Al_2O_3, which is hard to remove by wet etching processes, the complete Si substrate was removed from the backside. The remaining structure is a $2\,\mu\mathrm{m}$ thick film of Al_2O_3 that forms the lens and all other elements (Figure 7.5(c) and Figure 7.1(c)). This structure itself is very fragile and was glued to another Si wafer with photoresist in order to stabilize it. These last steps are a crucial aspect of lens fabrication and have tremendously influenced the achieved performance of the Al_2O_3-only RLL.

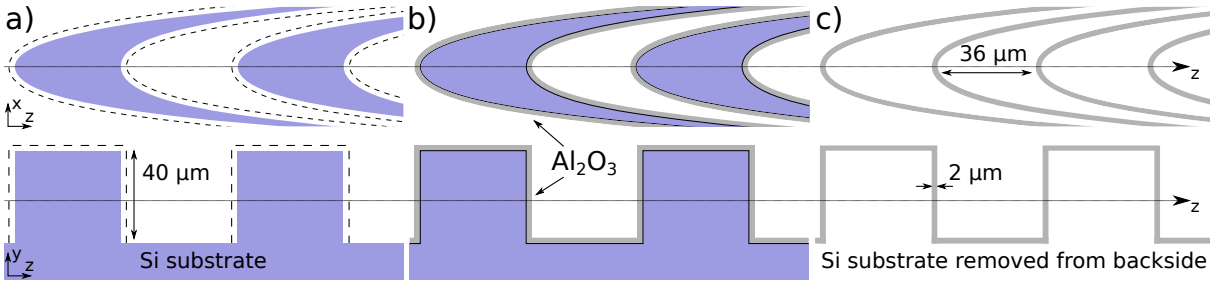

Figure 7.5: Schematic cross-section along the optical axis z through lens lamellae at different fabrication stages. Top row: View from above. Bottom row: Side view. On the initial Si scaffold (a) we applied a 2 µm thick Al_2O_3 layer by ALD (b). After the Si scaffold is removed only thin Al_2O_3 lamellae remain, forming the RLL lens stack.

		N	R	l	d	NA	d_t	WD	T
Si NFL	H	212	13.8 µm	30 µm	1.5 µm	4.95×10^{-4}	63 nm	12.9 mm	0.026
	V	106	11.4 µm			3.80×10^{-4}	82 nm		
Al_2O_3 RLL	H	140	20 µm	36 µm	2.0 µm	4.95×10^{-4}	63 nm	24.5 mm	0.117
	V	96				3.82×10^{-4}	81 nm		
Al_2O_3 RLL	H	234	20 µm	36 µm	2.0 µm	6.72×10^{-4}	46 nm	12.8 mm	0.049
	V	148				5.13×10^{-4}	60 nm		

Table 7.2: Comparison of NFL versus RLL ($\rho_{Al2O3} = 3.0\,g\,cm^{-3}$) focusing with identical numerical apertures NA. In addition, an example of an RLL with smallest spot size and the constraint of a reasonable working distance WD, suitable for user experiments, is given. All lens setups are calculated for a photon energy of $E_{ph} = 15\,keV$ with a geometric aperture of $D = 40\,\mu m$.

A theoretical comparison between a Si NFL and an Al_2O_3 RLL with identical numerical aperture NA is given in Table 7.2. Additionally an RLL with a comparable working distance WD as the NFL, while achieving higher transmission T and smaller spot sizes d_t, is also shown. Despite the fact that the RLL is made of thicker material than the NFL ($d_{RLL} > d_{NFL}$) and the radius of curvature is also larger for the RLL, the higher refractive power and lower absorption result both in fewer lenses needed while achieving the same NA. This results in a higher transmission and also a larger working distance, which is desirable for many applications where special sample environments are neccesary, while keeping the focal spot size the same. On the other hand comparable working distances are achieved at slightly increased transmission while decreasing the focal spot sizes by almost 70 %.

First experiments with these lenses were carried out at ID13 of the ESRF, using the lens set with a typical NA of NFLs as described by the upper "Al_2O_3 RLL" lens in Table 7.2. Due to the fragile nature of the lamellae structure to stress during removal of the Si substrate, and due to the difficult handling thereafter, lenses were not completely flat. An example is given in Figure 7.6, showing the aligned horizontal and vertical wafer in transmission of the flat x-ray beam. The vertical lens wafer appears thicker than the horizontal one. In addition, the vertical lens seems only homogeneous in the central part. To the outside the lens resembles a cone shape. By tilting the vertical lens the alignment could not be further improved. The tilt series revealed a slight bend of the whole wafer along the optical axis, causing the described phenomena. However, the horizontal wafer appears flat, features like bar codes and individual lenses are more sharply recognizable and the wafer is much thinner. Here, a dominant feature in that wafer is

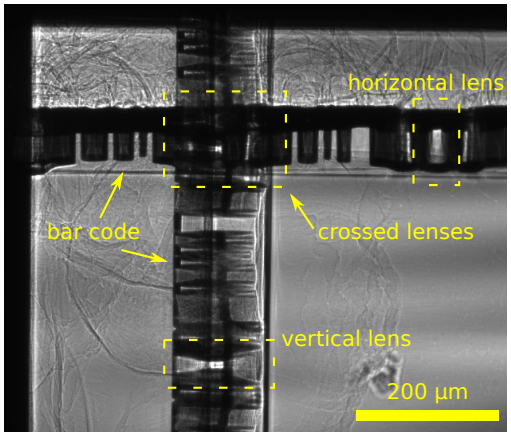

Figure 7.6: X-ray transmission image of a pair of crossed Al_2O_3-only RLLs. One single lens is marked by a dashed rectangle. The overlapping region of two lenses is also marked in the same way. The structures in between lenses are bar codes to identify individual lenses on the wafer.

a highly absorbing layer on the top. This layer cuts off the bar codes as well as the lens. The removal of the Si scaffold from the backside was apparently not successful and a layer of Si remained. Though, this layer seems to stabilize the wafer longitudinally, preventing a bending like in the case of the vertical wafer.

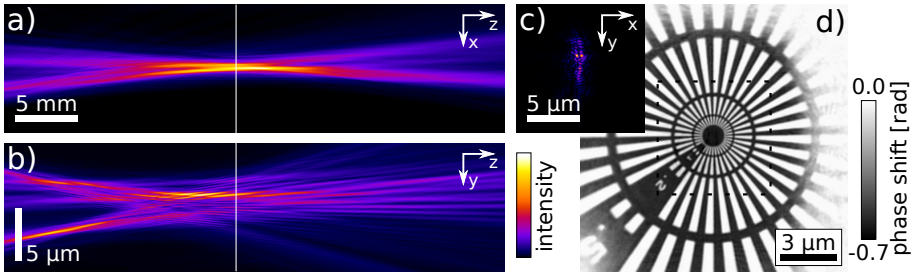

Figure 7.7: A projection of the wave field around the focus is shown in horizontal and vertical direction in (a) and (b), respectively. The wave field in the assumed focal plane marked by the white line in (a) and (b) is shown in (c). The reconstructed object phase with the scanned area marked by a dashed rectangle is depicted in (d).

Although lenses appeared far from ideal in the high resolution camera in Figure 7.6, a ptychographic scan was carried out in order to characterize the focused wave field. Results are shown in Figure 7.7. The caustics in Figure 7.7(a),(b) reveal a strongly broadened wave field in the vertical direction compared to the horizontal case. This is also apparent in Figure 7.7(c), showing a vertically elongated wave field. Since the vertical lens is twisted along the optical axis, the resulting focus is very bad. Therefore, an interpretation of the results, especially for the superior horizontal lens, is very difficult. In the center of Figure 7.7(c) two bright speckles are visible. The size of each of them is roughly $180\,\mathrm{nm}$. Compared to the theoretical values in Table 7.2 for the horizontal lens of the upper "Al_2O_3 RLL" set the spot size is increased by more than a factor of two.

These recent experiments show that the fabrication of Al_2O_3-only RLLs is still at the beginning and much has to be improved upon the manufacturing side. Main challenge is to stabilize the fragile lamellae structure in order to avoid any deformation. One possible solution could be to use the bar code region in between lenses. Here, the silicon scaffold would be left untouched in order to provide more support for the lens. Another aspect is the mounting of the finished RLL to some support material. For these experiments we simply utilized photo resist to glue the RLL onto a raw Si wafer. Since photo resist is not very radiation hard this method might not work for lenses that shall be constantly used in routine

operation. In addition, the handling of the RLL during these mounting procedures has to be carried out with caution. The development of these procedures is a current research topic and improved RLLs are in sight.

7.4 Summary of Results

A short listing is given of the key findings within this chapter.

- The completely new lens shape of bent lamellae (RLL) was successfully fabricated with the help of a silicon scaffold (cf. Figure 7.3).
- A compound RLL consisting of Si and Al_2O_3 showed promising results and was a proof-of-concept for the new lens design [Sei+14a].
- The compound RLL showed typical Si microfabrication problems like slanted sidewalls for high aspect ratios. They are problematic for this new lens shape, since it relies on a constant thickness profile over the whole etch depth.
- Despite these shape errors a focal spot size of $164\,\mathrm{nm} \times 296\,\mathrm{nm}$ (h×v) was measured, which is only a factor two above the expected values (cf. Figure 7.4).
- A new RLL fabrication scheme was presented (cf. Figure 7.5) that removes the Si scaffold completely after the Al_2O_3 coating process, leading to an Al_2O_3-only RLL. This eliminates the slanted sidewall problem, but new challenges were imposed by the now fragile Al_2O_3 structure that is left without any support.
- While the Al_2O_3-only RLL could be characterized at ID13 of the ESRF, a good nanofocusing result could not be obtained (cf. Figure 7.7).
- Main concern is the fragile nature of the Al_2O_3 lamellae. In next RLL iterations stabilizing elements in between lens stacks out of Si are foreseen.

8 Conclusion and Outlook

Effective and aberration-free nanofocusing of hard x rays is an important key component in all experimental scenarios where highest resolution [Hol+14; Sch+15] and extreme intensities [Yon+14] are demanded. In this thesis concepts were developed to enhance hard x-ray nanofocusing capabilities at both storage ring and x-ray free-electron laser sources by refractive x-ray optics. Starting from the problem of compatibility of suitable lens materials and available structuring techniques a completely new lens shape was devised in Section 4.2, named by refractive lamellar lens (RLL). The unconventional shape allows to utilize new materials such as Al_2O_3 by thin film techniques, a material with favorable x-ray optical properties in comparison to currently utilized silicon (cf. Section 4.4). The working principle of these lenses was successfully demonstrated [Sei+14a] and recent developments towards pure Al_2O_3 optics are pointed out. The main field of application are storage ring sources with limited coherence properties where small aperture optics with shortest focal distances are beneficial. While the theoretical advantages of Al_2O_3 lenses were highlighted in Table 7.1 and Table 7.2, achieved performance in experiments could not reach these aims in terms of focal spot size since lens shape accuracy was insufficient. Similar to NFLs the accurate structuring of the scaffold into Si with high aspect ratios is crucial. Nevertheless, a compound RLL consisting of Si and Al_2O_3 created a focal spot of $164\,\mathrm{nm} \times 296\,\mathrm{nm}$ (h×v), enlarged only by a factor of two compared to theoretical values. In a next iteration the RLL idea was taken one step further and an Al_2O_3-only RLL was created. Here, the fragile structure of the thin Al_2O_3 lamellae has to be considered. While the new pure Al_2O_3 RLL avoids problems with slanted Si scaffold side walls by design, stabilization of the lamellae and the removal of the Si scaffold have to be improved. As this was the very first prototype consisting only of Al_2O_3 various improvements are investigated for future upgrades. Especially in the optically not contributing regions between lens stacks we plan to implement stabilizing elements of intentionally not removed Si scaffolds. In general, the new lens shape provides an interesting platform for refractive lenses made by thin film techniques. Currently Al_2O_3 is a promising material that is applicable by ALD. If manufacturing constraints can be resolved focal spot sizes could be reduced to $70\,\%$ of current Si NFLs and the gain of the optical system increased by at least a factor of four (cf. Figure 4.9). In the future also RLLs made of diamond may become an option if thin film techniques evolve, which would lead to tremendous improvements in both focal spot size and gain (cf. Figure 4.7 and 4.8).

Besides this completely new development, another main focus of this work was the aberration correction of current compound refractive lenses (CRLs) made of beryllium using phase plates (cf. Section 5.3). Since CRLs find a widespread use at numerous x-ray sources of the third generation and even free-electron laser sources, this development will be crucial for a variety of future nanofocusing experiments at these sources. Many x-ray optics that are used today are far from being considered aberration free [Sch+10b; Kew+10; Vil+11; Nil+12], especially when larger apertures and radiation hardness are demanded, e. g. at XFELs [Dav+11; Sch+13]. Very high-quality reflective hard x-ray optics exist today for XFEL use [Yum+13; Mim+14], but the extremely high expenditure and setup complexity may prevent

a wide utilization. In general, limitations are imposed by the accuracy of current fabrication techniques. Overcoming these restrictions is of course one of the great challenges today.

The developed phase plate in this thesis presents a concrete solution to overcome certain limitations in refractive x-ray optics fabrication. Throughout Chapter 6 the successful correction of strong spherical aberrations in a set of 20 Be CRLs with $R = 50\,\mu\mathrm{m}$ was demonstrated. Overall wavefront errors were reduced from over $1.3\,\lambda$ down to below $0.2\,\lambda$. The strength of spherical aberrations measured by Zernike polynomial decomposition was reduced by an order of magnitude from $0.4\,\lambda^{-1}$ down to $0.04\,\lambda^{-1}$. One challenge in using the phase plate is the accurate alignment with respect to the aberrated optics. Two different approaches were successfully realized in this work. The fixed alignment of the phase plate together with the aberrated optics provides a compact unit where only one alignment step and no additional experimental controls are necessary. However, mechanical challenges are more significant. If this accuracy is somehow not achievable an aberration correction may also be realized by additional alignment stages in a variable setup. Both alternatives were presented and comparable results achieved. For the use with Be CRLs the fixed model is the most elegant solution, since the phase plate holder has the same form factor as a single lens and can simply be inserted at the end of the lens stack.

With the techniques of high-accuracy aberration characterization by ptychography and the microstructuring capabilities of high-intensity short-pulse laser ablation a broad variety of x-ray optics and aberrations may be corrected by this phase plate approach, limiting its application not only to refractive x-ray lenses. While wavefront manipulation by a phase plate may not be as adaptive as previous schemes relying on deformable reflective optics [Mim+10], its portability, simple integration into existing setups, and affordable fabrication are key benefits of this solution. The successful demonstration of aberration correction at very different synchrotron radiation facilities in this thesis emphasizes this aspect. These characteristics will allow one to equip any aberrated optics with a phase plate and also retrofit a phase plate to existing setups, enhancing their performance.

One of the most obvious steps to improve the phase plate performance is a reduction in substrate thickness. First prototypes were structured in over $100\,\mu\mathrm{m}$ thick SiO_2 plates, were in theory only $40\,\mu\mathrm{m}$ were needed. A logical step is therefore the use of appropriate substrate thicknesses that correspond to the needed maximum phase shift in order to correct aberrations. Depending on the final phase plate shape a remaining substrate offset of $5\,\mu\mathrm{m}$ seems feasible in order to guarantee sufficient stability of the phase plate structure itself. In the scenario described within this work an increase in phase plate transmission from $54\,\%$ to roughly $90\,\%$ can be achieved on this way. With this the phase plate is not only creating an aberration free focus, but also increases achievable peak intensities in the focal region considerably compared to an uncorrected CRL optic, despite the additional phase plate absorption. As shown in Figure 6.12 an uncorrected Be CRL stack reaches only $25\,\%$ of the peak intensity in focus compared to an aberration free system. Experiments demonstrated an increase of peak intensity to $48\,\%$, taking the thick substrate material of roughly $120\,\mu\mathrm{m}$ into account. A considerable reduction in phase plate absorption is in sight by using $40\,\mu\mathrm{m}$ thick substrates, which would increase the peak intensity to over $75\,\%$ with current fabrication capabilities. A refinement of the shape accuracy and alignment procedures could increase this to $90\,\%$.

Another interesting approach that will be pursued is the use of diamond as a substrate material, which could increase the phase plate transmission even more, leading to peak intensities of $98\,\%$ for the investigated optical system. Very recent developments showed the feasibility of diamond micro fabrication by

a short-pulse high-intensity laser to manufacture refractive x-ray lenses [Ter+15]. Depending on strength and type of lens aberrations the requirements on manufacturing a diamond phase plate are very similar. Thus, developments in both refractive lenses and upcoming phase plate iterations will stimulate each other, further refining the promising technique of short-pulse laser ablation for x-ray optics manufacturing.

Fourth generation synchrotron sources and the advent of diffraction limited storage rings are the propulsive forces in current developments in x-ray optics and the exploitation of new materials and manufacturing techniques. Throughout this work a new refractive lens design based on thin film techniques and a universal approach to correct aberrations in many of nowadays utilized x-ray optics was presented. Especially at XFELs a large community will benefit from aberration free nanofocusing to pursue science with unprecedented temporal and spatial resolution and to explore previously unaccessible states of matter.

Bibliography

[AM11] J. Als-Nielsen and D. McMorrow. *Elements of modern X-ray physics*. John Wiley & Sons, 2011.

[Ama+12] J. Amann, W. Berg, V. Blank, F.-J. Decker, Y. Ding, P. Emma, Y. Feng, J. Frisch, D. Fritz, J. Hastings, Z. Huang, J. Krzywinski, R. Lindberg, H. Loos, A. Lutman, H.-D. Nuhn, D. Ratner, J. Rzepiela, D. Shu, Y. Shvyd'ko, S. Spampinati, S. Stoupin, S. Terentyev, E. Trakhtenberg, D. Walz, J. Welch, J. Wu, A. Zholents, and D. Zhu. Demonstration of self-seeding in a hard-X-ray free-electron laser. *Nat Photon* **6**(10) (2012), 693–698.

[Att00] D. Attwood. *Soft x-rays and extreme ultraviolet radiation: principles and applications*. Cambridge University Press, 2000.

[Bal+04] K. Balewski, W. Brefeld, W. Decking, H. Franz, R. Röhlsberger, and E. Weckert. *PETRA III: A Low Emittance Synchrotron Radiation Source*. Tech. rep. Desy, 2004.

[Bal+11] R. Ballabriga, M. Campbell, E. Heijne, X. Llopart, L. Tlustos, and W. Wong. Medipix3: A 64k pixel detector readout chip working in single photon counting mode with improved spectrometric performance. *Nuclear Instruments and Methods in Physics Research Section A: Accelerators, Spectrometers, Detectors and Associated Equipment* **633, Supplement 1** (2011). 11th International Workshop on Radiation Imaging Detectors, S15–S18.

[Bau14] C. Baumbach. "Entfaltung von Röntgenfluoreszenzbildern mittels Ptychographie." Dissertation. Universität Hamburg, Department Physik, 2014.

[BDM92] R. Bonifacio, L. De Salvo Souza, and B. McNeil. Emittance limitations in the free electron laser. *Optics Communications* **93**(3) (1992), 179–185.

[BDR95] P. Bösecke, O. Diat, and B. Rasmussen. High-brilliance Beamline at the European Synchrotron Radiation Facility. *Review of Scientific Instruments* **66**(2) (1995), 1636–1638.

[BG03] D. Briggs and J. T. Grant. *Surface analysis by Auger and X-ray photoelectron spectroscopy*. IM publications, 2003.

[BMP89] R. Bonifacio, B. W. J. McNeil, and P. Pierini. Superradiance in the high-gain free-electron laser. *Phys. Rev. A* **40** (8 1989), 4467–4475.

[Boy09] P. Boye. "Nanofocusing refractive X-ray lenses." Dissertation. Technische Universität Dresden, Institute of Structural Physics, 2009.

[BPN84] R. Bonifacio, C. Pellegrini, and L. Narducci. Collective instabilities and high-gain regime in a free electron laser. *Optics Communications* **50**(6) (1984), 373–378.

[Bra+13] S. Braun, A. Kubec, M. Menzel, S. Niese, P. Krüger, F. Seiboth, J. Patommel, and C. Schroer. Multilayer Laue Lenses with Focal Length of 10 mm. *Journal of Physics: Conference Series* **425**(5) (2013), 052019.

[Bun+08] O. Bunk, M. Dierolf, S. Kynde, I. Johnson, O. Marti, and F. Pfeiffer. Influence of the overlap parameter on the convergence of the ptychographical iterative engine. *Ultramicroscopy* **108**(5) (2008), 481–487.

[BW80] M. Born and E. Wolf. *Principles of optics: electromagnetic theory of propagation, interference and diffraction of light*. Pergamon Press, 1980.

[CS14] C. Chang and A. Sakdinawat. Ultra-high aspect ratio high-resolution nanofabrication for hard X-ray diffractive optics. *Nat Commun* **5** (2014),

[Dav+11] C. David, S. Gorelick, S. Rutishauser, J. Krzywinski, J. Vila-Comamala, V. A. Guzenko, O. Bunk, E. Farm, M. Ritala, M. Cammarata, D. M. Fritz, R. Barrett, L. Samoylova, J. Grunert, and H. Sinn. Nanofocusing of hard X-ray free electron laser pulses using diamond based Fresnel zone plates. *Sci. Rep.* **1** (2011),

[Dea+77] D. A. G. Deacon, L. R. Elias, J. M. J. Madey, G. J. Ramian, H. A. Schwettman, and T. I. Smith. First Operation of a Free-Electron Laser. *Phys. Rev. Lett.* **38**(16) (1977), 892–894.

[Dzh+14] D. Dzhigaev, U. Lorenz, R. P. Kurta, F. Seiboth, T. Stankevic, S. Mickevicius, A. Singer, A. Shabalin, O. M. Yefanov, M. N. Strikhanov, G. Falkenberg, C. G. Schroer, R. Feidenhans'l, and I. A. Vartanyants. Ptychographical imaging of the phase vortices in the x-ray beam formed by nanofocusing lenses. *Journal of Physics: Conference Series* **499**(1) (2014), 012020.

[Eld+47] F. R. Elder, A. M. Gurewitsch, R. V. Langmuir, and H. C. Pollock. Radiation from Electrons in a Synchrotron. *Phys. Rev.* **71**(11) (1947), 829–830.

[Emm+10] P. Emma, R. Akre, J. Arthur, R. Bionta, C. Bostedt, J. Bozek, A. Brachmann, P. Bucksbaum, R. Coffee, F.-J. Decker, Y. Ding, D. Dowell, S. Edstrom, A. Fisher, J. Frisch, S. Gilevich, J. Hastings, G. Hays, P. Hering, Z. Huang, R. Iverson, H. Loos, M. Messerschmidt, A. Miahnahri, S. Moeller, H.-D. Nuhn, G. Pile, D. Ratner, J. Rzepiela, D. Schultz, T. Smith, P. Stefan, H. Tompkins, J. Turner, J. Welch, W. White, J. Wu, G. Yocky, and J. Galayda. First lasing and operation of an angstrom-wavelength free-electron laser. *Nat Photon* **4**(9) (2010), 641–647.

[End+14] B. Enders, M. Dierolf, P. Cloetens, M. Stockmar, F. Pfeiffer, and P. Thibault. Ptychography with broad-bandwidth radiation. *Applied Physics Letters* **104**(17), 171104 (2014).

[Fel10] J. Feldhaus. FLASH—the first soft x-ray free electron laser (FEL) user facility. *Journal of Physics B: Atomic, Molecular and Optical Physics* **43**(19) (2010), 194002.

[Fie82] J. R. Fienup. Phase retrieval algorithms: a comparison. *Appl. Opt.* **21**(15) (1982), 2758–2769.

[FM10] J. Falta and T. Möller. *Forschung mit Synchrotronstrahlung - Eine Einführung in die Grundlagen und Anwendungen*. Vieweg+Teubner, 2010.

[Goo00] J. W. Goodman. *Statistical optics*. Wiley classics library ed. Wiley: Wiley, 2000.

[Goo05] J. Goodman. *Introduction to Fourier Optics*. McGraw-Hill physical and quantum electronics series. Roberts & Company, 2005.

[Gro+04] M. D. Groner, F. H. Fabreguette, J. W. Elam, and S. M. George. Low-Temperature Al2O3 Atomic Layer Deposition. *Chemistry of Materials* **16**(4) (2004), 639–645.

[Gut+12] C. Gutt, P. Wochner, B. Fischer, H. Conrad, M. Castro-Colin, S. Lee, F. Lehmkühler, I. Steinke, M. Sprung, W. Roseker, D. Zhu, H. Lemke, S. Bogle, P. H. Fuoss, G. B. Stephenson, M. Cammarata, D. M. Fritz, A. Robert, and G. Grübel. Single Shot Spatial and Temporal Coherence Properties of the SLAC Linac Coherent Light Source in the Hard X-Ray Regime. *Phys. Rev. Lett.* **108** (2 2012), 024801.

[GW53] H. S. Green and E. Wolf. A Scalar Representation of Electromagnetic Fields. *Proceedings of the Physical Society. Section A* **66**(12) (1953), 1129.

[Har+13] T. Hara, Y. Inubushi, T. Katayama, T. Sato, H. Tanaka, T. Tanaka, T. Togashi, K. Togawa, K. Tono, M. Yabashi, and T. Ishikawa. Two-colour hard X-ray free-electron laser with wide tunability. *Nat Commun* **4** (2013),

[Hau11] S. P. Hau-Riege. *High-intensity X-rays - interaction with matter / processes in plasmas, clusters, molecules, and solids*. 1. ed. Wiley-VCH: Wiley-VCH, 2011.

[Hec02] E. Hecht. *Optics*. 4. ed., international ed. Addison-Wesley: Addison-Wesley, 2002.

[Hem+14] E. Hemsing, G. Stupakov, D. Xiang, and A. Zholents. Beam by design: Laser manipulation of electrons in modern accelerators. *Rev. Mod. Phys.* **86** (3 2014), 897–941.

[Her+02] M. A. Herráez, D. R. Burton, M. J. Lalor, and M. A. Gdeisat. Fast two-dimensional phase-unwrapping algorithm based on sorting by reliability following a noncontinuous path. *Appl. Opt.* **41**(35) (2002), 7437–7444.

[Her+13] S. Herrmann, S. Boutet, B. Duda, D. Fritz, G. Haller, P. Hart, R. Herbst, C. Kenney, H. Lemke, M. Messerschmidt, J. Pines, A. Robert, M. Sikorski, and G. Williams. CSPAD-140k: A versatile detector for LCLS experiments. *Nuclear Instruments and Methods in Physics Research Section A: Accelerators, Spectrometers, Detectors and Associated Equipment* **718** (2013). Proceedings of the 12th Pisa Meeting on Advanced Detectors, La Biodola, Isola d'Elba, Italy, May 20 – 26, 2012, 550–553.

[HH70] R. Hegerl and W. Hoppe. Dynamische Theorie der Kristallstrukturanalyse durch Elektronenbeugung im inhomogenen Primärstrahlwellenfeld. *Berichte der Bunsengesellschaft für physikalische Chemie* **74**(11) (1970), 1148–1154.

[HK07] Z. Huang and K.-J. Kim. Review of x-ray free-electron laser theory. *Phys. Rev. ST Accel. Beams* **10** (3 2007), 034801.

[HOH03] O. Hemberg, M. Otendal, and H. M. Hertz. Liquid-metal-jet anode electron-impact x-ray source. *Applied Physics Letters* **83**(7) (2003), 1483–1485.

[Hol+14] M. Holler, A. Diaz, M. Guizar-Sicairos, P. Karvinen, E. Färm, E. Härkönen, M. Ritala, A. Menzel, J. Raabe, and O. Bunk. X-ray ptychographic computed tomography at 16 nm isotropic 3D resolution. *Sci. Rep.* **4** (2014),

[Hop+13] R. Hoppe, J. Reinhardt, G. Hofmann, J. Patommel, J.-D. Grunwaldt, C. D. Damsgaard, G. Wellenreuther, G. Falkenberg, and C. G. Schroer. High-resolution chemical imaging of gold nanoparticles using hard x-ray ptychography. *Applied Physics Letters* **102**(20) (2013), 203104.

[HTB94] S. Hoffman, D. Thiel, and D. Bilderback. Developments in tapered monocapillary and polycapillary glass X-ray concentrators. *Nuclear Instruments and Methods in Physics Research Section A: Accelerators, Spectrometers, Detectors and Associated Equipment* **347**(1-3) (1994), 384–389.

[Ish+12] T. Ishikawa, H. Aoyagi, T. Asaka, Y. Asano, N. Azumi, T. Bizen, H. Ego, K. Fukami, T. Fukui, Y. Furukawa, S. Goto, H. Hanaki, T. Hara, T. Hasegawa, T. Hatsui, A. Higashiya, T. Hirono, N. Hosoda, M. Ishii, T. Inagaki, Y. Inubushi, T. Itoga, Y. Joti, M. Kago, T. Kameshima, H. Kimura, Y. Kirihara, A. Kiyomichi, T. Kobayashi, C. Kondo, T. Kudo, H. Maesaka, X. M. Marechal, T. Masuda, S. Matsubara, T. Matsumoto, T. Matsushita, S. Matsui, M. Nagasono, N. Nariyama, H. Ohashi, T. Ohata, T. Ohshima, S. Ono, Y. Otake, C. Saji, T. Sakurai, T. Sato, K. Sawada, T. Seike, K. Shirasawa, T. Sugimoto, S. Suzuki, S. Takahashi, H. Takebe, K. Takeshita, K. Tamasaku, H. Tanaka, R. Tanaka, T. Tanaka, T. Togashi, K. Togawa, A. Tokuhisa, H. Tomizawa, K. Tono, S. Wu, M. Yabashi, M. Yamaga, A. Yamashita, K. Yanagida, C. Zhang, T. Shintake, H. Kitamura, and N. Kumagai. A compact X-ray free-electron laser emitting in the sub-angstrom region. *Nat Photon* **6**(8) (2012), 540–544.

[Jac98] J. D. Jackson. *Classical Electrodynamics Third Edition*. Vol. 67. Wiley, 1998.

[Jam54] R. James. *The optical principles of the diffraction of X-rays*. The crystalline state. G. Bell, 1954.

[Jen99] R. Jenkins. *X-ray fluorescence spectrometry*. 2. ed. Wiley: Wiley, 1999.

[Kan+06] H. C. Kang, J. Maser, G. B. Stephenson, C. Liu, R. Conley, A. T. Macrander, and S. Vogt. Nanometer Linear Focusing of Hard X Rays by a Multilayer Laue Lens. *Phys. Rev. Lett.* **96** (12 2006), 127401.

[KB48] P. Kirkpatrick and A. V. Baez. Formation of Optical Images by X-Rays. *J. Opt. Soc. Am.* **38**(9) (1948), 766–773.

[Kew+10] C. M. Kewish, M. Guizar-Sicairos, C. Liu, J. Qian, B. Shi, C. Benson, A. M. Khounsary, J. Vila-Comamala, O. Bunk, J. R. Fienup, A. T. Macrander, and L. Assoufid. Reconstruction of an astigmatic hard X-ray beam and alignment of K-B mirrors from ptychographic coherent diffraction data. *Opt. Express* **18**(22) (2010), 23420–23427.

[Kim86a] K.-J. Kim. Brightness, coherence and propagation characteristics of synchrotron radiation. *Nuclear Instruments and Methods in Physics Research Section A: Accelerators, Spectrometers, Detectors and Associated Equipment* **246**(1–3) (1986), 71–76.

[Kim86b] K.-J. Kim. Three-Dimensional Analysis of Coherent Amplification and Self-Amplified Spontaneous Emission in Free-Electron Lasers. *Phys. Rev. Lett.* **57** (15 1986), 1871–1874.

[Koy+15] T. Koyama, H. Yumoto, K. Tono, T. Togashi, Y. Inubushi, T. Katayama, J. Kim, S. Matsuyama, M. Yabashi, K. Yamauchi, and H. Ohashi. *Damage to inorganic materials illuminated by focused beam of x-ray free-electron laser radiation*. 2015.

[Kro26] R. L. Kronig. On the Theory of Dispersion of X-Rays. *J. Opt. Soc. Am.* **12**(6) (1926), 547–557.

[Lai+92] B. Lai, W. B. Yun, D. Legnini, Y. Xiao, J. Chrzas, P. J. Viccaro, V. White, S. Bajikar, D. Denton, F. Cerrina, E. Di Fabrizio, M. Gentili, L. Grella, and M. Baciocchi. Hard x-ray phase zone plate fabricated by lithographic techniques. *Applied Physics Letters* **61**(16) (1992), 1877–1879.

[Lam+08] G. Lambert, T. Hara, D. Garzella, T. Tanikawa, M. Labat, B. Carre, H. Kitamura, T. Shintake, M. Bougeard, S. Inoue, Y. Tanaka, P. Salieres, H. Merdji, O. Chubar, O. Gobert, K. Tahara, and M.-E. Couprie. Injection of harmonics generated in gas in a free-electron laser providing intense and coherent extreme-ultraviolet light. *Nat Phys* **4**(4) (2008), 296–300.

[Len+02] B. Lengeler, C. G. Schroer, B. Benner, A. Gerhardus, T. F. Günzler, M. Kuhlmann, J. Meyer, and C. Zimprich. Parabolic refractive X-ray lenses. *Journal of Synchrotron Radiation* **9**(3) (2002), 119–124.

[Len+98] B. Lengeler, J. Tummler, A. Snigirev, I. Snigireva, and C. Raven. Transmission and gain of singly and doubly focusing refractive x-ray lenses. *Journal of Applied Physics* **84**(11) (1998), 5855–5861.

[Len+99] B. Lengeler, C. Schroer, J. Tummler, B. Benner, M. Richwin, A. Snigirev, I. Snigireva, and M. Drakopoulos. Imaging by parabolic refractive lenses in the hard X-ray range. *Journal of Synchrotron Radiation* **6** (1999), 1153–1167.

[Li+05] Y. Li, S. Krinsky, J. Lewellen, and V. Sajaev. Frequency-domain statistics of the chaotic optical field of a high-gain, self-amplified free-electron laser and its correlation to the time-domain statistics. English. *Applied Physics B* **80**(1) (2005), 31–34.

[Lut+14] A. A. Lutman, F.-J. Decker, J. Arthur, M. Chollet, Y. Feng, J. Hastings, Z. Huang, H. Lemke, H.-D. Nuhn, A. Marinelli, J. L. Turner, S. Wakatsuki, J. Welch, and D. Zhu. Demonstration of Single-Crystal Self-Seeded Two-Color X-Ray Free-Electron Lasers. *Phys. Rev. Lett.* **113** (25 2014), 254801.

[Mad71] J. M. J. Madey. Stimulated Emission of Bremsstrahlung in a Periodic Magnetic Field. *Journal of Applied Physics* **42**(5) (1971), 1906–1913.

[Mai+12] A. Maiden, M. Humphry, M. Sarahan, B. Kraus, and J. Rodenburg. An annealing algorithm to correct positioning errors in ptychography. *Ultramicroscopy* **120** (2012), 64–72.

[Mal07] D. Malacara. *Optical shop testing*. 3rd ed. John Wiley: John Wiley, 2007.

[Mar+03] S. Marchesini, H. He, H. N. Chapman, S. P. Hau-Riege, A. Noy, M. R. Howells, U. Weierstall, and J. C. H. Spence. X-ray image reconstruction from a diffraction pattern alone. *Phys. Rev. B* **68** (14 2003), 140101.

[Mar+15] A. Marinelli, D. Ratner, A. Lutman, J. Turner, J. Welch, F.-J. Decker, H. Loos, C. Behrens, S. Gilevich, A. Miahnahri, S. Vetter, T. Maxwell, Y. Ding, R. Coffee, S. Wakatsuki, and Z. Huang. High-intensity double-pulse X-ray free-electron laser. *Nat Commun* **6** (2015).

[Mas+04] J. Maser, G. B. Stephenson, S. Vogt, W. Yun, A. Macrander, H. C. Kang, C. Liu, and R. Conley. *Multilayer Laue lenses as high-resolution x-ray optics*. 2004.

[Mia+99] J. Miao, P. Charalambous, J. Kirz, and D. Sayre. Extending the methodology of X-ray crystallography to allow imaging of micrometre-sized non-crystalline specimens. *Nature* **400**(6742) (1999), 342–344.

[Mic91] A. G. Michette. No X-ray lens. *Nature* **353**(6344) (1991), 510–510.

[Mim+10] H. Mimura, S. Handa, T. Kimura, H. Yumoto, D. Yamakawa, H. Yokoyama, S. Matsuyama, K. Inagaki, K. Yamamura, Y. Sano, K. Tamasaku, Y. Nishino, M. Yabashi, T. Ishikawa, and K. Yamauchi. Breaking the 10 nm barrier in hard-X-ray focusing. *Nat Phys* **6**(2) (2010), 122–125.

[Mim+14] H. Mimura, H. Yumoto, S. Matsuyama, T. Koyama, K. Tono, Y. Inubushi, T. Togashi, T. Sato, J. Kim, R. Fukui, Y. Sano, M. Yabashi, H. Ohashi, T. Ishikawa, and K. Yamauchi. Generation of 10ˆ20 W/cmˆ2 hard X-ray laser pulses with two-stage reflective focusing system. *Nat Commun* **5** (2014).

[Mor+15] A. J. Morgan, M. Prasciolu, A. Andrejczuk, J. Krzywinski, A. Meents, D. Pennicard, H. Graafsma, A. Barty, R. J. Bean, M. Barthelmess, D. Oberthuer, O. Yefanov, A. Aquila, H. N. Chapman, and S. Bajt. High numerical aperture multilayer Laue lenses. *Sci. Rep.* **5** (2015).

[MR09] A. M. Maiden and J. M. Rodenburg. An improved ptychographical phase retrieval algorithm for diffractive imaging. *Ultramicroscopy* **109**(10) (2009), 1256–1262.

[MT10] B. W. J. McNeil and N. R. Thompson. X-ray free-electron lasers. *Nat Photon* **4**(12) (2010), 814–821.

[Nil+12] D. Nilsson, F. Uhlén, A. Holmberg, H. M. Hertz, A. Schropp, J. Patommel, R. Hoppe, F. Seiboth, V. Meier, C. G. Schroer, E. Galtier, B. Nagler, H. J. Lee, and U. Vogt. Ronchi test for characterization of nanofocusing optics at a hard x-ray free-electron laser. *Opt. Lett.* **37**(24) (2012), 5046–5048.

[NM12] R. Neutze and K. Moffat. Time-resolved structural studies at synchrotrons and X-ray free electron lasers: opportunities and challenges. *Current Opinion in Structural Biology* **22**(5) (2012). Carbohydrates and glycoconjugates ? Biophysical methods, 651–659.

[Nöh+03] B. Nöhammer, J. Hoszowska, A. K. Freund, and C. David. Diamond planar refractive lenses for third- and fourth-generation X-ray sources. *Journal of Synchrotron Radiation* **10**(2) (2003), 168–171.

[Pat10] J. Patommel. “Hard X-Ray Scanning Microscope Using Nanofocusing Parabolic Refractive Lenses.” Dissertation. Technische Universität Dresden, Institute of Structural Physics, 2010.

[Pen+13] D. Pennicard, S. Lange, S. Smoljanin, H. Hirsemann, H. Graafsma, M. Epple, M. Zuvic, M.-O. Lampert, T. Fritzsch, and M. Rothermund. The LAMBDA photon-counting pixel detector. *Journal of Physics: Conference Series* **425**(6) (2013), 062010.

[Pfe+02] F. Pfeiffer, C. David, M. Burghammer, C. Riekel, and T. Salditt. Two-Dimensional X-ray Waveguides and Point Sources. *Science* **297**(5579) (2002), 230–234.

[Pfe+06] F. Pfeiffer, C. David, J. F. van der Veen, and C. Bergemann. Nanometer focusing properties of Fresnel zone plates described by dynamical diffraction theory. *Phys. Rev. B* **73** (24 2006), 245331.

[Pla+13] R. Plackett, I. Horswell, E. N. Gimenez, J. Marchal, D. Omar, and N. Tartoni. Merlin: a fast versatile readout system for Medipix3. *Journal of Instrumentation* **8**(01) (2013), C01038.

[Pol+15] M. Polikarpov, I. Snigireva, J. Morse, V. Yunkin, S. Kuznetsov, and A. Snigirev. Large-acceptance diamond planar refractive lenses manufactured by laser cutting. *Journal of Synchrotron Radiation* **22**(1) (2015), 23–28.

[Pre+07] W. H. [Press, S. A. [Teukolsky, W. T. [Vetterling, and B. P. [Flannery. *Numerical recipes / the art of scientific computing*. Cambridge Univ. Press, 2007.

[Rau+11] C. Rau, U. Wagner, Z. Pešić, and A. De Fanis. Coherent imaging at the Diamond beamline I13. *physica status solidi (a)* **208**(11) (2011), 2522–2525.

[RF04] J. M. Rodenburg and H. M. L. Faulkner. A phase retrieval algorithm for shifting illumination. *Applied Physics Letters* **85**(20) (2004), 4795–4797.

[Rod+07] J. M. Rodenburg, A. C. Hurst, A. G. Cullis, B. R. Dobson, F. Pfeiffer, O. Bunk, C. David, K. Jefimovs, and I. Johnson. Hard-X-Ray Lensless Imaging of Extended Objects. *Phys. Rev. Lett.* **98** (3 2007), 034801.

[Ron64] V. Ronchi. Forty Years of History of a Grating Interferometer. *Appl. Opt.* **3**(4) (1964), 437–451.

[Rön95] W. C. Röntgen. Über eine neue Art von Strahlen. *Sitzungsberichte der Würzburger Physik.-Medic.-Gesellschaft* (1895).

[Sch+01] C. G. Schroer, J. Tuemmler, B. Lengeler, M. Drakopoulos, A. A. Snigirev, and I. Snigireva. Compound refractive lenses: high-quality imaging optics for the X-FEL. In: ed. by D. M. Mills, H. Schulte-Schrepping, and J. R. Arthur. Vol. 4143. 1. San Diego, CA, USA: SPIE, 2001, pp.60–68.

[Sch+03] C. G. Schroer, M. Kuhlmann, U. T. Hunger, T. F. Gunzler, O. Kurapova, S. Feste, F. Frehse, B. Lengeler, M. Drakopoulos, A. Somogyi, A. S. Simionovici, A. Snigirev, I. Snigireva, C. Schug, and W. H. Schroder. Nanofocusing parabolic refractive x-ray lenses. *Applied Physics Letters* **82**(9) (2003), 1485–1487.

[Sch+04] C. G. Schroer, B. Benner, M. Kuhlmann, O. Kurapova, B. Lengeler, F. Zontone, A. A. Snigirev, I. Snigireva, and H. Schulte-Schrepping. Focusing hard x-ray FEL beams with parabolic refractive lenses. In: ed. by S. G. Biedron, W. Eberhardt, T. Ishikawa, and R. O. Tatchyn. Vol. 5534. 1. Denver, CO, USA: SPIE, 2004, pp.116–124.

[Sch+05] C. G. Schroer, O. Kurapova, J. Patommel, P. Boye, J. Feldkamp, B. Lengeler, M. Burghammer, C. Riekel, L. Vincze, A. van der Hart, and M. Kuchler. Hard x-ray nanoprobe based on refractive x-ray lenses. *Applied Physics Letters* **87**(12) (2005), 124103.

[Sch+10a] C. G. Schroer, P. Boye, J. M. Feldkamp, J. Patommel, D. Samberg, A. Schropp, A. Schwab, S. Stephan, G. Falkenberg, G. Wellenreuther, and N. Reimers. Hard X-ray nanoprobe at beamline P06 at PETRA III. *Nuclear Instruments and Methods in Physics Research Section A: Accelerators, Spectrometers, Detectors and Associated Equipment* **616**(2-3) (2010), 93–97.

[Sch+10b] A. Schropp, P. Boye, J. M. Feldkamp, R. Hoppe, J. Patommel, D. Samberg, S. Stephan, K. Giewekemeyer, R. N. Wilke, T. Salditt, J. Gulden, A. P. Mancuso, I. A. Vartanyants, E. Weckert, S. Schoder, M. Burghammer, and C. G. Schroer. Hard x-ray nanobeam characterization by coherent diffraction microscopy. *Applied Physics Letters* **96**(9) (2010), 091102.

[Sch+12] A. Schropp, R. Hoppe, J. Patommel, D. Samberg, F. Seiboth, S. Stephan, G. Wellenreuther, G. Falkenberg, and C. G. Schroer. Hard x-ray scanning microscopy with coherent radiation: Beyond the resolution of conventional x-ray microscopes. *Applied Physics Letters* **100**(25) (2012), 253112.

[Sch+13] A. Schropp, R. Hoppe, V. Meier, J. Patommel, F. Seiboth, H. J. Lee, B. Nagler, E. C. Galtier, B. Arnold, U. Zastrau, J. B. Hastings, D. Nilsson, F. Uhlén, U. Vogt, H. M. Hertz, and C. G. Schroer. Full spatial characterization of a nanofocused x-ray free-electron laser beam by ptychographic imaging. *Sci. Rep.* **3** (2013), 01633.

[Sch+15] A. Schropp, R. Hoppe, V. Meier, J. Patommel, F. Seiboth, Y. Ping, D. G. Hicks, M. A. Beckwith, G. W. Collins, A. Higginbotham, J. S. Wark, H. J. Lee, B. Nagler, E. C. Galtier, B. Arnold, U. Zastrau, J. B. Hastings, and C. G. Schroer. Imaging Shock Waves in Diamond with Both High Temporal and Spatial Resolution at an XFEL. *Sci. Rep.* **5** (2015), 11089.

[Sch+98] C. Schulze, U. Lienert, M. Hanfland, M. Lorenzen, and F. Zontone. Microfocusing of Hard X-rays with Cylindrically Bent Crystal Monochromators. *Journal of Synchrotron Radiation* **5**(2) (1998), 77–81.

[Sch06] C. G. Schroer. Focusing hard x rays to nanometer dimensions using Fresnel zone plates. *Physical Review B* **74**(3) (2006), 033405.

[Sch10] J. R. Schneider. FLASH—from accelerator test facility to the first single-pass soft x-ray free-electron laser. *Journal of Physics B: Atomic, Molecular and Optical Physics* **43**(19) (2010), 194001.

[Sch14] M. Scholz. “Refraktive Lamellarlinsen (RLL) für die Mikroskopie mit harter Röntgenstrahlung.” Diploma Thesis. Technische Universität Dresden, Institute of Structural Physics, 2014.

[Sei+14a] F. Seiboth, M. Scholz, J. Patommel, R. Hoppe, F. Wittwer, J. Reinhardt, J. Seidel, M. Knaut, A. Jahn, K. Richter, J. W. Bartha, G. Falkenberg, and C. G. Schroer. Hard x-ray nanofocusing by refractive lenses of constant thickness. *Applied Physics Letters* **105**(13) (2014), 131110.

[Sei+14b] F. Seiboth, A. Schropp, R. Hoppe, V. Meier, J. Patommel, H. J. Lee, B. Nagler, E. C. Galtier, B. Arnold, U. Zastrau, J. B. Hastings, D. Nilsson, F. Uhlén, U. Vogt, H. M. Hertz, and C. G. Schroer. Focusing XFEL SASE pulses by rotationally parabolic refractive x-ray lenses. *Journal of Physics: Conference Series* **499**(1) (2014), 012004.

[Sni+96] A. Snigirev, V. Kohn, I. Snigireva, and B. Lengeler. A compound refractive lens for focusing high-energy X-rays. *Nature* **384**(6604) (1996), 49–51.

[Som49] A. Sommerfeld. *Partial differential equation in physics*. 1949.

[SS10] A. Schropp and C. G. Schroer. Dose requirements for resolving a given feature in an object by coherent x-ray diffraction imaging. *New Journal of Physics* **12**(3) (2010), 035016.

[SS80] P. Sprangle and R. A. Smith. Theory of free-electron lasers. *Phys. Rev. A* **21** (1 1980), 293–301.

[SSY10] E. L. Saldin, E. A. Schneidmiller, and M. V. Yurkov. Statistical and coherence properties of radiation from x-ray free-electron lasers. English. *NEW JOURNAL OF PHYSICS* **12** (2010).

[Suz+05] Y. Suzuki, A. Takeuchi, H. Takano, and H. Takenaka. Performance Test of Fresnel Zone Plate with 50 nm Outermost Zone Width in Hard X-ray Region. *Japanese Journal of Applied Physics* **44**(4A) (2005), 1994–1998.

[Suz+14] A. Suzuki, S. Furutaku, K. Shimomura, K. Yamauchi, Y. Kohmura, T. Ishikawa, and Y. Takahashi. High-Resolution Multislice X-Ray Ptychography of Extended Thick Objects. *Phys. Rev. Lett.* **112** (5 2014), 053903.

[Ter+15] S. Terentyev, V. Blank, S. Polyakov, S. Zholudev, A. Snigirev, M. Polikarpov, T. Kolodziej, J. Qian, H. Zhou, and Y. Shvyd'ko. Parabolic single-crystal diamond lenses for coherent x-ray imaging. *Applied Physics Letters* **107**(11) (2015), 111108.

[Thi+08] P. Thibault, M. Dierolf, O. Bunk, A. Menzel, and F. Pfeiffer. Probe retrieval in ptychographic coherent diffractive imaging. *Ultramicroscopy* **109**(4) (2008), 338–343.

[TM13] P. Thibault and A. Menzel. Reconstructing state mixtures from diffraction measurements. *Nature* **494**(7435) (2013), 68–71.

[Uhl+11] F. Uhlén, S. Lindqvist, D. Nilsson, J. Reinspach, U. Vogt, H. M. Hertz, A. Holmberg, and R. Barrett. New diamond nanofabrication process for hard x-ray zone plates. *Journal of Vacuum Science & Technology B* **29**(6), 06FG03 (2011).

[Uhl+14] F. Uhlén, J. Rahomäki, D. Nilsson, F. Seiboth, C. Sanz, U. Wagner, C. Rau, C. G. Schroer, and U. Vogt. Ronchi test for characterization of X-ray nanofocusing optics and beamlines. *Journal of Synchrotron Radiation* **21**(5) (2014), 1105–1109.

[UTF86] J. H. Underwood, J. Troy W. Barbee, and C. Frieber. X-ray microscope with multilayer mirrors. *Appl. Opt.* **25**(11) (1986), 1730–1732.

[Var+11] I. A. Vartanyants, A. Singer, A. P. Mancuso, O. M. Yefanov, A. Sakdinawat, Y. Liu, E. Bang, G. J. Williams, G. Cadenazzi, B. Abbey, H. Sinn, D. Attwood, K. A. Nugent, E. Weckert, T. Wang, D. Zhu, B. Wu, C. Graves, A. Scherz, J. J. Turner, W. F. Schlotter, M. Messerschmidt, J. Lüning, Y. Acremann, P. Heimann, D. C. Mancini, V. Joshi, J. Krzywinski, R. Soufli, M. Fernandez-Perea, S. Hau-Riege, A. G. Peele, Y. Feng, O. Krupin, S. Moeller, and W. Wurth. Coherence Properties of Individual Femtosecond Pulses of an X-Ray Free-Electron Laser. *Phys. Rev. Lett.* **107** (14 2011), 144801.

[Vil+11] J. Vila-Comamala, A. Diaz, M. Guizar-Sicairos, A. Mantion, C. M. Kewish, A. Menzel, O. Bunk, and C. David. Characterization of high-resolution diffractive X-ray optics by ptychographic coherent diffractive imaging. *Opt. Express* **19**(22) (2011), 21333–21344.

[Wer12] T. van Werkhoven. Zernike basis function utilities. *Licensed under Creative Commons v3.0* (2012), https://github.com/tvwerkhoven/libtim–py.

[Wil96] K. Wille. *The physics of particle accelerators: an introduction*. Oxford University Press, 1996.

[WM64] E. Wolf and E. Marchand. Comparison of the Kirchhoff and the Rayleigh-Sommerfeld Theories of Diffraction at an Aperture. *J. Opt. Soc. Am* **54**(5) (1964), 587–594.

[Wol52] H. Wolter. Spiegelsysteme streifenden Einfalls als abbildende Optiken für Röntgenstrahlen. *Annalen der Physik* **445**(1-2) (1952), 94–114.

[Yam+15] K. Yamauchi, M. Yabashi, H. Ohashi, T. Koyama, and T. Ishikawa. Nanofocusing of X-ray free-electron lasers by grazing-incidence reflective optics. *Journal of Synchrotron Radiation* **22**(3) (2015), 592–598.

[Yan+11] H. Yan, V. Rose, D. Shu, E. Lima, H. C. Kang, R. Conley, C. Liu, N. Jahedi, A. T. Macrander, G. B. Stephenson, M. Holt, Y. S. Chu, M. Lu, and J. Maser. Two dimensional hard x-ray nanofocusing with crossed multilayer Laue lenses. *Opt. Express* **19**(16) (2011), 15069–15076.

[Yon+14] H. Yoneda, Y. Inubushi, M. Yabashi, T. Katayama, T. Ishikawa, H. Ohashi, H. Yumoto, K. Yamauchi, H. Mimura, and H. Kitamura. Saturable absorption of intense hard X-rays in iron. *Nat Commun* **5** (2014).

[Yum+13] H. Yumoto, H. Mimura, T. Koyama, S. Matsuyama, K. Tono, T. Togashi, Y. Inubushi, T. Sato, T. Tanaka, T. Kimura, H. Yokoyama, J. Kim, Y. Sano, Y. Hachisu, M. Yabashi, H. Ohashi, H. Ohmori, T. Ishikawa, and K. Yamauchi. Focusing of X-ray free-electron laser pulses with reflective optics. *Nat Photon* **7**(1) (2013), 43–47.

[Zha+13] F. Zhang, I. Peterson, J. Vila-Comamala, A. Diaz, F. Berenguer, R. Bean, B. Chen, A. Menzel, I. K. Robinson, and J. M. Rodenburg. Translation position determination in ptychographic coherent diffraction imaging. *Opt. Express* **21**(11) (2013), 13592–13606.

List of Publications

[Sch+15] A. Schropp, R. Hoppe, V. Meier, J. Patommel, F. Seiboth, Y. Ping, D. G. Hicks, M. A. Beckwith, G. W. Collins, A. Higginbotham, J. S. Wark, H. J. Lee, B. Nagler, E. C. Galtier, B. Arnold, U. Zastrau, J. B. Hastings, and C. G. Schroer. Imaging Shock Waves in Diamond with Both High Temporal and Spatial Resolution at an XFEL. *Sci. Rep.* **5** (2015), 11089.

[Sik+15] M. Sikorski, S. Song, A. Schropp, F. Seiboth, Y. Feng, R. Alonso-Mori, M. Chollet, H. T. Lemke, D. Sokaras, T.-C. Weng, W. Zhang, A. Robert, and D. Zhu. Focus characterization at an X-ray free-electron laser by coherent scattering and speckle analysis. *Journal of Synchrotron Radiation* **22**(3) (2015).

[Dzh+14] D. Dzhigaev, U. Lorenz, R. P. Kurta, F. Seiboth, T. Stankevic, S. Mickevicius, A. Singer, A. Shabalin, O. M. Yefanov, M. N. Strikhanov, G. Falkenberg, C. G. Schroer, R. Feidenhans'l, and I. A. Vartanyants. Ptychographical imaging of the phase vortices in the x-ray beam formed by nanofocusing lenses. *Journal of Physics: Conference Series* **499**(1) (2014), 012020.

[Sei+14a] F. Seiboth, M. Scholz, J. Patommel, R. Hoppe, F. Wittwer, J. Reinhardt, J. Seidel, M. Knaut, A. Jahn, K. Richter, J. W. Bartha, G. Falkenberg, and C. G. Schroer. Hard x-ray nanofocusing by refractive lenses of constant thickness. *Applied Physics Letters* **105**(13) (2014), 131110.

[Sei+14b] F. Seiboth, A. Schropp, R. Hoppe, V. Meier, J. Patommel, H. J. Lee, B. Nagler, E. C. Galtier, B. Arnold, U. Zastrau, J. B. Hastings, D. Nilsson, F. Uhlén, U. Vogt, H. M. Hertz, and C. G. Schroer. Focusing XFEL SASE pulses by rotationally parabolic refractive x-ray lenses. *Journal of Physics: Conference Series* **499**(1) (2014), 012004.

[Uhl+14a] F. Uhlén, D. Nilsson, J. Rahomäki, L. Belova, C. Schroer, F. Seiboth, A. Holmberg, H. Hertz, and U. Vogt. Nanofabrication of tungsten zone plates with integrated platinum central stop for hard X-ray applications. *Microelectronic Engineering* **116** (2014), 40–43.

[Uhl+14b] F. Uhlén, J. Rahomäki, D. Nilsson, F. Seiboth, C. Sanz, U. Wagner, C. Rau, C. G. Schroer, and U. Vogt. Ronchi test for characterization of X-ray nanofocusing optics and beamlines. *Journal of Synchrotron Radiation* **21**(5) (2014), 1105–1109.

[Bra+13] S. Braun, A. Kubec, M. Menzel, S. Niese, P. Krüger, F. Seiboth, J. Patommel, and C. Schroer. Multilayer Laue Lenses with Focal Length of 10 mm. *Journal of Physics: Conference Series* **425**(5) (2013), 052019.

[Hop+13] R. Hoppe, V. Meier, J. Patommel, F. Seiboth, H. J. Lee, B. Nagler, E. C. Galtier, B. Arnold, U. Zastrau, J. Hastings, D. Nilsson, F. Uhlén, U. Voigt, H. M. Hertz, C. G. Schroer, and A. Schropp. Full characterization of a focused wave field with sub 100 nm resolution. *Proc. SPIE* **8778** (2013), 87780G.

[Sch+13a] C. G. Schroer, F.-E. Brack, R. Brendler, S. Hönig, R. Hoppe, J. Patommel, S. Ritter, M. Scholz, A. Schropp, F. Seiboth, D. Nilsson, J. Rahomäki, F. Uhlén, U. Vogt, J. Reinhardt, and G. Falkenberg. Hard x-ray nanofocusing with refractive x-ray optics: full beam characterization by ptychographic imaging. *Proc. SPIE* **8848** (2013), 884807.

[Sch+13b] A. Schropp, R. Hoppe, V. Meier, J. Patommel, F. Seiboth, H. J. Lee, B. Nagler, E. C. Galtier, B. Arnold, U. Zastrau, J. B. Hastings, D. Nilsson, F. Uhlén, U. Vogt, H. M. Hertz, and C. G. Schroer. Full spatial characterization of a nanofocused x-ray free-electron laser beam by ptychographic imaging. *Sci. Rep.* **3** (2013), 01633.

[Sch+13c] A. Schropp, R. Hoppe, J. Patommel, F. Seiboth, F. Uhlén, U. Vogt, H. J. Lee, B. Nagler, E. C. Galtier, U. Zastrau, B. Arnold, P. Heimann, J. B. Hastings, and C. G. Schroer. Scanning coherent x-ray microscopy as a tool for XFEL nanobeam characterization. *Proc. SPIE* **8849** (2013), 88490R.

[Uhl+13] F. Uhlén, D. Nilsson, A. Holmberg, H. M. Hertz, C. G. Schroer, F. Seiboth, J. Patommel, V. Meier, R. Hoppe, A. Schropp, H. J. Lee, B. Nagler, E. Galtier, J. Krzywinski, H. Sinn, and U. Vogt. Damage investigation on tungsten and diamond diffractive optics at a hard x-ray free-electron laser. *Opt. Express* **21**(7) (2013), 8051–8061.

[Nil+12] D. Nilsson, F. Uhlén, A. Holmberg, H. M. Hertz, A. Schropp, J. Patommel, R. Hoppe, F. Seiboth, V. Meier, C. G. Schroer, E. Galtier, B. Nagler, H. J. Lee, and U. Vogt. Ronchi test for characterization of nanofocusing optics at a hard x-ray free-electron laser. *Opt. Lett.* **37**(24) (2012), 5046–5048.

[Sch+12a] A. Schropp, R. Hoppe, J. Patommel, D. Samberg, F. Seiboth, S. Stephan, G. Wellenreuther, G. Falkenberg, and C. G. Schroer. Hard x-ray scanning microscopy with coherent radiation: Beyond the resolution of conventional x-ray microscopes. *Applied Physics Letters* **100**(25) (2012), 253112.

[Sch+12b] A. Schropp, J. Patommel, F. Seiboth, B. Arnold, E. C. Galtier, H. J. Lee, B. Nagler, J. B. Hastings, and C. G. Schroer. Developing a platform for high-resolution phase contrast imaging of high pressure shock waves in matter. *Proc. SPIE* **8504** (2012), 85040F.

Danksagung

Während der vergangenen fast vierjährigen Promotionszeit hatte ich das Privileg mit vielen wunderbaren Menschen, nicht nur unmittelbar in der Arbeitsgruppe, sondern auch von externen Instituten und bei einer Vielzahl von Messreisen, zusammenzuarbeiten. An dieser Stelle möchte ich mich ganz herzlich bei all diesen Menschen bedanken, ohne deren Motivation, Geduld und Hilfsbereitschaft diese Arbeit nicht zustande gekommen wäre.

Allen voran gebührt mein Dank meinem Doktorvater Prof. Dr. Christian Schroer, der mir nach der Diplomarbeit auch die Möglichkeit zur Promotion in seiner Arbeitsgruppe gab. Während dieser Zeit war seine enthusiastische und mitreisende Natur stets ein großer Antrieb für mich. Die positive Grundhaltung von Christian und sein unbeschwerter Umgang sorgten für ein überdurchschnittlich gutes Klima innerhalb der Arbeitsgruppe. Nicht zuletzt bewundere ich auch seine exzellente fachliche Kompetenz, mit der er stets Hilfreich zur Seite stand.

Ich möchte mit außerdem bei Herrn Prof. em. Dr. Bruno Lengeler bedanken. Nicht nur für die Übernahme des Zweitgutachtens, sondern auch für die unkomplizierte und schnelle Bereitstellung von Linsen und Komponenten während der gesamten Zeit. Des Weiteren schätze ich so manche Augen öffnende Diskussion.

Die vorliegende Arbeit wurde maßgeblich durch die enge Zusammenarbeit innerhalb der Arbeitsgruppe beeinflusst. Die Diskussionen im Extraktionslabor über Gott und die Welt haben schon so manche Idee hervorgebracht.
Hervorheben möchte ich hier Robert Hoppe für die initiale Idee der RLL und für seine endlosen Stunden an Entwicklungsarbeit an der gemeinsam genutzten Ptychographie-Software, ohne die eine Auswertung der Messdaten undenkbar wäre.
Bei Jens Patommel bedanke ich mich für sein Engagement bei der Erstellung der Wafer-Masken und der Überwindung so mancher Programmierhürde. Mit seiner exakten und gewissenhaften Arbeitsweise sowie der hohen fachlichen Kompetenz hat er mir stets sehr geholfen, so auch bei der Korrektur dieser Arbeit.
Ohne einen kompetenten Ingenieur wäre man des öfteren ziemlich Aufgeschmissen. Zum erfolgreichen Gelingen aller Experimente hat Dirk Samberg einen entscheidenden Beitrag geleistet. Vielen Dank für deine stete Hilfsbereitschaft, cleveren Konstruktionsideen und die vielen Gespräche.
Obwohl Andreas Schropp die meiste Zeit während meiner Dissertation in Stanford verbrachte, so war gerade diese Verbindung essentiell. Ich bedanke mich bei ihm für die vielen tollen Messzeiten an der LCLS und die schöne gemeinsame Zeit auf den Dienstreisen. Seine konstante Hilfe, insbesondere die vielen wertvollen und kritischen Anmerkungen zu dieser Arbeit, sowie seine moralische Unterstützung waren sehr wichtig für mich. Nicht zuletzt ist die Idee einer Phasenplatte aus den Messzeiten an der LCLS entstanden.
Bei Maria Scholz, Felix Wittwer und Juliane Reinhardt bedanke ich mich für die unentbehrliche Unter-

stützung auf Messzeiten und der Mithilfe bei der Datenauswertung.
Die Atmosphäre auf Arbeit ist natürlich besonders durch die Kolleginnen im gemeinsamen Arbeitszimmer geprägt. Hier hatte ich das Glück mit Sandra Stephan und Susanne Klare lange Zeit ein Zimmer teilen zu dürfen. Durch das Beenden der Dissertation und eine Elternzeit wurde es im Büro zeitweise ganz schön einsam. Vielen Dank an euch für die schöne Zeit, euer Einfühlungsvermögen und die interessanten Gespräche.
Was wäre eine Arbeitsgruppe ohne Sekretärin. Für die alltägliche Hilfe bei der Bewältigung des Papierkrieges und der Aufrechterhaltung des Koffeinpegels bedanke ich mich ganz herzlich bei Mirjam Kalusa, Cornelia Junker und Julia Barth.
In annähernd vier Jahren habe ich mit zahlreichen weiteren Menschen am Institut zusammengearbeitet. Einige sind nach erfolgreichem Abschluss weiter gezogen, viele mit Christian nach Hamburg gewechselt und ein harter Kern ist noch vor Ort. Ohne Anspruch auf Vollständigkeit bedanke ich mich außerdem bei Christoph Baumbach, Constantin Bernert, Florian Brack, Roman Brendler, Florian Heinsch, Maik Kahnt, Johannes Richter, Stephan Ritter, Melanie Rödel, Andreas Schwab, Martin Seyrich und Theo Woike für die angenehme Zeit in Dresden.

Obwohl viele Ideen in Dresden gereift sind, ist man für die Umsetzung einer Lösung oft auf externe Hilfe von Spezialisten angewiesen. Für die enge Zusammenarbeit in den vergangenen Jahren und zahlreiche Nachtschichten, um die Lieferung von Linsen in letzter Minute zu ermöglichen, bedanke ich mich bei Andreas Jahn, Martin Knaut und Karola Richter vom IHM in Dresden.
Lange suchten wir nach einer Möglichkeit die Phasenplatten zu produzieren. Christian Rödel lernte ich eher zufällig während einer Messzeit an LCLS kennen. In dieser Begegnung war er sofort von der Idee einer Phasenplatte überzeugt und hatte eine Idee zur Herstellung. Er stellte den Kontakt an die Friedrich-Schiller Universität Jena zur Fertigung der Phasenplatte mit intensiven Kurzpulslasern her. Ich bedanke mich bei ihm für sein Engagement und seinen Kollegen Tobias Ullsperger und Martin Wünsche für die Herstellung der Phasenplatten.
Für die Bereitstellung von Testproben sowie eine langjährige Zusammenarbeit bedanke ich mich bei Ulrich Vogt und seiner Arbeitsgruppe, insbesondere Fredrik Uhlén, Daniels Nilsson, Jussi Rahomäki und Karolis Parfeniukas.
Bei der Herleitung der RLL Form gab es Anfangs viele Hürden. Ich bedanke mich bei Jens Seidel für seine Hilfe zur mathematischen Berechnung.

Viele spannende Messzeiten sind ins Land gegangen und wertvolle Erkenntnisse wurde gewonnen. Für die tatkräftige Unterstützung an den Synchrotronquellen dieser Welt bedanke ich mich bei Ulrich Wagner und Christoph Rau (I13-1, DLS), bei Manfred Burghammer und Britta Weinhausen (ID13, ESRF), bei Bob Nagler, Hae Ja Lee und Eric Galtier (MEC, LCLS) und bei Gerd Wellenreuther, Ulrike Bösenberg und Gerald Falkenberg (P06, PETRA III).

Ohne familiären Rückhalt wäre die Bewältigung des Physikstudiums und insbesondere dieser Promotion nicht möglich gewesen. Ich danke Christin dafür, dass sie stets an meiner Seite ist und mir so die nötige Kraft und den Halt im Leben zur Bewältigung aller Aufgaben gibt. Zu guter Letzt und mir größter Anerkennung danke ich meinen Eltern für ihre bedingungslose Unterstützung und stete Aufmunterung.

Eidesstattliche Versicherung

Hiermit erkläre ich an Eides statt, dass ich die vorliegende Dissertationsschrift selbst verfasst und keine anderen als die angegebenen Quellen und Hilfsmittel benutzt habe.

(Frank Seiboth)
Hamburg, 05. Januar 2016